

Node Density and Quality of Estimation for Infrastructure-based Indoor Geolocation Using Time of Arrival

A Dissertation

Submitted to the Faculty of the

WORCESTER POLYTECHNIC INSTITUTE

in partial fulfillment of the requirements for the

Degree of Doctor of Philosophy

in

Electrical and Computer Engineering

by

Muzaffer Kanaan

April, 2008

APPROVED

Prof. Kaveh Pahlavan, Advisor

Prof. Fred J. Looft, Head, ECE Department

Abstract

Infrastructure-based indoor geolocation systems utilizing a regular grid arrangement of sensors are being investigated for many applications in indoor wireless networks. One of the factors affecting the *Quality of Estimation* (i.e. location estimation accuracy) of these systems is node density. In this dissertation we study the effects of node density on indoor geolocation systems based on time of arrival (TOA).

The effects of node density on the performance of various indoor communication networks (e.g. wireless LANs) in the presence of realistic indoor radio propagation models has been analyzed and reported in the literature. However, we have noted the lack of an equivalent analysis on the effects of node density on the performance of infrastructure-based indoor geolocation systems. The goal of this dissertation is to address this knowledge gap.

Due to the complicated behavior of the indoor radio channel, the relationship between the node density and Quality of Estimation (QoE) is not straightforward. Specifically, QoE depends on factors such as the bandwidth used to make the TOA-based distance measurements, the existence of undetected direct path (UDP) conditions, and coverage. In this dissertation, we characterize these dependencies.

We begin by characterizing the Quality of Estimation for closest-neighbor (CN), least-squares (LS) and weighted LS techniques in the presence of different node densities and a distance measurement error (DME) model based on ray tracing (RT) that was recently proposed in the literature. Then, we propose a new indoor geolocation algorithm, Closest Neighbor with TOA Grid (CN-TOAG), characterize its performance

and show that it outperforms the existing techniques. We also propose an extension to this algorithm, known as Coverage Map Search (CMS) that allows it to be used in suboptimal coverage conditions (which we refer to as *partial coverage conditions*) that may prevent other TOA-based geolocation techniques from being used. We treat the partial coverage case by defining *coverage probabilities* and relating them to the average radius of coverage and dimensions of the indoor area. Next, we characterize the effects of node density on the performance of the CN-TOAG algorithm using a DME model based on UWB measurements, and show that node density and partial coverage are intimately linked together. Since this second DME model also allows for the effects of UDP conditions (which affect the quality of the link or QoL), we also characterize the effects of varying UDP conditions on the performance. Finally, we conclude the dissertation by presenting an analysis of fundamental performance bounds for infrastructure-based indoor geolocation, specifically focusing on the Cramer-Rao Lower Bound (CRLB).

Acknowledgments

I wish to begin by thanking God for helping me get to this point in my life and work. If it were not for His help, mercy and guidance, I would not be writing these words today.

I would like to thank my advisor, Prof. Kaveh Pahlavan for his invaluable help and guidance. He has taught me not only how to do research, but also many other things that I believe made me a better, stronger person in the process.

I would also like to express my thanks and appreciation to my committee members Professor Allen Levesque, Professor Xinrong Li, Professor Xinming Huang and Dr. Ahmad Hatami for their thorough review and thoughtful comments on my dissertation.

I have had the good fortune to work with a stellar group of individuals at the CWINS lab. I would like to thank the following people for their help: Ferit Ozan Akgül, Dr. Bardia Alavi, Nayef Alsindi, Leon Metraud, and Mohammad Heidari.

My supervisors at Verizon Laboratories have been consistently supportive of my efforts at every turn. I would like to acknowledge and thank (in chronological order) Len D'Alotto, William C. Uliasz, Alex Laparidis, Henry Ruiz, Tushar Saxena and Lee Tjio. Many thanks also to my colleagues (former and present): Dr. Vincent O'Byrne, Dr. Pablo Vicharelli, Ms. Donna Fagen, Dr. David A. Freeman. Dr. Rajamani Ganesh, Dr. Art Giordano, and Dr. Richard A. Stanley.

I would also like to thank Dr. Nannaji Saka and Dr. Irwin Schick of Massachusetts Institute of Technology for their valuable help and advice during the various phases of this research.

This dissertation would not have been possible without my dear friends at the Cambridge Musiki Cemiyeti (Cambridge Society for Turkish Music), who were always there for me. I will forever treasure the moments that I have spent with them practicing Turkish music, not to mention the lively and enlightening conversation. I would like to thank the director of the Society, Mr. Feridun Özgören, as well as Dr. Güliz Pamukoglu, Dr. Selis Önel, Dr. Tuba Okutucu, Dr. Metin Sezgin, Dr. Servet Yatin, Berker Evren, and Gamze Güngör Demirci.

Two of my professors from my undergraduate days have encouraged me to choose wireless communications as an area of specialty, and encouraged my graduate work over the years. I would like to acknowledge and thank Prof. Mehmet Şafak of Hacettepe University and Prof. Hasan Amca of Eastern Mediterranean University.

Last but not least, I would like to thank my parents, whose help, support and encouragement over the years was never in short supply. I consider myself truly blessed to have such parents, and it is with deep gratitude that I dedicate this work to them.

Muzaffer Kanaan

Watertown, Massachusetts

April, 2008

Nothing in the world can take the place of Persistence. Talent will not; nothing is more common than unsuccessful men with talent. Genius will not; unrewarded genius is almost a proverb. Education will not; the world is full of educated derelicts. Persistence and determination alone are omnipotent. The slogan 'Press On' has solved and always will solve the problems of the human race. – *Calvin Coolidge*

Victorious warriors win first and then go to war, while defeated warriors go to war first and then seek to win. – *Sun-Tzu*

Table of Contents

Chapter 1	Introduction.....	1
1.1	Motivation for the Dissertation.....	2
1.2	Contributions of the Dissertation.....	6
1.3	Outline of the Dissertation.....	7
Chapter 2	Performance Evaluation Methodology	9
2.1	Indoor Environment.....	9
2.2	Scenario for Performance Evaluation.....	10
2.3	Quality of Estimation (QoE).....	16
2.3.1	Relationship between Quality of Link (QoL) and QoE.....	16
2.3.2	Relationship between node density and QoE	18
2.4	Distance Measurement Error (DME)	19
2.4.1	RT-based DME Model	20
2.4.2	DME Model based on UWB Measurements	21
Chapter 3	Performance of Existing Algorithms	22
3.1	Existing Algorithms for Indoor Applications.....	22
3.1.1	Closest-Neighbor (CN) Algorithm	25
3.1.2	Least-Squares (LS) Algorithm.....	26
3.1.3	Residual Weighting (RWGH) Algorithm.....	29
3.2	Comparative Performance Evaluation.....	31
3.3	Discussion.....	37
Chapter 4	Performance of New Algorithms.....	39
4.1	Closest-Neighbor with TOA Grid (CN-TOAG) Algorithm	39
4.2	Performance Evaluation of CN-TOAG	42
4.2.1	Complexity Analysis for CN-TOAG versus LS and RWGH.....	46
4.3	Coverage Map Search (CMS) Algorithm.....	50
4.4	Performance Evaluation for the CMS Algorithm.....	54
Chapter 5	Partial Coverage Analysis.....	58
5.1	Statistical Behavior of the QoE Under Partial Coverage	58
5.2	Coverage Probabilities.....	60
Appendix 5.A	Coverage Probability Analysis	65
Chapter 6	Effects of Node Density on QoE: Full Coverage	86
6.1	Full Coverage	86
6.2	QoE as a function of Reference Point (RP) Density	87
6.3	Statistical behavior of the QoE under Bipolar Channel Behavior: MSE Profile.....	95
Chapter 7	Analysis of Performance Bounds	103
7.1	Cramer-Rao Lower Bound (CRLB): The Preliminaries.....	103
7.2	CRLB Derivation for the DME Model based on UWB Measurements	106
7.3	Comparison of CN-TOAG Performance with the CRLB	114
7.4	Effects of Node Density on the CRLB: Full Coverage Case	125
7.5	Effects of Node Density on the CRLB: Partial Coverage Case	127

Chapter 8	Conclusions & Future Work.....	131
8.1	Conclusions	131
8.2	Future Work.....	134
Bibliography	136

List of Figures

Figure 1.1 (a) Grid-based deployment of wireless LANs (after [Hil01]) (b) Infrastructure-based indoor geolocation scenario (c) Ad-hoc geolocation scenario	3
Figure 1.2 Summary of the contributions	7
Figure 2.1 Channel profiles for: (a) DDP, (b) UDP [Kan08b]	10
Figure 2.2 (a) Infrastructure-based indoor communication network (after [Hil01]) (b) infrastructure-based indoor geolocation	11
Figure 2.3 Illustrating the concept of coverage in the presence of adverse link conditions	13
Figure 2.4 Full vs. partial coverage in indoor geolocation	15
Figure 2.5 Illustrating the link between QoE and Quality of Link (QoL)	17
Figure 2.6 Node density and its effects on QoE	18
Figure 3.1 Geometric relationships for TOA-based geolocation: (a) ideal non-multipath case, (b) multipath case (region of uncertainty is shaded)	24
Figure 3.2 Basic configuration for an infrastructure-based indoor geolocation system	26
Figure 3.3 LS/RWGH QoE comparison for: (a) LOS channel, (b) OLOS channel	33
Figure 3.4 LS/RWGH comparison: mixed LOS/OLOS channel	33
Figure 3.5 QoE comparison for the CN algorithm over the three channel scenarios	34
Figure 3.6 QoE comparison of the CN, LS and RWGH algorithms for two different node densities: (a) LOS channel, (b) OLOS channel, (c) mixed LOS/OLOS channel	35
Figure 4.1 An indoor geolocation system showing the TOA grid for the CN-TOAG algorithm	40
Figure 4.2 Comparison of CN-TOAG performance vs. LS and RWGH algorithms (system bandwidth = 50 MHz) Dashed lines indicate ranging errors.	43
Figure 4.3 Comparison of CN-TOAG performance vs. LS and RWGH algorithms (system bandwidth = 500 MHz). Dashed lines indicate ranging errors.	43
Figure 4.4 Comparison of CN-TOAG performance vs. LS and RWGH algorithms (system bandwidth = 1000 MHz). Dashed lines indicate ranging errors.	44
Figure 4.5 CN-TOAG performance at the various bandwidth values	45
Figure 4.6 Overall variance of the RT-based DME model (OLOS case)	46
Figure 4.7 General system scenario used to develop the CMS algorithm	50
Figure 4.8 Illustration of partial coverage for the CMS algorithm	51
Figure 4.9 CMS Performance comparison as a function of R for system bandwidth, w , in the range 50-1000 MHz	56
Figure 4.10 CMS performance as a function of R over a larger area for system bandwidth, w , in the range 50-1000 MHz	56
Figure 4.11 CMS performance in the presence of realistic path loss models (20 x 20 m ² vs. 40 x 40 m ² area)	57
Figure 5.1 System scenario for the statistical analysis of the QoE in partial coverage. The numbers in the various areas represent the number of RPs that are likely to be observed throughout that area.	59
Figure 5.2 Coverage probabilities plotted as a function of α	64
Figure 6.1 LS performance as a function of RP density	90
Figure 6.2 CN-TOAG Performance as a function of RP density	91
Figure 6.3 Comparison of LS and CN-TOAG as a function of RP density	92
Figure 6.4 MSE Profile for the LS algorithm. The system bandwidth is a parameter	98

Figure 6.5 MSE Profile for the CN-TOAG algorithm.....	99
Figure 6.6 QoE variation across different QoL classes.....	99
Figure 6.7 Average MSE comparison: LS vs. CN-TOAG	100
Figure 6.8 Variance comparison: LS vs. CN-TOAG	101
Figure 7.1 Example scenario for infrastructure-based indoor geolocation.....	110
Figure 7.2 (a) Discrete PDF of the CRLB at a given point, (b) Average RMSE as a function of bandwidth	113
Figure 7.3 CRLB Calculations over a 20m x 20m area with 4 RPs at a bandwidth of 500 MHz: (a) .	114
Figure 7.4 CRLB results over a 20m x 20m area with 4 RPs at a bandwidth of 1000 MHz: (a)	114
Figure 7.5 Scatter plots of CN-TOAG performance vs. CRLB for the all-DDP case: (a) 500 MHz, (b) 1000 MHz	117
Figure 7.6 Scatter plots of CN-TOAG performance vs. CRLB for the case of UDP-based DME in the measurement set: (a) 500 MHz, (b) 1000 MHz.....	118
Figure 7.7 Comparison of the 90% concentration ellipses on the CRLB vs. the CN-TOAG algorithm: (a) the ellipses. (b) ellipse for the algorithm reoriented with respect to the bound ellipse.....	119
Figure 7.8 Comparison of the CN-TOAG vs. CRLB (all-DDP case) in a 20m x 20m area: (a) $W = 500$ MHz (b) $W = 1000$ MHz	121
Figure 7.9 Comparison of the CN-TOAG vs. CRLB (all-DDP case) in a 20m x 20m area: (a) $W = 2000$ MHz (b) $W = 3000$ MHz	121
Figure 7.10 Relative efficiency of CN-TOAG as a function of bandwidth (all-DDP case).....	122
Figure 7.11 Comparison of CN-TOAG vs. CRLB for the 3-DDP, 1-UDP case in a 20m x 20m area: (a) $w=500$ MHz, (b) $w=1000$ MHz.....	123
Figure 7.12 Comparison of CN-TOAG vs. CRLB for the 3-DDP, 1-UDP case in a 20m x 20m area: (a) $w=2000$ MHz, (b) $w=3000$ MHz.....	124
Figure 7.13 Relative efficiency of CN-TOAG vs. CRLB (3-DDP, 1-UDP case).....	124
Figure 7.14 CRLB as a function of the RP density: full coverage case	127
Figure 7.15 Illustrating the coverage issues for indoor geolocation.....	128
Figure 7.16 CRLB as a function of RP density: partial coverage case.....	130

List of Tables

Table 3-1 Average Degradation in Estimation Accuracy	36
Table 6-1 Coefficients of the third degree polynomial for the LS algorithm	93
Table 6-2 Coefficients of the third degree polynomial for the CN-TOAG algorithm.....	93

Chapter 1 Introduction

Ever since the Global Positioning System (GPS) and cellular networks were launched, there has been an increasing amount of interest in location estimation technologies ([Kap96], [Mis01], [Sha99], [Fis99], [Ott77], [Sil96], [Caf99]). The primary drivers have been either location estimation for emergency services (such as the E-911 initiative from the FCC in the US [FCC96]) or other location-based services, such as yellow-pages, driving directions, location-sensitive advertising and mobility management ([Gio95], [Rao03]). Most of the geolocation platforms have been designed to work in the outdoor environment; but recently there has been increasing interest in geolocation technologies for the indoor case as well ([Pah00], [Wal02], [Wan92], [War97]). In the commercial space, there are applications such as tracking children, and the elderly, as well as helping blind people find their way throughout indoor areas. Other applications may include inventory tracking in large indoor areas such as shopping malls and warehouses. Indoor geolocation will also have an important part to play in applications such as environmental monitoring [Sno03] and pervasive computing [Est02]. In the public safety and military space, very accurate indoor geolocation is needed in order to help policemen, firefighters and soldiers navigate their way and complete their missions inside buildings.

Geolocation schemes using GPS and cellular signals generally do not work well in indoor areas, partly because of the large amount of signal attenuation caused by

building walls and floors [Sei92]. While the signal attenuation issue can be addressed through application of repeaters, this is, in general, a costly proposition. In addition, the behavior of the indoor radio channel has been shown to exhibit very strong multipath characteristics, which have to be analyzed and taken into account, in order for accurate indoor geolocation to be feasible [Pah98]. Moreover, the accuracy requirements of indoor geolocation systems are typically a lot higher compared to the outdoor case. For an application such as E-911, an accuracy of 125 m 67% of the time is considered acceptable [FCC96], while a similar indoor application typically requires an accuracy level on the order of only a few meters [Say05]. Therefore, new techniques have to be developed for precise indoor geolocation.

1.1 Motivation for the Dissertation

The system scenario for infrastructure-based indoor geolocation is analogous to the grid-based deployment of large-scale wireless LANs [Hil01] as shown in Figure 1.1a. For the wireless LAN scenario, we have a number of *access points* (APs) arranged in a regular grid fashion throughout an indoor area. Grid-based deployments are common in practice, since they provide good coverage in indoor areas [Unb02] and also fit well with the layout of most types of buildings where indoor wireless networks are likely to be deployed. For the indoor geolocation scenario, we have a number of *reference points* (RPs) arranged in a grid pattern to locate a user, as shown in Figure 1.1b. RPs are radio transceivers that can measure the *location metrics*, i.e. those characteristics of the received signal useful for the location estimation process. This grid-based deployment is in contrast to the so-called *ad-hoc configuration* where the

nodes can be deployed in any manner; such a configuration is more common for sensor networks and is shown in Figure 1.1c [Aky02]. The indoor geolocation problem for the ad-hoc configuration is outside the scope of this dissertation; however, this has also been investigated in the literature ([Als06a], [Als06b]).

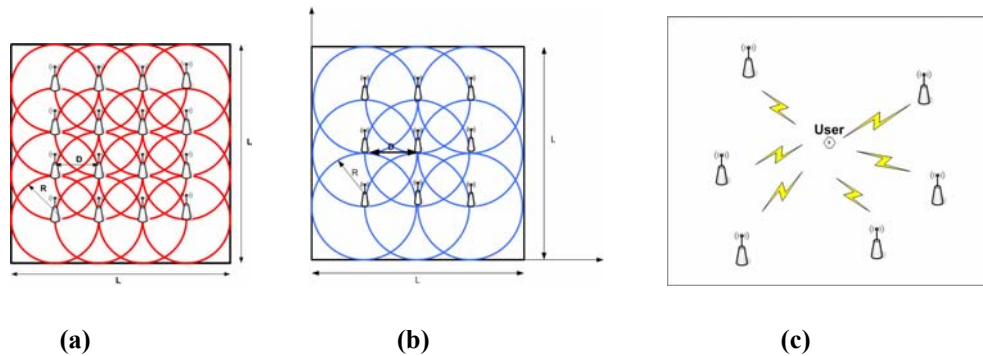


Figure 1.1 (a) Grid-based deployment of wireless LANs (after [Hil01]) (b) Infrastructure-based indoor geolocation scenario (c) Ad-hoc geolocation scenario

With this brief overview on geolocation systems in general and infrastructure-based indoor geolocation in particular, we now pose the following questions. How good is the location estimate that such a system produces? In other words, what is the *Quality of Estimation (QoE)* for such a system? There are several ways of answering these questions, depending on the specific application. For example, in some applications such as high-value inventory tracking, only the accuracy of the location estimate would be considered important. In these cases, the QoE would be defined as the accuracy of the estimate. In contrast, some mission-critical military or public-safety applications involve tracking moving people or objects in a real-time manner for monitoring or surveillance purposes. In such cases, the accuracy of the location estimate, as well as the speed with which a location estimate is obtained would both be considered

important. In this case, the definition of QoE would have to take both of these factors into account. In this dissertation, we are principally concerned with the first definition of QoE, i.e. we focus on the characterization of QoE where the user or object to be located is stationary. Therefore, our definition of QoE is the accuracy of the location estimate. The problem of location tracking is outside the scope of this dissertation; however, the interested reader is referred to [Bro98] and [Hel99] for more details in this area.

The relationship between node density (formally defined as the number of nodes per unit area) and performance (e.g. throughput) for different wireless LAN technologies for telecommunications has been investigated by Unbehaun in his PhD dissertation [Unb02] and also in the article by Unbehaun and Kamenetsky [Unb03]. These studies have been based on radio propagation predictions and revealed that grid-based deployments of access points (APs) in indoor areas can often provide satisfactory coverage in indoor areas for communication applications. However, while there has been some research activity on the relationship between node density and Quality of Estimation for ad-hoc multihop sensor localization ([Pat03], [Shi05], [Pat05], [Sav05]), no such analysis for an infrastructure-based indoor geolocation system using Time of Arrival (TOA) currently exists. This was the first motivating factor for this dissertation.

Due to the complicated behavior of the indoor radio channel, the relationship between node density and QoE is not a simple one to analyze. In fact, until recently, there were no models available in the literature to relate the channel behavior to the errors induced into the TOA measurements, known as *distance measurement error*

(DME) or ranging error. Without such models, it is not possible to explain the causes of large errors in indoor geolocation, which is a function of the actual distance and bandwidth. This issue has recently been addressed in the PhD dissertation by Alavi [Ala06a], who observed via measurements that the indoor channel exhibits *bipolar* behavior, i.e. it statistically changes state to one where a lot of errors are added to the measurements. This bipolar behavior also depends on the quality of the link (QoL) between the RP and the user. Besides this, the way node density affects the QoE does, to a certain extent, depend on the algorithms used. Thus, the second motivating factor for this dissertation was to leverage these recently proposed models to undertake the performance analysis and to explore the relationship between node density and QoE for different types of geolocation algorithms using channel models to reflect this bipolar channel behavior.

Radio coverage within an indoor area can affect the node density and thus QoE. Specifically, for a TOA-based system, there may be coverage deficiencies to the point where the required minimum number of distance measurements for the geolocation process (three, in order to locate the user uniquely in two-dimensional space) cannot be obtained. In this dissertation, we refer to such coverage conditions as *partial coverage* conditions. The existence of partial coverage conditions means that some of the existing TOA-based location estimation techniques cannot be used. Therefore, new techniques need to be explored for TOA-based geolocation in partial coverage environments, and their performance in the presence of realistic channel models needs to be analyzed.

These issues are not adequately addressed in the literature, and provided the third and last motivating factor for this dissertation.

1.2 Contributions of the Dissertation

The main contribution of this dissertation is to provide a systematic analysis of the relationships amongst node density, channel behavior, geolocation algorithms and QoE statistics for infrastructure-based indoor geolocation using Time of Arrival (TOA). In support of this main contribution, we make the following specific contributions to the literature:

1. We explore the behavior of existing geolocation algorithms (LS, RWGH, and CN) in the presence of recently proposed statistical models for distance measurement error proposed in [Ala03] and different node densities. This contribution has been published in [Kan04a].
2. We propose a new indoor geolocation algorithm, known as CN-TOAG, and compare its performance with the LS and RWGH algorithms. The findings of this study have been published in [Kan04b], and [Kan04c]. We propose an extension to the CN-TOAG algorithm, known as CMS, to cover the partial coverage case; this contribution has been published in [Kan07]. We also present a statistical analysis of the partial coverage case.
3. We analyze the QoE for LS and CN-TOAG algorithms in the presence of different node densities. This contribution has been published in [Kan06a].
4. We study the statistical behavior of the QoE in relation to the QoL; this contribution has been published in [Kan06b], and [Kan08a].

5. Finally, we present an analysis of the fundamental QoE bounds for infrastructure-based indoor geolocation in indoor channels with bipolar behavior, using the Cramer Rao-Lower Bound (CRLB) [Kan08b].

Figure 1.2 summarizes the contributions of this dissertation.

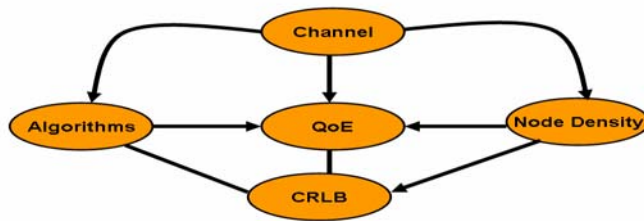


Figure 1.2 Summary of the contributions

1.3 Outline of the Dissertation

The rest of this dissertation is organized as follows. In chapter 2, we provide an overview of the performance evaluation methodology and summarize the DME models that have been used for this research. In chapter 3, we present the results of a comparative performance evaluation of existing geolocation algorithms in the presence of the recently proposed DME models and different node densities. In chapter 4, we present the CN-TOAG and CMS algorithms, and assess their performance. Chapter 5 presents a statistical analysis of the partial coverage situation. An analysis of the performance of CN-TOAG and LS algorithms in the presence of different node densities and statistical behavior of the QoE with respect to QoL is discussed in chapter 6. An analysis of the fundamental QoE bounds is presented in Chapter 7. Chapter 8

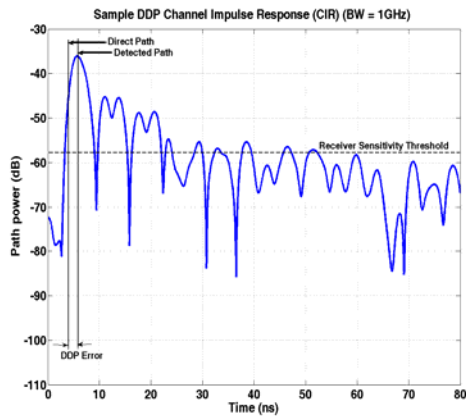
provides a summary of the main results of the dissertation and suggests avenues for future research.

Chapter 2 Performance Evaluation Methodology

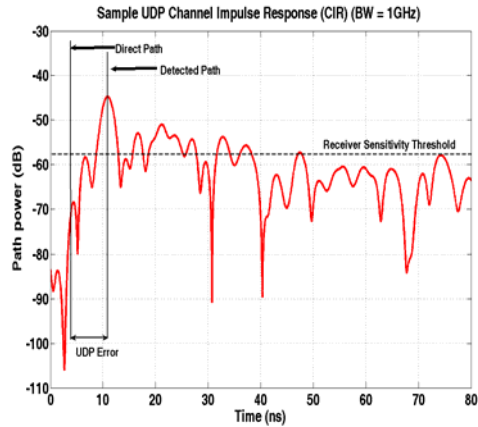
The indoor environment has certain particular characteristics that affect the Quality of Estimation for TOA-based indoor geolocation. We begin by reviewing these characteristics at a high level. We then describe the scenario for performance evaluation in detail. We end this chapter by a brief review of the existing literature on models to describe the statistics of the errors introduced by the channel into TOA-based distance measurements.

2.1 Indoor Environment

As mentioned in chapter 1, the indoor radio channel exhibits very strong multipath characteristics. It also exhibits *bipolar* behavior, in the sense that the channel can sometimes can change state and introduce substantial errors into TOA-based distance measurements [Ala06a]. In this case, the channel is considered to have two states, depending on whether the TOA of the direct path (DP) between transmitter and receiver is strong enough to be detected or not. In the first case, the DP is strong enough in power to be detected; we refer to this as the Detected Direct Path (DDP) case. In this case, the primary source of the errors is multipath. In the second case, the DP cannot be detected at all; we refer to this as Undetected Direct Path (UDP) case. Figure 2.1 below shows example channel profiles for the DDP and UDP cases.



(a)



(b)

Figure 2.1 Channel profiles for: (a) DDP, (b) UDP [Kan08b]

2.2 Scenario for Performance Evaluation

The system scenario for infrastructure-based indoor geolocation resembles the deployment of most indoor wireless networks, such as WLANs, with radio transceivers, generally known as *access points* (APs) distributed in a grid fashion throughout an indoor area. This can be seen in Figure 2.2a. The analog of an AP in the indoor geolocation case is a *reference point* (RP), as shown in Figure 2.2b.

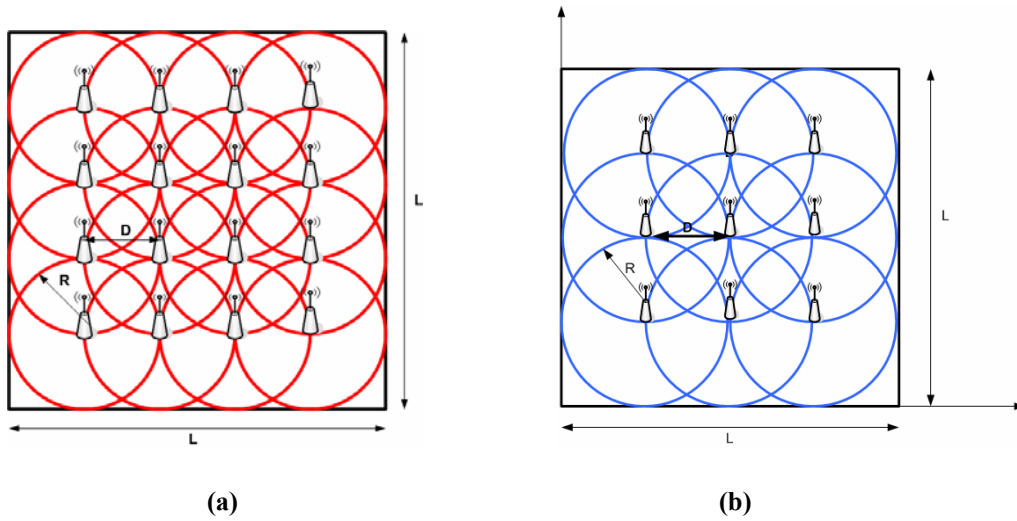


Figure 2.2 (a) Infrastructure-based indoor communication network (after [Hil01]) (b) infrastructure-based indoor geolocation

In this dissertation, we investigate how the performance of an infrastructure-based indoor geolocation system using TOA varies as a function of node density. In order to help put this issue in perspective, we refer to Figure 2.2. For the sake of simplicity, we assume that the RPs all have an average coverage radius of R meters, and are spaced D meters apart. The idea here is to understand how *node density*, i.e. the number of RPs per unit area that can be contacted by a user, impacts the QoE achievable from this system. Quantifying the effect of node density on the QoE for a TOA-based indoor geolocation system carries special significance, since most TOA-based location estimation algorithms either will not work properly or will not work at all if there are fewer than three distance measurements available.

From an indoor geolocation perspective, node density can be defined as the number of RPs that can be contacted by a user per unit area. This definition has a close relationship with radio coverage. But what exactly does coverage mean and how does it relate to performance analysis for indoor geolocation? In order to answer these

questions, it is helpful to first explore some of the existing body of literature on indoor propagation research and review the existing definitions of radio coverage.

For the indoor environment, two methods of defining coverage are widely used. The first definition mainly concentrates on the distance-power relationship in an indoor area ([Pah98], [How90], [How92], [She96], [Mat98], [Lie98]). Specifically, for a fixed transmitter power, the received power, P_r , is generally assumed to vary with distance, d , according to the relationship [How90]

$$P_r(d) = Ad^{-K} \quad (2.1)$$

where A is a constant set by the transmitted power and the measurement system gain, and K is the propagation path-loss exponent. For free space $K = 2$, and for some office buildings, it can be between 2 or 3, and even higher in some cases. Based on this definition, the area of coverage for a wireless transmitter is determined purely on the basis of signal strength, i.e. when the path-loss value reaches a certain maximum value, PL_{\max} , the signal is attenuated so much that it is below the receiver sensitivity threshold and can no longer be detected. The value of d that corresponds to PL_{\max} then determines the (ideally) circular region of coverage.

The second definition of radio coverage takes a wider view. Specifically, in this case, radio coverage area for a wireless transmitter is that area over which communication is feasible according to some criterion such as a minimum carrier-to-noise ratio or receiver sensitivity, as outlined by Panjwani et al. [Pan96]. Dardari and Tralli defined coverage in a similar way, in terms of outage probabilities [Dar99]. This definition is a step beyond the first one, in that it considers not just the raw signal

strength, but also other parameters that determine the quality of the radio link (or QoL) in the definition of radio coverage. We illustrate this concept with a simple example. Consider the simplified situation depicted in Figure 2.3 below where we have a number of IEEE 802.11 WLAN APs (shown as black dots in the figure) covering a section of an office building. In this example, the APs are assumed to be very close to one another, and so will cause a substantial amount of interference both to one another as well as to users trying to access the network. A very high amount of interference is experienced, particularly by users who are in the area marked with 'X' in Figure 2.3. Now suppose that we have an application that requires a minimum of 2 Mbps throughput from this system. Due to the automatic rate selection algorithms implemented on most APs (which will adjust the transmission rate as a result of interference [Har04]), the users in area 'X' may never be able to experience this level of throughput, and as a result, the coverage area for that specific application may be reduced. This example highlights the fact that QoL as well as the raw signal strength will have a role to play in determining coverage.

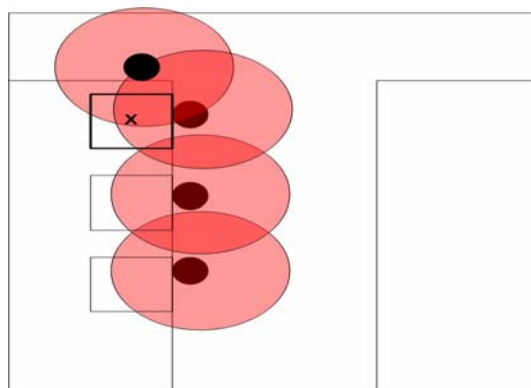


Figure 2.3 Illustrating the concept of coverage in the presence of adverse link conditions

For our discussion of node density and its effects on QoE, both definitions of coverage are applicable to a certain extent. Since we are concerned with TOA-based indoor geolocation, we know that we will need a minimum of three distance measurements to be able to estimate location of the user uniquely in 2-D space (for our analysis in this dissertation, we assume that the synchronization mismatch between the RPs and the user is negligible). For this aspect of the problem, we are concerned with the number of RPs that the user can see at any specific point in an indoor area, so we need to keep the first definition in mind. However, we also have to keep in mind the effects of multipath and UDP conditions, so we need to consider the QoL as well, when we consider the effects of node density. This implies we also need to keep in mind the second definition of coverage.

In order to set the stage for an analytical discussion of coverage and its effects on performance, we first define the *coverage factor*, α :

$$\alpha = \frac{R}{D} \quad (2.2)$$

where R is the average radius of coverage, and D is the separation distance between the RPs in meters. We will also use the *node density*, ρ (which we shall also refer to as *RP density* in the future chapters), to describe performance, which is defined as:

$$\rho = \frac{N}{A} \quad (2.3)$$

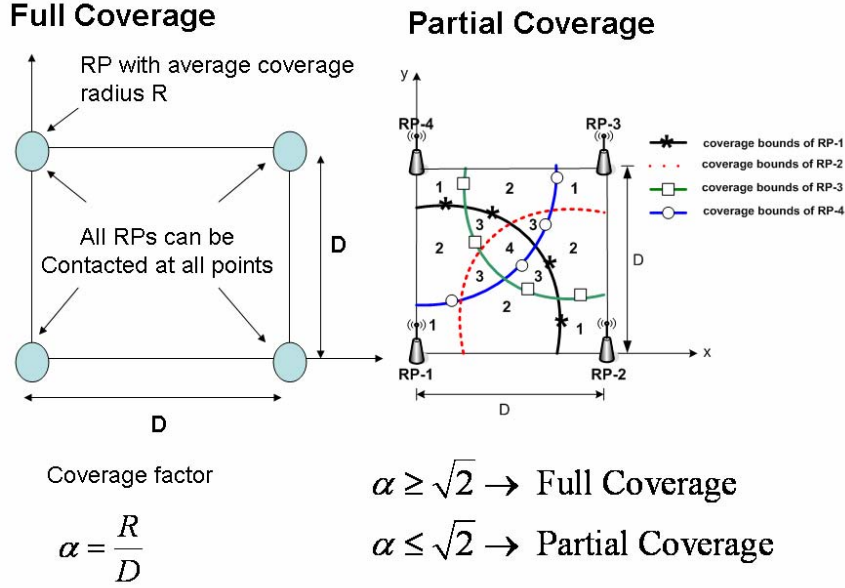


Figure 2.4 Full vs. partial coverage in indoor geolocation

It is worth noting that the concepts of the coverage factor and node density are interrelated. For the scenario of Figure 2.4, since the size of the area, $A = D^2$, we can write (2.3) using (2.2) as:

$$\rho = \frac{N\alpha^2}{R^2} \quad (2.4)$$

Therefore, any results obtained for the QoE (e.g. the Mean-Square-Error, or MSE for the location estimate) obtained in terms of ρ can be written in terms of α using (2.4).

From the definition of α , it is clear that all four RPs can be observed at all points (i.e. a range measurement can be obtained from all four RPs) if $\alpha \geq \sqrt{2}$. We term this scenario *full coverage*. If, on the other hand, $\alpha < \sqrt{2}$, then not all RPs can be observed at all points, and we term this scenario *partial coverage*. We will refer to the

definitions of full and partial coverage often when we discuss the relationship between node density and performance in chapters 5-7. Figure 2.4 shows the difference between full coverage and partial coverage scenarios.

2.3 Quality of Estimation (QoE)

We have broadly described QoE in chapter 1 as a performance metric which indicates how good an estimate the geolocation system produces. As mentioned in chapter 1, our definition of QoE is the accuracy of the estimate, i.e. it is related to the location estimation error. By this definition a low location estimation error will give rise to a high QoE. QoE is influenced by node density, but when we formulate this relationship, we have to consider channel behavior as well. This becomes even more important as we consider the unavoidable occurrence of UDP conditions in indoor environments. In the context of TOA-based indoor geolocation, channel behavior determines the Quality of Link (QoL) between an RP and the user which, in turn, determines the QoE. For the purposes of this dissertation, we classify QoL on the basis of whether the DP is detectable or not. In the next section, we will discuss the relationship between QoL and QoE. This is followed by a discussion of the relationship between node density and QoE.

2.3.1 Relationship between Quality of Link (QoL) and QoE

In Figure 2.5, we show an infrastructure-based indoor geolocation system composed of four RPs in four corners of a square room with dimensions D_1 m by D_1 m. All four RPs make TOA-based distance measurements to the user via the four radio

links to the user. Suppose that the DP is detectable on all four radio links as illustrated in Figure 2.5a. In this case, the QoL on all four links is said to be DDP. In this case, the DME is entirely due to multipath. Provided that the bandwidth is high enough, the TOA of the DP can be measured quite precisely, which leads to low DME [Ala06a] and therefore low location estimation error. As a result, we have high QoE.

Now, consider the case illustrated in Figure 2.5b, where a large metallic object is moved in the path between RP-3 and the user. In this case, the DP is blocked on that radio link; therefore, the QoL on that link now becomes UDP, and we will have large DME on the measurement performed by that RP. The QoL on the other three links remains as DDP. Because we now have one distance measurement with a lot of error, the user's location is estimated with lower accuracy; this gives rise to low QoE. However, even if one or more distance measurements contains a lot of error, it is still possible to obtain accurate location estimates if the location estimation algorithm has adequate intelligence, as we will see in chapter 3. We will discuss the statistical variation of the QoE as a function of QoL in greater detail in chapter 6.

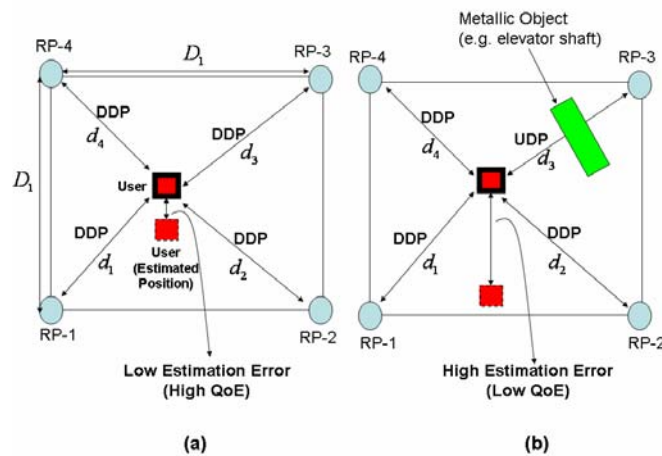


Figure 2.5 Illustrating the link between QoE and Quality of Link (QoL)

2.3.2 Relationship between node density and QoE

Now, we are ready to discuss how node density can affect the QoE for TOA-based indoor geolocation systems. Referring to Figure 2.6, we see that as we increase the size of the area, the node density (as defined by the parameter ρ in (2.3)) will decrease. Suppose that the DP is detectable on all four links, i.e. any errors in the distance measurements are due to multipath effects only. As we will discuss in section 2.4, the overall distance measurement error (DME) will now increase, since the multipath-based DME has been shown to increase with the actual distance [Ala06a]. As a result, location estimation error is high, and the QoE is low as shown in Figure 2.6b. Furthermore, we note from [Ala06a] that the probability of occurrence of UDP conditions increases with actual distance. In reference to the system scenario of Figure 2.6b, this means that, depending on the actual distance, some of the links could change state and become UDP instead of DDP. This is why it is so critical that channel behavior be considered when quantifying the effects of node density on the performance of infrastructure-based indoor geolocation systems using TOA.

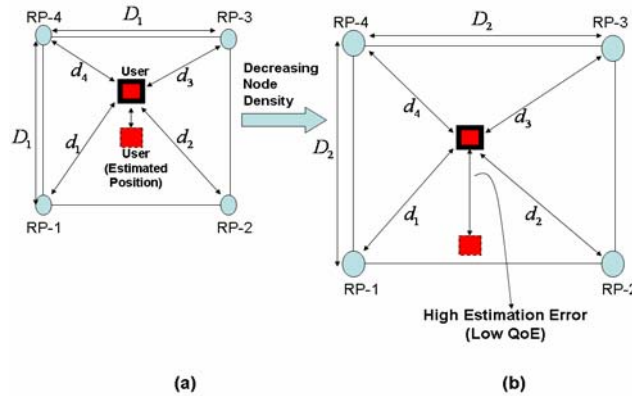


Figure 2.6 Node density and its effects on QoE

2.4 Distance Measurement Error (DME)

The presence of heavy multipath conditions in the indoor environment means that the TOA of the DP cannot be accurately measured. As a result, the measured distance between the transmitter and receiver is different from the actual distance, thereby resulting in *distance measurement error* (DME). The DME is generally given as:

$$\varepsilon = \hat{d} - d \quad (2.5)$$

where \hat{d} is the estimated distance and d is the true distance. The sources of DME are basically two-fold: systematic (such as those related to synchronization mismatch between a transmitter and receiver), and channel-related (such as those due to Obstructed LOS channel conditions). In this dissertation, we assume that the systematic errors are negligible and that the dominant source of errors is the channel. Because of the statistical variation of the indoor channel, ε is a random variable. As a side note, the terms “distance measurement” and “distance measurement error” are also referred to as “ranging” and “ranging error” respectively in the literature and we will use these two terms interchangeably for the rest of this dissertation.

In this dissertation, we use the statistical DME models outlined in the next two subsections for the performance evaluation. The main motivation for this is that the indoor propagation models designed for telecommunication applications, such as the Saleh-Valenzuela (S-V) model ([Sal87]) and its extensions ([Mol03], [Spe00], [Mol06]) focus on modeling the root-mean-square (RMS) delay spread as well as the distance-

power relationship for communication applications. As such, they are not suitable for performance analysis of TOA-based indoor geolocation systems, where the important channel parameter is the TOA of the DP. It has already been shown in the literature ([Ala06a], [Pah05]) that these models cannot explain the causes of large DME values in the indoor environment, mainly because they do not account for the existence of UDP conditions.

2.4.1 RT-based DME Model

The first of these models is based on ray tracing (RT) simulations [Ala03]. This model partitions channel behavior into line of sight (LOS) and obstructed line of sight (OLOS). The overall model is

$$\hat{d}_i = d_{a,i}(1 + \gamma) \quad (2.6)$$

where \hat{d}_i is the observed distance measurement between the sensor and the i -th RP, $d_{a,i}$ is the actual distance and γ is a random variable that defines the statistical distribution of the DME. It has been shown that ([Ala03]) for the LOS case, the distribution of γ is Gaussian with zero mean and a variance that depends on the bandwidth used, i.e. $\gamma = \gamma_{Lw}$ (where the subscript w denotes dependence on the bandwidth w) and the PDF of γ_{Lw} is

$$f(\gamma_{Lw}) = \frac{1}{\sqrt{2\pi}\sigma_{Lw}} e^{-\frac{\gamma_{Lw}^2}{\sigma_{Lw}^2}} \quad (2.7)$$

For the OLOS case, the distribution of γ is a linear combination of Gaussian and exponential distributions ([Ala03]), i.e. $\gamma = \gamma_{Ow}$ where the PDF of γ_{Ow} is

$$f(\gamma_{Ow}) = W_G \frac{1}{\sqrt{2\pi}\sigma_{Ow}} e^{-\frac{\gamma_{Ow}^2}{\sigma_{Ow}^2}} + W_{Exp} \lambda_w e^{-\lambda_w \gamma_{Ow}} u(\gamma_{Ow}) \quad (2.8)$$

2.4.2 DME Model based on UWB Measurements

The second model has been obtained through empirical measurements in the UWB regime [Ala05]. Specifically, it has been shown that both multipath-based DME and UDP-based DME follow a Gaussian distribution, with mean and variance that depends on the bandwidth. The overall model can be expressed as follows:

$$\hat{d} = d + G(m_w, \sigma_w) \log(1 + d) + \zeta \cdot G(m_{UDP,w}, \sigma_{UDP,w}) \quad (2.9)$$

where $G(m_w, \sigma_w)$ and $G(m_{UDP,w}, \sigma_{UDP,w})$ are the Gaussian RVs that refer to multipath and UDP-based DME, respectively. The subscript w in both cases denotes the bandwidth dependence. An important point to be noted from (2.9) is the logarithmic dependence of the DDP-based DME on the actual distance. The parameter ζ is a binary RV that denotes the presence or absence of UDP conditions, with a probability density function (PDF) given as:

$$f(\zeta) = P_{UDP,w} \delta(\zeta - 1) + (1 - P_{UDP,w}) \delta(\zeta) \quad (2.10)$$

where $P_{UDP,w}$ denotes the probability of occurrence of UDP-based DME.

Chapter 3 Performance of Existing Algorithms

In this chapter, we present a comparative study of existing algorithms under the RT-based DME model discussed in the last chapter. Specifically, we concentrate on the Closest-Neighbor (CN), Least-Squares (LS) and Weighted LS (WLS) methods. After describing the algorithms used, we present the results of our evaluations. The material in this chapter was first reported in [Kan04a].

3.1 Existing Algorithms for Indoor Applications

As mentioned in chapter 1, geolocation problem in general has been well-studied and there is a large amount of literature on this subject. Most of the recent literature focused on the geolocation problem in terrestrial cellular networks, mainly inspired by cellular service providers' need to comply with regulatory initiatives such as E-911 in the US, and E-112 in Europe. In addition, the propagation environment that was used for these studies was mainly outdoor settings, such as urban, suburban, rural etc. The issue of designing algorithms specifically for the indoor geolocation application has only recently begun to receive attention ([Jen01], [Pro03]).

Existing geolocation algorithms can be grouped under two main headings: *geometric* algorithms ([Caf98], [Tho01], [Aso01], [Jeo00], [Vil99], [Gou91], [Cha94], [Wan03], [McG03], [Con02], [Den04]) and *pattern-recognition* algorithms ([Roo02], [Che00], [Bah00], [Jan03], [Ner04], [Ner06], [Bat02]). Geometric algorithms use the measured location metrics to formulate a geometric relationship between the location of the reference points (RPs) and the user location. This relationship generally results in a

series of nonlinear equations, which can be solved using a variety of analytical and numerical techniques. An example of a geometric technique that is especially relevant to our discussion in this dissertation is one based on TOA, which is illustrated on Figure 3.1. In TOA-based geolocation systems, the one-way propagation delay between a transmitter and receiver is used to come up with an estimate of the distance between them. Geometrically, this implies that a TOA measurement at every RP determines a circle (in 2-D space) centered at that RP on which the user must lie. Assuming no error in the distance measurements, the intersection point of the circles would give the location of the user (see Figure 3.1a). Note that a minimum of three distance measurements are needed in order to locate the user uniquely in 2-D space. Of course, in a real system, the TOA measurements have some error, so the three circles will not intersect at the same point; this gives rise to a region of uncertainty for the user location (see Figure 3.1b). Another important note with respect to the geometric techniques is that the performance tends to be sensitive to the geometric relationship between the user and the RPs. For instance, if the RPs and the user are all lined up in a straight line then it is possible that the positioning mean-square error (MSE) will be very large; for these cases, it may be important to have adequate intelligence in the location estimation algorithm [Qi05].

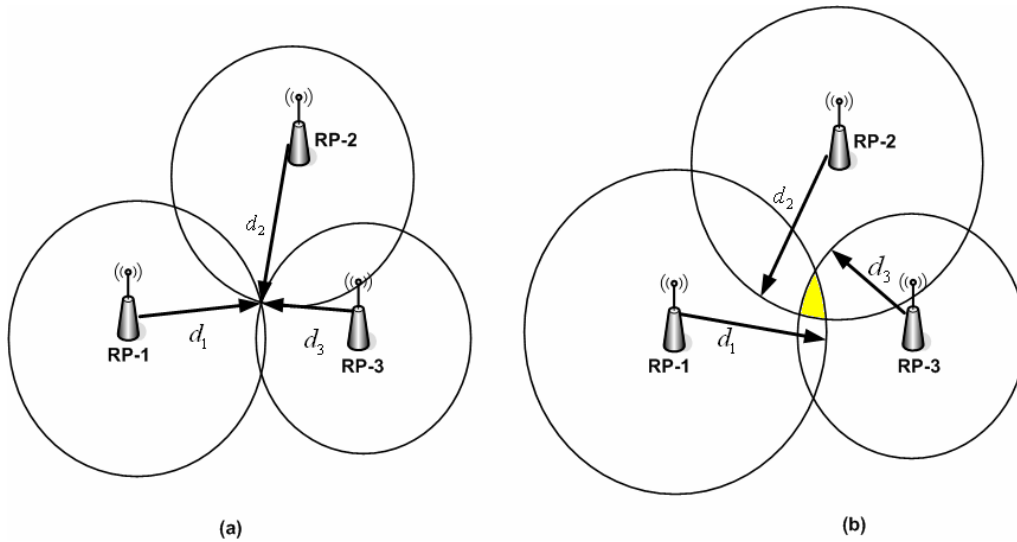


Figure 3.1 Geometric relationships for TOA-based geolocation: (a) ideal non-multipath case, (b) multipath case (region of uncertainty is shaded)

In pattern recognition techniques, the area over which a user is to be located would first need to be characterized so that a unique value of the location metric is associated with every possible location. As mentioned in chapter 2, this could, for example, be done with RSS as a location metric. The characterization could be done through exhaustive measurements in the area of interest ([Bah00], [Jan03]); however, this is generally a costly proposition, especially in the indoor setting, where the site-specific nature of the indoor radio channel and changing layout of an indoor area (for example, addition of new furniture) could quickly render a characterization database meaningless. The alternative is to do the characterization through the use of channel modeling techniques as discussed in the PhD dissertation by Hatami [Hat06].

Historically, performance characterization of geolocation systems in the indoor environment has been complicated by the fact that there were no models available for distance measurement errors (DMEs). This issue has recently been addressed as discussed in the last chapter [Ala06a]. Therefore, the first focus of this research was to

characterize the Quality of Estimation (QoE) various existing geolocation algorithms under these models.

After careful consideration, three algorithms were selected as representative samples for this study, namely Closest-Neighbor (CN), Least-Squares (LS) [Dav68] and Residual Weighting (RWGH), which is a form of weighted LS (WLS) algorithm [Che99]. CN was selected because of its use in early-generation indoor geolocation systems (such as the system from *PinPoint* [Wer98]). LS was selected due to its use in popular geolocation systems such as GPS, and RWGH was selected because of its ability to combat OLOS conditions common in cellular systems.

3.1.1 Closest-Neighbor (CN) Algorithm

Consider a group of reference points (RPs), arranged in a regular grid to locate a user, such as the one shown in Figure 3.2. In such a scenario, each RP is located at D meters away from its adjacent RPs. In order to locate the user, each RP would perform a distance measurement to that user. Let d_i be the distance measurement performed by RP i , which is located at $\mathbf{R}_i = [x_i, y_i]^T$. The CN algorithm estimates the location of the user, \mathbf{R}_{est} , as the location of the RP that is located closest to that user. In other words, \mathbf{R}_{est} is that value of \mathbf{R}_i for which the corresponding distance measurement, d_i , is the minimum in the set. For example, in Figure 3.2, the location of the user would be determined as the location of RP-4.

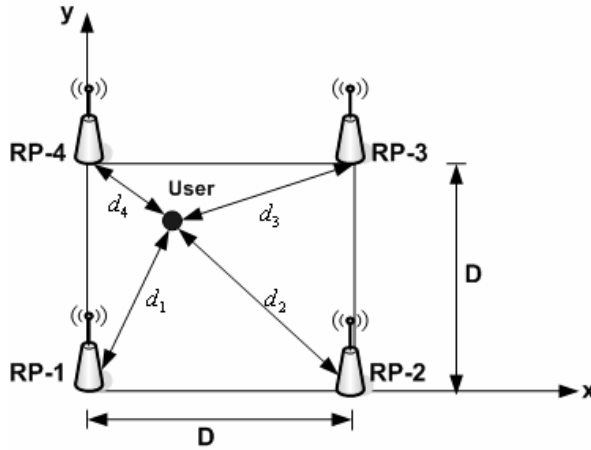


Figure 3.2 Basic configuration for an infrastructure-based indoor geolocation system

3.1.2 Least-Squares (LS) Algorithm

The LS algorithm is fundamentally focused on minimizing the value of the objective function, $f(\mathbf{x})$, usually formulated as:

$$f(\mathbf{x}) = \sum_{i=1}^N \left(\sqrt{(x-x_i)^2 + (y-y_i)^2} - d_i \right)^2 \quad (3.1)$$

where $\mathbf{x} = (x, y)^T$ is the user location to be determined, and N is the number of reference points. The square-root term is readily recognized as the distance between a point (x, y) in the Cartesian coordinate system, and a reference point located at (x_i, y_i) . The difference in the parentheses is commonly called the *residual* of the estimate. Of course, at the true location of the user, each of terms within the summation would be identically zero, such that $f(\mathbf{x}) = 0$. However, in practice, the set of distance measurements, d_i ($1 \leq i \leq N$), contains some errors due to OLOS channel behavior and systematic errors (see section 2.4), such that the summation in equation (3.1) will never be identically zero. For

the purposes of this discussion, we assume that the systematic errors in the distance measurements are negligible, and that the dominant source of errors is the channel. OLOS channel conditions generally result in the strongest signal being received with longer delay, with the resulting in a higher value for the distance measurement. Under such circumstances, a solution (x, y) can be found, which minimizes the value of $f(\mathbf{x})$ in a least-squares sense. For this paper, we used a least-squares algorithm developed by Davidon [Dav68] to minimize $f(\mathbf{x})$, which we discuss below.

The Davidon algorithm is a computationally efficient least-squares algorithm that is based on the Newton-Raphson method, and belongs in the general category of quasi-Newton methods ([Fle87], [Opp04]). The Davidon algorithm searches for the point minimizing (3.1) (generally denoted as the vector, \mathbf{x}) in an iterative manner, as defined by the equation:

$$\mathbf{x}_{k+1} = \mathbf{x}_k - \mathbf{H}_k \mathbf{g}(\mathbf{x}_k) \quad (3.2)$$

where \mathbf{H}_k represents an approximation to the inverse of the Hessian of $f(\mathbf{x})$, $\mathbf{G}(\mathbf{x})$, whose elements are defined as:

$$G_{jk}(x_1, x_2, \dots, x_N) \equiv \frac{\partial^2 f(x_1, x_2, \dots, x_N)}{\partial x_j \partial x_k} \quad (3.3)$$

and $\mathbf{g}(\mathbf{x})$ is the gradient of $f(\mathbf{x})$, defined as:

$$\mathbf{g}(\mathbf{x}) = \nabla f(\mathbf{x}) \quad (3.4)$$

As can be seen from (3.4), $\mathbf{G}(\mathbf{x})$ is a matrix of second derivatives. It can be shown that $\mathbf{G}(\mathbf{x})$ is both symmetric, and positive-definite. However, computing the Hessian and

its inverse at every iteration point (as the Newton-Raphson method generally requires) can be computationally prohibitive. Therefore, the Davidon algorithm tries to construct an approximation to it. Of course, in doing this, one would have to ensure that the approximation, \mathbf{H}_k , stays both symmetric and positive-definite between successive iterations. To accomplish this, \mathbf{H}_k is updated according to the equation:

$$\mathbf{H}_{k+1} = \mathbf{H}_k + \frac{\lambda_k - 1}{\rho_k} \mathbf{r}_k \mathbf{r}_k^T \quad (3.5)$$

where:

$$\mathbf{r}_k = \mathbf{H}_k \mathbf{g}(\mathbf{x}_{k+1}) \quad (3.6)$$

and

$$\rho_k = (\mathbf{g}(\mathbf{x}_{k+1}))^T \mathbf{H}_k (\mathbf{g}(\mathbf{x}_{k+1})) = \mathbf{r}_k^T \mathbf{g}(\mathbf{x}_{k+1}) \quad (3.7)$$

where λ_k is a parameter specially chosen to ensure that \mathbf{H}_{k+1} stays positive definite given that \mathbf{H}_k is. This point will be discussed in greater detail a little later in this section. Equation (3.7) is readily recognized as a quadratic form. Therefore, as long as \mathbf{H}_k is positive-definite, ρ_k will be greater than zero, and will be zero only if $\mathbf{g}(\mathbf{x})$ is zero. As such, (3.7) is often used as an explicit stopping criterion for the algorithm. Of course, in practice, ρ_k will never be identically zero, but can be compared with some small tolerance value, ϵ , so that computations stop when $\rho_k \leq \epsilon$.

All this leaves us with the task of setting λ_k , which is somewhat more complex. As can be inferred from (3.5), this quantity is of central importance in ensuring that the

\mathbf{H}_k matrices remain positive-definite throughout successive iterations. It can be shown that [Dav68]:

$$\lambda_k = \frac{\gamma_k}{\gamma_k + 1} \quad (3.8)$$

where:

$$\gamma_k \equiv -\frac{\mathbf{r}_k^T \mathbf{g}(\mathbf{x}_k)}{\rho_k} \quad (3.9)$$

Choosing λ_k in accordance with (3.8) and (3.9) generally ensures that \mathbf{H}_k remains positive-definite from one iteration to the next, unless $\gamma_k = -1$. Because of this possibility, the Davidon algorithm provides a slightly different way of mapping γ_k values to λ_k values. Specifically, two numbers, α and β , are defined. The values of these can be picked at will. Then, the Davidon algorithm defines the following transformation from γ_k values to λ_k values:

$$\Lambda(\gamma) = \begin{cases} \alpha & -\frac{\beta}{\beta+1} < \gamma < \frac{\alpha}{1-\alpha} \\ \beta & -\frac{\beta}{\beta-1} < \gamma < \frac{\beta}{\beta+1} \\ \frac{\gamma}{\gamma+1} & \text{elsewhere} \end{cases} \quad (3.10)$$

3.1.3 Residual Weighting (RWGH) Algorithm

The RWGH algorithm has been investigated in the PhD dissertation by Chen [Che99] as a way of mitigating the effects of errors in distance measurements brought

about by OLOS channel conditions. Although originally formulated in the context of geolocation in terrestrial cellular systems, this algorithm was included in this study to evaluate its performance in an indoor setting, and can be basically viewed as a form of weighted least-squares algorithm.

The fundamental concept behind this algorithm is as follows: since OLOS channel conditions introduce errors that are strictly positive, distance measurements corrupted by OLOS errors would give rise to location estimates with higher residuals than would be the case with no OLOS errors. Therefore, if the number of distance measurements is greater than the minimum required (which, for a TOA-based system, is three), then the distance measurements can be grouped in various ways and intermediate LS estimates derived from those sub-groups. Some of these intermediate estimates would have lower residuals than others. The final estimate of the location can then be formed as a linear combination of these intermediate estimates, with each intermediate estimate weighted by the inverse of its associated residual. This means that, in the computation of the final estimate, those intermediate estimates with lower residuals would be assigned more weight. In this manner, the overall accuracy of the location estimate can be improved. It is worth noting, however, that with this technique, all the measurements have an influence on the solution, including those that have more error than others due to OLOS conditions. This could actually degrade the location estimation performance. For these cases, other solutions, such as the LMedS algorithm have been recently proposed [Cas06].

Specifically, given M ($M > 3$) distance measurements, the algorithm calls for the formation of N different distance measurement combinations, where

$$N = \sum_{i=3}^M \binom{M}{i} \quad (3.11)$$

with each combination being represented by an index set $\{S_k \mid k = 1, 2, \dots, N\}$. An intermediate LS estimate is then computed for each set of measurements. Note that the sets S_k will not necessarily all be of the same size. Therefore, the residuals in the intermediate LS estimates may depend on the size of the set. In order to remove this dependence, a *normalized* residual is computed for every intermediate estimate, \mathbf{x}'_k , as:

$$\tilde{R}_{es}(\mathbf{x}'_k, S_k) = \frac{R_{es}(\mathbf{x}'_k, S_k)}{\text{size of } S_k} \quad (3.12)$$

The final estimate, \mathbf{x}' , can then be computed as:

$$\mathbf{x}' = \frac{\sum_{k=1}^N \mathbf{x}'_k \left(\tilde{R}_{es}(\mathbf{x}'_k, S_k) \right)^{-1}}{\sum_{k=1}^N \left(\tilde{R}_{es}(\mathbf{x}'_k, S_k) \right)^{-1}} \quad (3.13)$$

3.2 Comparative Performance Evaluation

The performance of the three algorithms described in sections 3.1.1-3.1.3 is evaluated through simulations. The regular grid arrangement of four reference points (RPs) is assumed, as shown in Figure 3.2. A total of 2000 random user locations are simulated. Each of the RPs performs a distance measurement to that user. DME to that user is then simulated, using the RT-based DME model described in the previous chapter, using DME model parameters given in [Ala03]. Three different channel

scenarios are simulated: LOS, OLOS, and mixed LOS/OLOS. The mixed LOS/OLOS scenario is simulated using a binomial random variable, such that the channel is likely to be LOS with probability p , and OLOS with probability $1-p$. The results are presented for the case of $p = 0.3$. System bandwidths in the range of 50 – 1000 MHz are considered for the distance error models [Ala03]. The performance metric is the average estimation error, E_{av} , defined as:

$$E_{av} = E\{|\mathbf{R}_{est} - \mathbf{R}_{act}|\} \quad (3.14)$$

where \mathbf{R}_{act} , and \mathbf{R}_{est} are the actual and estimated locations of a user.

The first set of results in Figure 3.3 and Figure 3.4 show a comparison of the LS and RWGH algorithms for LOS, OLOS and mixed LOS/OLOS scenarios respectively over a 15m x 15m area. Out of these results, we can make two key observations. The first one is that in the LOS channel, there is not a lot of difference between the QoE exhibited by the LS and RWGH algorithms, whereas in the OLOS and mixed LOS/OLOS channels, RWGH is clearly seen to exhibit better performance. This behavior is consistent with the structure of the RWGH algorithm, since in the LOS case, most of the intermediate estimates are likely to have equal residuals, and so using RWGH over the LOS channel is not likely to provide a significant benefit. For the OLOS and mixed LOS/OLOS channels, however, some of the intermediate estimates used in RWGH have much higher residuals, and those intermediate estimates will then be assigned a lower weight, thereby enhancing the performance of the algorithm over such channels.

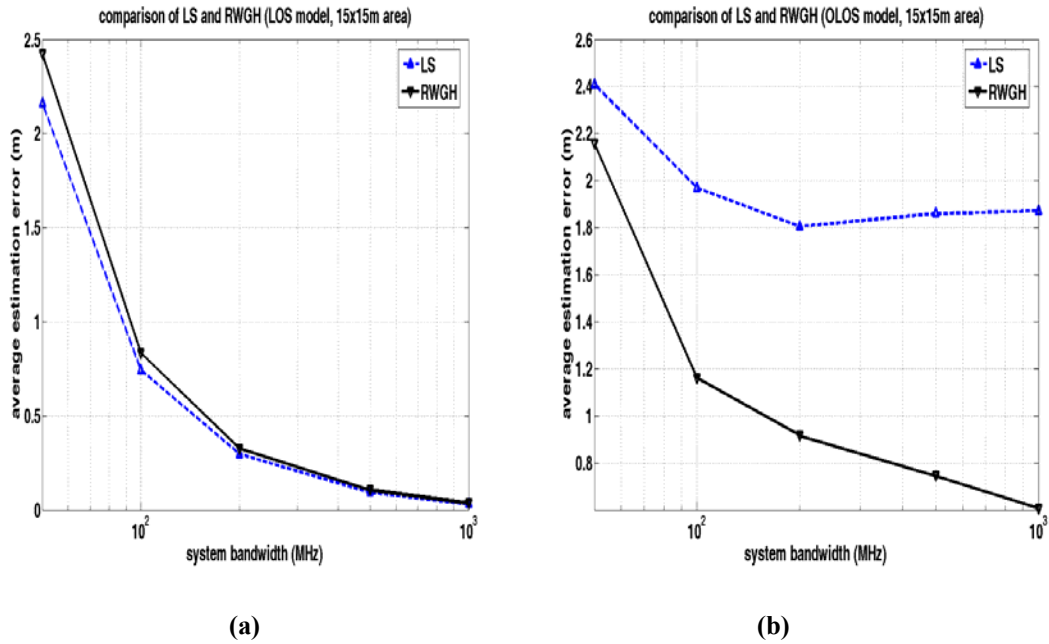


Figure 3.3 LS/RWGH QoE comparison for: (a) LOS channel, (b) OLOS channel

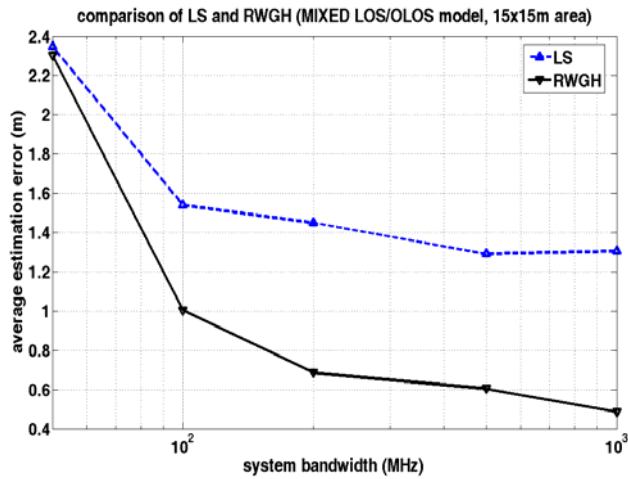


Figure 3.4 LS/RWGH comparison: mixed LOS/OLOS channel

The next set of results compares the performance of the CN algorithm over the LOS, OLOS and mixed LOS/OLOS channels. As can be clearly observed from Figure 3.5, this algorithm exhibits very high average estimation error (i.e. low QoE). A comparison of these results to those in Figure 3.3 through Figure 3.5 reveals that the CN

algorithm exhibits an estimation error approximately 2.5-8 times worse than the error performance provided by LS and RWGH algorithms, depending on the channel scenario and the bandwidth used. The crude nature of the CN algorithm is the principal reason for this behavior, since the algorithm simply estimates the location of the user as the location of the RP that made the minimum distance measurement to the user. While this may be acceptable for some indoor wireless networks (such as wireless LANs), it is clear that a very dense network of reference points may be needed, as we shall see next.

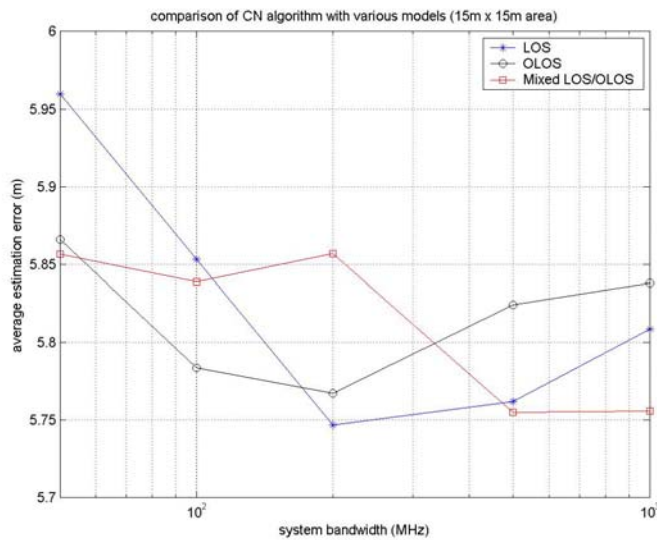


Figure 3.5 QoE comparison for the CN algorithm over the three channel scenarios

In the next set of results, we present a QoE comparison of LS, CN and RWGH algorithms for two different values of node densities, and over the three channel scenarios previously considered. We simulate the different node densities by fixing the number of RPs at four, and then changing the size of the area from 15m x 15m to 30m x 30m. Dividing the number of RPs by the size of the area gives a measure of the node

density. The two node density values are $0.0177 \text{ RPs} / \text{m}^2$ (for the $15\text{m} \times 15\text{m}$ area) and $0.004 \text{ RPs} / \text{m}^2$ (for the $30\text{m} \times 30\text{m}$ area).

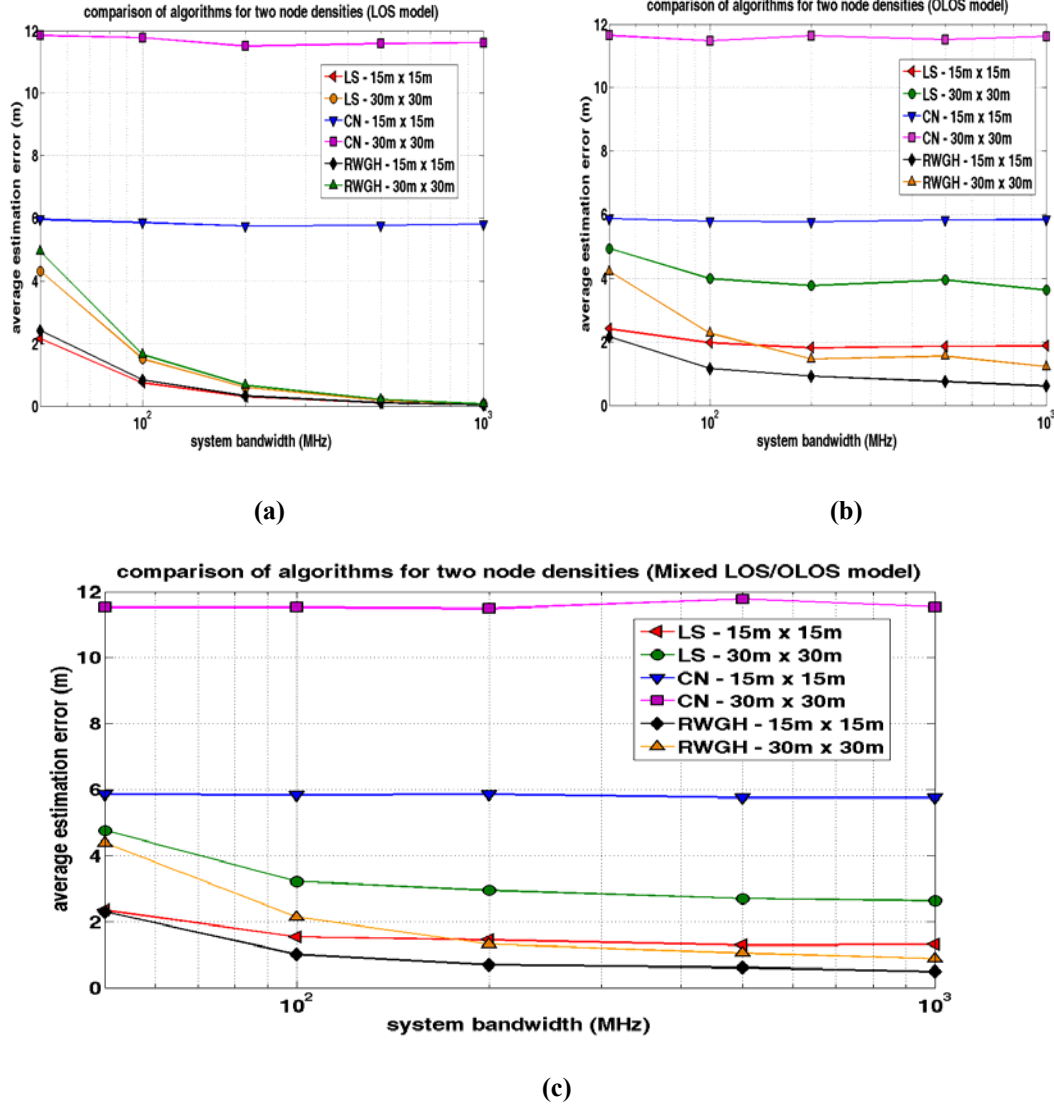


Figure 3.6 QoE comparison of the CN, LS and RWGH algorithms for two different node densities: (a) LOS channel, (b) OLOS channel, (c) mixed LOS/OLOS channel

A close examination of Figure 3.6 reveals that the QoE of all three algorithms degrades to a certain extent when the node density is decreased. What is also interesting is that the degradation seems to happen uniformly, regardless of bandwidth or the

channel scenario. On the basis of these results an *average degradation factor*, K_{av} , has been calculated for all the three algorithms within each channel scenario. These values are tabulated in Table 3-1, and are calculated as follows. For a given algorithm, and channel scenario, the ratio of E_{av} values at 30m x 30m to the values for 15m x 15m are calculated for each measurement bandwidth value. K_{av} is then calculated as the average of all the ratio values. Essentially, K_{av} allows an insight into the amount of performance degradation (i.e. reduction in estimation accuracy indicated by the increase in E_{av}) that can be expected as the size of the area is increased. The exact amount of performance degradation will, of course, vary as a function of the system bandwidth; nevertheless, K_{av} will be helpful in giving a rough idea.

Table 3-1 Average Degradation in Estimation Accuracy

Algorithm	Channel Scenario	K_{av}
LS	LOS	2.011
	OLOS	2.048
	MIXED LOS/OLOS	2.052
RWGH	LOS	2.024
	OLOS	1.920
	MIXED LOS/OLOS	1.897
CN	LOS	2.002
	OLOS	1.991
	MIXED LOS/OLOS	1.991

3.3 Discussion

Based on the results presented in the previous section we can draw a number of conclusions. First, regardless of the particular type of channel scenario, the CN algorithm has the worst performance of the three algorithms considered. This is expected, since the algorithm provides an estimate that is only as accurate as the location of the RP that is closest to the user.

The difference in performance between the LS and RWGH algorithms rapidly diminishes beyond a measurement bandwidth of 100 MHz, for the LOS case. In other words, as long as the system bandwidth is above 100 MHz, RWGH provides no additional advantage from a performance perspective in the LOS case. For the OLOS and mixed LOS/OLOS cases, however, the performance of RWGH is significantly better than that of LS algorithm. This is because the RWGH algorithm is designed to work in unbalanced (OLOS) channel environments.

Based on the distance error model parameters considered in this paper, it can be said that increasing the size of the area over which a user is to be located (while keeping the number and location of RPs fixed) makes the resulting location estimates less accurate. This point makes intuitive sense in that as the area gets larger, the LOS paths from the RP to the user will suffer more path loss, and the OLOS paths will suffer more delay (due to multipath). These factors will affect the TOA measurements, and therefore, the distance measurements that a given RP will make. From the results given in Table 3-1, it can be seen that a four-fold increase in the size of the area translates to an

approximately two-fold increase in estimation error, regardless of the algorithm, and the particular channel scenario.

Chapter 4 Performance of New Algorithms

In the previous chapter, we focused on the performance of existing algorithms for infrastructure-based indoor geolocation. We saw that the CN algorithm had a very poor performance compared with LS and RWGH algorithms, predominantly because of the crude way the location estimate is obtained. In this chapter, we present the Closest Neighbor with TOA Grid (CN-TOAG) algorithm ([Kan04b], [Kan04c]) and compare its performance to existing techniques. We describe the algorithm in section 4.1. In section 4.2, we evaluate its performance. In section 4.3, we present an extension to the CN-TOAG algorithm, known as the Coverage Map Search (CMS) [Kan07] and present some results on its performance in section 4.4.

4.1 Closest-Neighbor with TOA Grid (CN-TOAG) Algorithm

The CN-TOAG algorithm, as its name implies, is related to the CN algorithm which was discussed in section 3.1.1. Consider the regular grid scenario of RPs which was shown previously in Figure 3.1. In such a scenario, we know the *exact* number of the TOA-based distance measurement, assuming that the locations of the RPs are known more or less precisely with respect to a global coordinate system. Specifically, with the CN-TOAG algorithm, the whole area covered by the array of RPs is divided into a grid of points, with each point being equidistant from each of its adjacent neighbors, as shown in Figure 4.1. As can be seen, this is equivalent to subdividing the area covered by the array of RPs into equal-sized squares of size h meters. There is a set of distance

measurements (also known as range measurements) associated with each point on the grid, one from each base station. In our current example, since there are four RPs involved, each point, (x_i, y_j) , on the grid has a vector of four range measurements associated with it. We denote such a vector of range measurements associated with a particular point on the grid by \mathbf{r}_{ij} , and call it the *range signature* associated with the point (x_i, y_j) . Conceptually speaking, having a range signature associated with each point on the grid is almost equivalent to performing TOA-based range measurements to each point on the grid, and we call the overall construct a *TOA grid*.

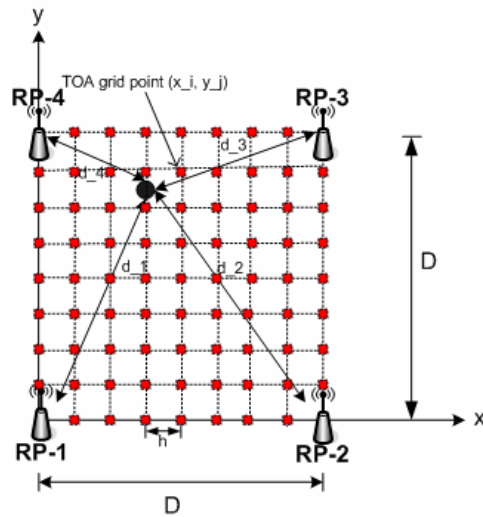


Figure 4.1 An indoor geolocation system showing the TOA grid for the CN-TOAG algorithm

Since the range values forming the range signature for a given point are based on straightforward geometric calculations (assuming the locations of the RPs are known accurately), the range signature is exact. Therefore, the user location can be estimated by comparing the vector of range measurements to the range signature at each point, and

noting the degree of similarity between them. Specifically, for each point on the TOA grid, (x_i, y_j) , an error figure, e_{ij} , is calculated as:

$$e_{ij} = \| \mathbf{D} - \mathbf{r}_{ij} \| \quad (4.1)$$

The estimated location, \mathbf{R}_{est} , is that point, (x_i, y_j) , on the grid which corresponds to the minimum value of e_{ij} . Based on the description above, it is clear that CN-TOAG is an example of a pattern recognition algorithm; however, it does not require fingerprinting for its operation, since the TOA grid can be determined in a purely geometric fashion if the size of the area and the location of the RPs are known.

Another way to look at the CN-TOAG algorithm is to rewrite (4.1) as an objective function to be minimized as follows:

$$e(x, y) = \sqrt{\sum_{k=1}^N \left(d_k - \sqrt{(x - X_k)^2 + (y - Y_k)^2} \right)^2} \quad (4.2)$$

where (X_k, Y_k) are the coordinates of the k -th RP, and d_k is the distance measurement obtained from the k -th RP. The point (x, y) that minimizes (4.2) can then be found by the gradient relationship:

$$\nabla e(x, y) = \mathbf{0} \quad (4.3)$$

Due to the complexity of the objective function in (4.2), (4.3) is difficult to solve analytically. However, it can be solved numerically, and CN-TOAG algorithm can be viewed as such a numerical method. As may be expected, the granularity of the TOA grid, as given by h , is a big determinant of the estimation accuracy for this algorithm.

4.2 Performance Evaluation of CN-TOAG

In this section, the performance of CN-TOAG is compared with the LS and RWGH algorithms under the RT-based DME model discussed in section 2.4.1. The regular grid arrangement of four RPs over an area of size 20m by 20m is assumed, as shown in Fig 3.1. A number of random sensor locations are simulated. For the purposes of this discussion, only the OLOS channel scenario is considered. System bandwidths in the range of 50 – 1000 MHz are considered for the range error models, as given in [Ala03]. The choice of these bandwidth figures for this study is purely arbitrary; these bandwidth values are sufficient to present a good representative sample of the results. There are two performance metrics depicted in the results presented below. The first is the root-mean-square positioning error ($RMSE_{pos}$), defined as:

$$RMSE_{pos} = \sqrt{E\{(\|\mathbf{R}_{est} - \mathbf{R}_{act}\|)^2\}} \quad (4.4)$$

where \mathbf{R}_{act} , and \mathbf{R}_{est} are the actual and estimated locations of a user. The other performance metric is the root-mean-square ranging error ($RMSE_{ran}$), defined as:

$$RMSE_{ran} = \sqrt{E\{(\|\mathbf{d} - \mathbf{d}_{act}\|)^2\}} \quad (4.5)$$

where \mathbf{d}_{act} is the vector of actual (uncorrupted) distance measurements, and \mathbf{d} is the vector of distance measurements that the BSs would report in practice (i.e. the distance measurements corrupted by OLOS channel conditions).

The results are presented in Figure 4.2 through Figure 4.5. In Figure 4.2 through Figure 4.4, the performance of the CN-TOAG algorithm is compared against the LS and RWGH algorithms for three system bandwidth values: 50 MHz, 500 MHz, and 1000

MHz. In each of these figures, the RMSE for ranging, as well as the RMSE for positioning is depicted for each algorithm (the RMSE for ranging and positioning are referred to in the plots as RMSE ‘before’ and ‘after’ positioning respectively).

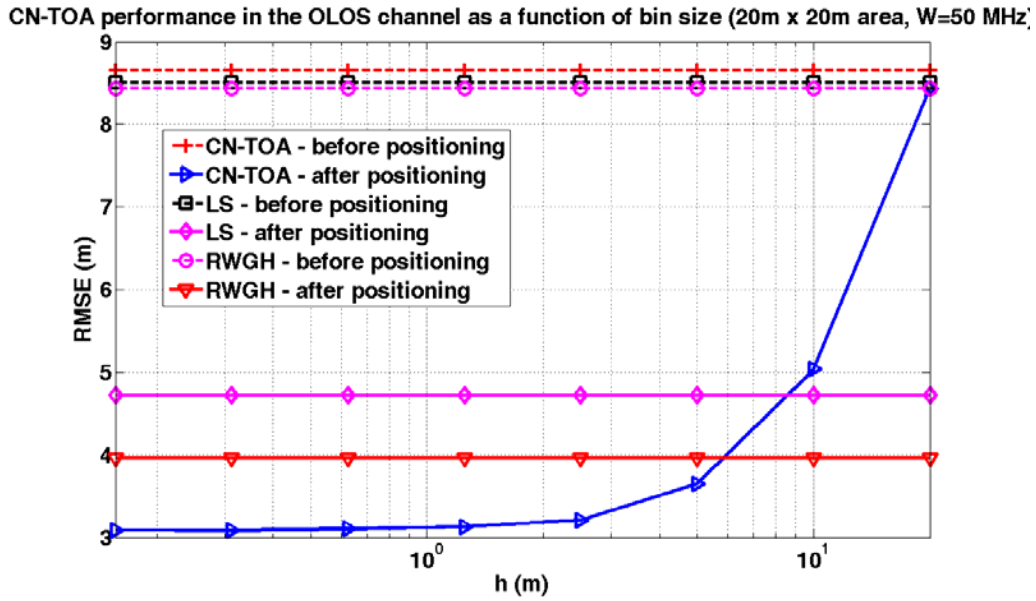


Figure 4.2 Comparison of CN-TOAG performance vs. LS and RWGH algorithms (system bandwidth = 50 MHz) Dashed lines indicate ranging errors.

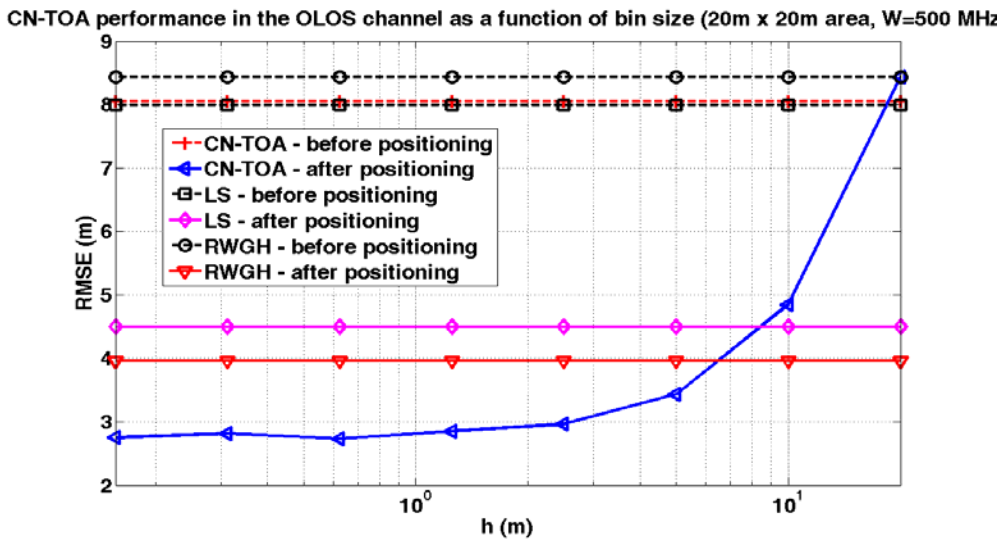


Figure 4.3 Comparison of CN-TOAG performance vs. LS and RWGH algorithms (system bandwidth = 500 MHz). Dashed lines indicate ranging errors.

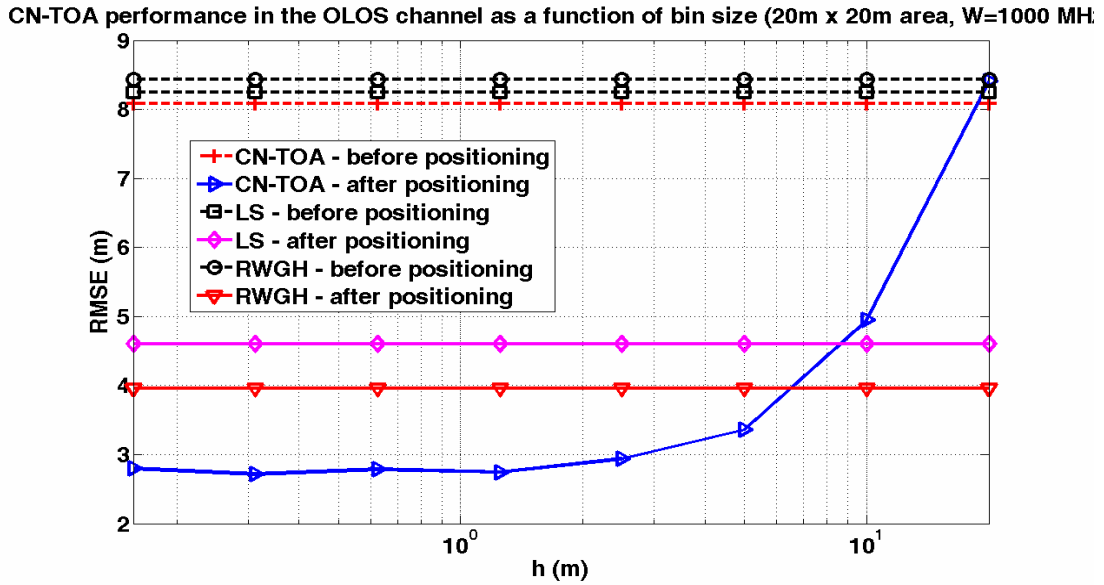


Figure 4.4 Comparison of CN-TOAG performance vs. LS and RWGH algorithms (system bandwidth = 1000 MHz). Dashed lines indicate ranging errors.

From the results of Figure 4.2 through Figure 4.4, we can observe that CN-TOAG can achieve exactly the same level of performance as the LS and RWGH algorithms in the indoor OLOS environment, provided that the TOA grid is granular enough (i.e. h is small enough). However, the performance does not appear to improve appreciably beyond a certain value of h . For the system scenario considered for this evaluation, this value of h is about 1.25 m. We also observe that, regardless of the system bandwidth used to make the range measurements, CN-TOAG can achieve exactly the same performance as LS using $h = 8.5$ m. In the case of RWGH, the grid has to be only slightly more granular for CN-TOAG to achieve the same performance, with h in the 6 – 6.5 m range. If h is below this value, then CN-TOAG can actually outperform both LS and RWGH by about 38% and 12% respectively.

In the next set of results (Figure 4.5), we study the performance of the CN-TOAG algorithm in the presence of the RT-based DME model to see how its performance varies as a function of the system bandwidth.

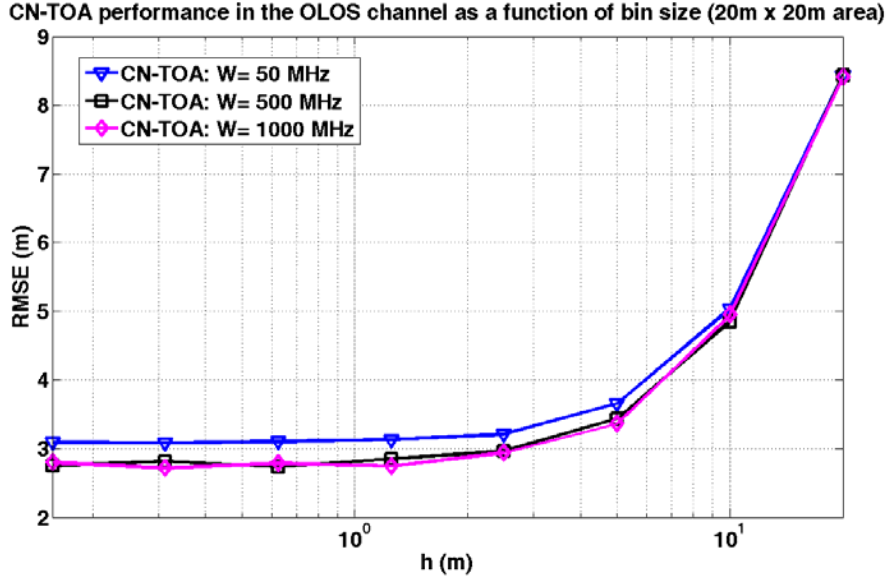


Figure 4.5 CN-TOAG performance at the various bandwidth values

From the results, we note that the CN-TOAG performance essentially stays the same between system bandwidth values of 500 and 1000 MHz. As the bandwidth of the system is increased, the range measurements themselves would be more accurate, which is normally expected to translate to a more accurate location estimate. However, for the CN-TOAG algorithm, the results suggest that beyond a certain point, increasing the system bandwidth any further will not necessarily result in greater accuracy in the location estimates. This issue has been investigated and found to be a consequence of the RT-based DME model in the OLOS case. Specifically, the overall variance of the OLOS-based DME can be calculated using equation (2.8) as:

$$\text{Var}\{\gamma_{O,w}\} = \frac{W_{G,w}\sigma_{O,w}^2\lambda_w^2 + 2W_{Exp,w} - W_{Exp,w}^2}{\lambda_w^2} \quad (4.6)$$

This relationship is plotted as a function of the bandwidth, w in the 50 – 1000 MHz range using the values of the parameters of the distributions given in [Ala03], as shown in Figure 4.6 below. In essence, since the overall variance stays about the same for bandwidth values greater than 100 MHz, the performance of CN-TOAG stays unchanged as well.

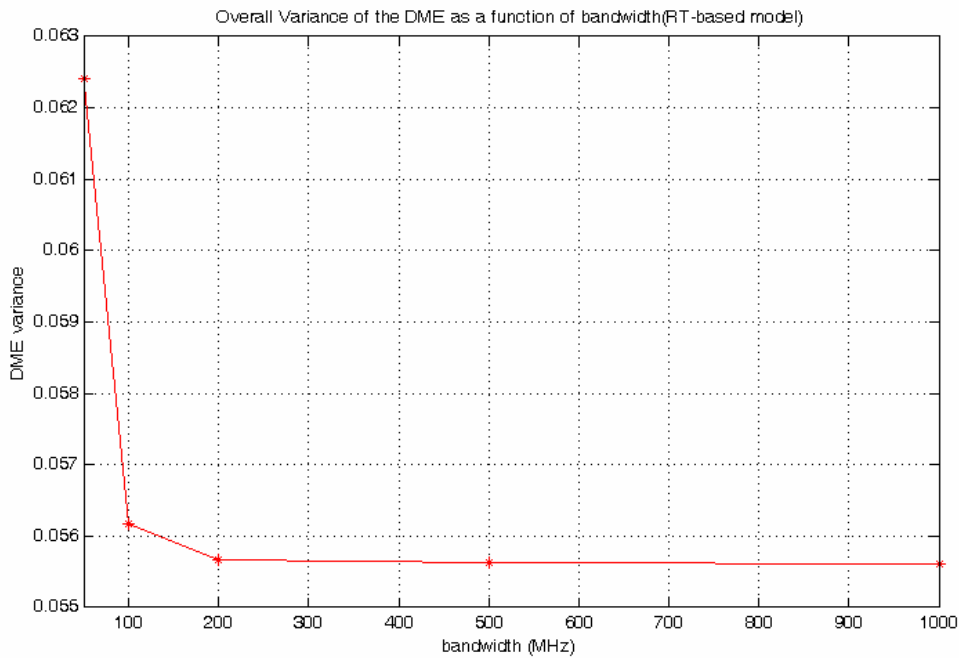


Figure 4.6 Overall variance of the RT-based DME model (OLOS case)

4.2.1 Complexity Analysis for CN-TOAG versus LS and RWGH

In this section, we present an analysis of the computational complexity of CN-TOAG versus LS and RWGH algorithms. We employ the term “computational complexity” to refer to the number of iterations required by each algorithm in order to reach a location estimate. We begin with the Davidon LS algorithm. As described in section 3.1.2., this algorithm requires an evaluation of the objective function and its

gradient. For an N -dimensional quadratic objective function given by (3.1), where N is the number of RPs, a total of $Q = N + 2$ iterations (i.e. evaluations of the gradient) are required to reach convergence and obtain the LS estimate [Dav68]. Therefore, the total number of iterations required for a LS estimate is

$$Q_{LS} = N + 2 \quad (4.7)$$

The RWGH algorithm, as described in section 3.1.3, requires that the number of distance measurements be greater than three, i.e. $N > 3$, in order to successfully combat the effects of OLOS conditions [Che99]. This algorithm requires that a total of $P = \sum_{i=3}^N \binom{N}{i}$ intermediate LS estimates be computed, one for each combination of distance measurements. Since we use the Davidon LS algorithm for this dissertation to obtain these intermediate LS estimates, the total number of iterations required to obtain an RWGH estimate is

$$Q_{RWGH} = \left(\sum_{i=3}^N \binom{N}{i} \right) (N + 2) \quad (4.8)$$

The CN-TOAG algorithm, on the other hand, is an example of a pattern recognition algorithm that relies on the TOA grid. We assume that we have a TOA grid of size $M = K \times L$ points, as shown in Figure 4.1, where K is the number of rows and L is the number of columns. CN-TOAG requires that we first evaluate the value of the error norm function given by (4.1) at each point on the TOA grid. This will require a total of M evaluations of the error norm function. After this step, CN-TOAG conducts a search on the two-dimensional grid to find the point with the minimum error norm. This is done in a two-step manner. First, the minimum value along each row is found, which

would require a total of $M = KL$ iterations. The result of this step would be an $L \times 1$ vector of minimum values. As a second step, the algorithm would perform a search on this $L \times 1$ vector to find the point with the minimum error norm, which would require L iterations. Therefore, the total number of iterations to obtain a location estimate from the CN-TOAG algorithm is

$$Q_{CNTOAG} = M + (M + L) = 2M + L \quad (4.9)$$

We are now in a position to perform a computational complexity comparison among the three algorithms. As can be seen from (4.7)-(4.9), a three-way comparison of these algorithms is made challenging by the fact that there is no common parameter that determines the required number of iterations for all three of them. This is not surprising, as CN-TOAG belongs in a different class of algorithms than LS and RWGH. LS and RWGH exploit the geometric relationship between the user location and the RP locations, embodied in the objective function of (3.1), in order to compute the location estimate. CN-TOAG, on the other hand, computes a location estimate using pattern recognition techniques. However, a limited comparison is made possible by examining the results of Figure 4.4. In this figure, we see that CN-TOAG can achieve the same performance as LS, assuming that the TOA grid spacing, $h = 8.5$ m, assuming a 20m x 20m room, with four RPs. For this case, the required size of the TOA grid can be found as

$$K = L = \left\lceil \frac{20}{8.5} \right\rceil = 3 \quad (4.10)$$

where $\lceil \cdot \rceil$ represents the ceiling operator.

Since we assume four RPs in this scenario, i.e. $N = 4$, we can readily see from (4.7) that the number of iterations required to produce the LS estimate is

$$Q_{LS} = N + 2 = 6 \quad (4.11)$$

while the number of iterations required to compute the CN-TOAG estimate can be found using (4.9) and (4.10) to be

$$Q_{CNTOAG} = 2M + L = 21 \quad (4.12)$$

In a similar fashion, we can compare the computational complexity of CN-TOAG versus the RWGH algorithm. Referring to Figure 4.4, we see that CN-TOAG can achieve the same performance as RWGH, assuming that the TOA grid point spacing is such that $h = 6.5$ m. In a similar fashion, we see that the required TOA grid size is

$$K = L = \left\lceil \frac{20}{6.5} \right\rceil = 4 \quad (4.13)$$

The required number of iterations to obtain the RWGH estimate can be found using (4.8) as

$$Q_{RWGH} = 30 \quad (4.14)$$

Similarly, we can see that the number of iterations required to obtain the CN-TOAG estimate is found from (4.9) as

$$Q_{CNTOAG} = 36 \quad (4.15)$$

From the results and the analysis presented above, it is clear that CN-TOAG can achieve better performance than LS and RWGH algorithms; however, this improvement comes at the expense of additional computational complexity. We also note from these results that channel conditions do not really affect the computational complexity, since

these three algorithms are not “channel aware”, i.e. they do not take any special action based on the channel conditions.

4.3 Coverage Map Search (CMS) Algorithm

The CMS algorithm is conceptually based on the Closest Neighbor with TOA Grid (CN-TOAG) algorithm [Kan07]. Like CN-TOAG, the CMS algorithm is dependent on a mathematical construct known as a *TOA Grid*, which was discussed in the previous chapter. The general system scenario is as shown in Figure 4.7 below, where a regular arrangement of reference points (RPs) is assumed. Each RP performs a TOA-based range measurement to a user to be located.

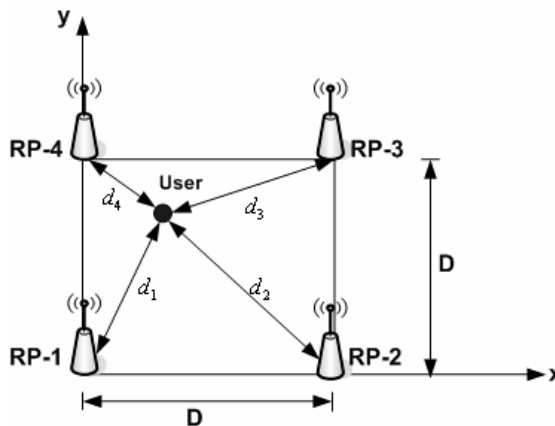


Figure 4.7 General system scenario used to develop the CMS algorithm

In a realistic indoor environment, there will be deficiencies in coverage (termed as *coverage holes*) throughout the area covered by the RPs, as depicted in Figure 4.8 below. This means that a valid range measurement from every RP cannot be guaranteed at every point. For example, with the scenario depicted in Figure 4.8, there will be areas

where only three or fewer range measurements are available. This essentially rules out the applicability of more conventional algorithms, such as least-squares techniques, which require a minimum of three range measurements in order to function properly. It should be emphasized at this juncture that this scenario assumes *averages* for the coverage radii for the four RPs (allowing for factors such as shadow fading).

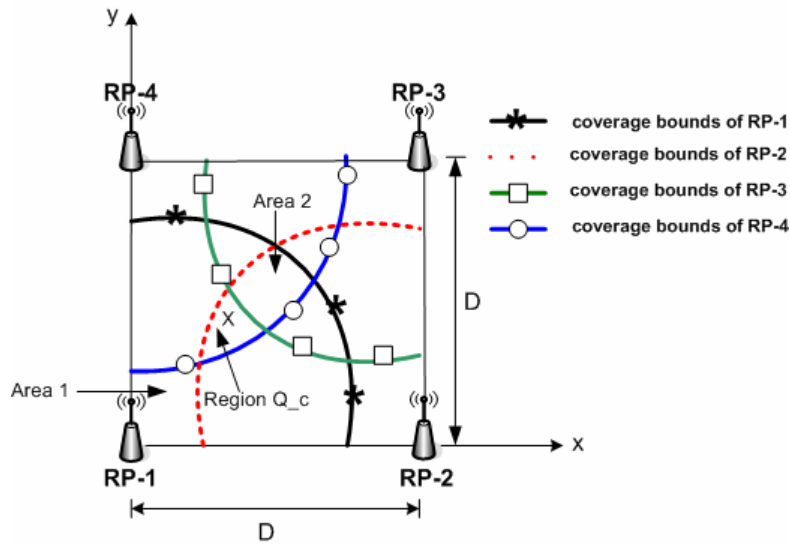


Figure 4.8 Illustration of partial coverage for the CMS algorithm

It should be noted that the deficiencies in the range measurements follow a specified pattern. For example, in the area marked ‘Area 1’ in Figure 4.8, a user would only be able to communicate with RP-1. Therefore, as a refinement on the CN-TOAG algorithm, we define a so-called *coverage signature*, C , which is an array of all RPs that can communicate with the user at a specific point. For example, at any point within area marked ‘Area 1’, $C = [1, -1, -1, -1]^T$, where -1 indicates that the user cannot communicate with a particular RP and the superscript T denotes the transpose operation. In the current example, this implies that the user can only communicate with, and obtain

a range measurement from RP-1. Similarly, for all points in the area marked ‘Area 2’ in Figure 4.8, $\mathbf{C} = [1, 2, 3, 4]^T$, indicating that the user can communicate with all four RPs in that area. It is possible to characterize an entire area with a two-dimensional array of \mathbf{C} vectors which, for the purposes of this discussion, we call a *coverage map*.

It is clear that observations of \mathbf{C} can provide valuable information in locating a user, and this is the idea behind the CMS algorithm. In essence, the algorithm exploits the knowledge about missing range measurements to narrow down the user’s location to a specific area, and finally estimate it. In other words, the CMS algorithm operates on the premise that *the lack of information is, in itself, information that can be exploited*. Specifically, the algorithm works as follows.

For a given vector of range measurements, a pattern is derived. For example, suppose a sensor is located at point X, as shown in Figure 4.8. At this point, the sensor can only communicate with RPs 1, 2, and 4. Therefore, the range measurement vector, $\mathbf{D} = [d_1, d_2, -1, d_4]^T$, where -1 refers to a missing range measurement from RP-3 due to coverage limitations. For the current example, the CMS algorithm would translate this to an equivalent representation in the \mathbf{C} vector space as

$$\mathbf{C}_m = [1, 2, -1, 4]^T \quad (4.16)$$

The algorithm then searches the coverage map for a region, Q_c , which is a subset, Q , of all points within the area, A , where the coverage signatures match \mathbf{C}_m . In other words:

$$Q_c = \{Q \subset A : \mathbf{C} = \mathbf{C}_m\} \forall \mathbf{C} \quad (4.17)$$

In our current example, the Q_c region is as shown in Figure 4.8.

Based on the coordinates of the different points within Q_c , and the coordinates of the APs, a range signature, $\mathbf{Z}(x,y)$, can be computed for each point (x,y) based on purely geometrical considerations, just as in the CN-TOAG algorithm. The range measurement vector, \mathbf{D} , is then compared with all the range signatures to find the point, $\hat{\mathbf{r}} = (\hat{x}, \hat{y})^T$, where \mathbf{Z} most closely approximates \mathbf{D} . In essence, this is equivalent to minimizing an objective function with the additional condition that the search for the minimum is confined to the region Q_c . In other words:

$$\hat{\mathbf{r}} = \arg \min_{\forall \mathbf{r} \in Q_c} e(x, y) \quad (4.18)$$

where $e(x, y)$ is the objective function defined for CN-TOAG in (4.2).

The primary advantage of the CMS algorithm is that it can be used with any number of range measurements, whereas other algorithms such as least-squares (LS) require a minimum of three range measurements. The main characteristic of the algorithm is that it requires a central computing entity in the network to generate the coverage map, and perform the search for the minimum. Although the algorithm has been presented in terms of the simplified coverage scenario of Figure 4.8, it is readily applicable to more realistic coverage scenarios if the coverage map is generated using any accurate indoor radio propagation model [Pah05].

4.4 Performance Evaluation for the CMS Algorithm

The performance of the CMS algorithm has been evaluated through simulations. The regular grid arrangement of four base stations over an area of size D m by D m is assumed, as shown in Figure 4.7. For the purposes of this study, D values of 20 m and 40 m were considered to simulate two different node densities. A number of random user locations are simulated. Each of the RPs performs a distance measurement to the user, to which we add DME in accordance with the RT-based DME model [Ala03]. For the purposes of this paper, only the OLOS channel scenario is considered. System bandwidths in the range of 50 – 1000 MHz are considered for the range error models. In order to come up with a realistic coverage map, the following path loss model was used for the maximum allowable path loss, L_p [Pah05]:

$$L_p = L_o + 10\alpha \cdot \log_{10}(d) + \eta \quad (4.19)$$

where:

L_o : 1-meter intercept

α : A slope factor that depends on the building

d : distance from the transmitter to the receiver location

η : Lognormal shadowing component

For the path loss model, the following typical values were considered:

$$L_o = -42 \text{ dBm}$$

$$\alpha = 3$$

$$L_{p,max} = 110 \text{ dB}$$

The shadowing component in the model was simulated with a zero-mean lognormal random variable with $\sigma = 8$ dB. For the grid granularity parameter, h , a value of 0.625 m was used, since it was noted in previous work ([Kan04b]) that increasing h beyond this value did not noticeably increase the estimation accuracy.

The performance metric used is the root-mean-square positioning error ($RMSE_{pos}$), defined as:

$$RMSE_{pos} = \sqrt{E\{(\|\mathbf{R}_{est} - \mathbf{R}_{act}\|)^2\}} \quad (4.20)$$

where \mathbf{R}_{act} , and \mathbf{R}_{est} are the actual and estimated locations of a user respectively.

For the first set of results (Figure 4.9 and Figure 4.10) we explore the relationship between coverage radius, R , of the RPs, and the performance of the algorithm. Figure 4.9 displays the results for a 20m x 20m area, and Figure 4.10 displays the results for 40m x 40m area. Results are presented for values of the system bandwidth (referred to as w in the figures) in the range 50 – 1000 MHz. A number of observations can be made with regard to these results.

1. The performance of the CMS algorithm does not seem to change a lot as the bandwidth is increased. This is actually a consequence of the RT-based DME model, which was used for this evaluation. For this model, the overall variance of the DME for this model does not change a lot beyond 50 MHz (see Figure 4.6).
2. For a given system bandwidth, there appears to be a value of the RP coverage radius, R , for which the RMSE is lowest. Depending on the size of the area, this value can range from 17.5 m to 35 m, which is almost of the order of the size of the area, i.e. $R \approx D$, which implies $\alpha \approx 1$. This observation can be explained in the

following way. For these values of R , the size of the area where only a single RP can be observed is actually very small, and the size of the area of no coverage (i.e. where the user would not be able to observe any RPs) is zero. Therefore, even under the worst-case scenario where the user was only able to contact a single RP, the size of the area over which the algorithm has to search for a solution is very small, which prevents large fluctuations in the final location estimate.

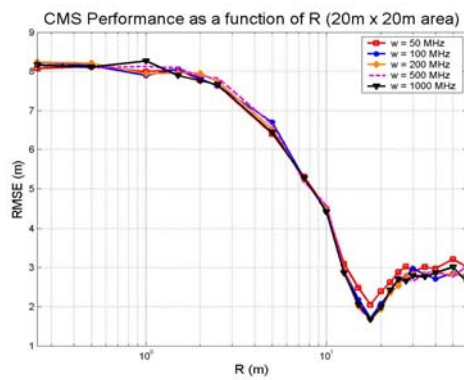


Figure 4.9 CMS Performance comparison as a function of R for system bandwidth, w , in the range 50-1000 MHz

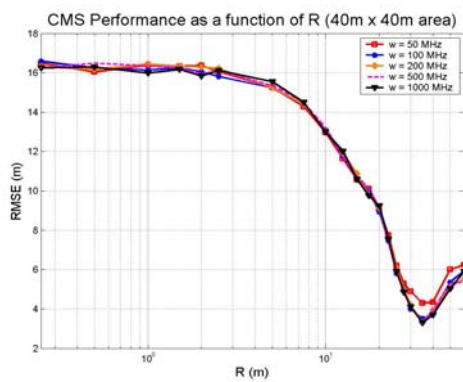


Figure 4.10 CMS performance as a function of R over a larger area for system bandwidth, w , in the range 50-1000 MHz

In Figure 4.11, we show the CMS performance when used with a coverage map that is generated with a path loss model, the parameters of which were presented earlier. RT-based DME model is again used for this case, and the node density is varied by changing the size of the area from 20m x 20m to 40m x 40m size. These results clearly indicate that regardless of the bandwidth, the performance generally degrades by a factor of two, when the size of the area is increased by a factor of four (which also decreases the node density by the same amount). This is consistent with the findings of chapter 3, which were also obtained with the RT-based DME model.

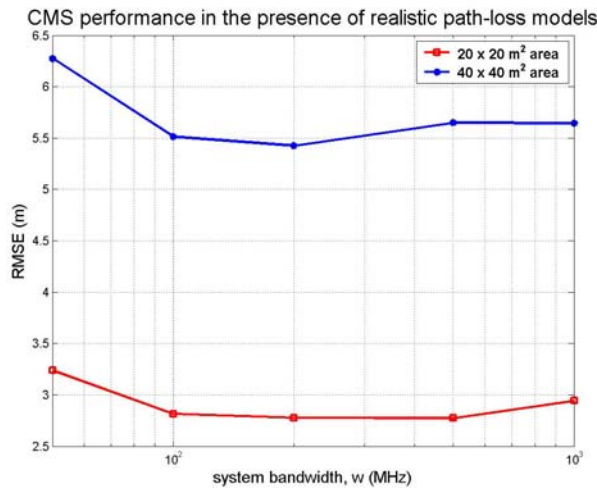


Figure 4.11 CMS performance in the presence of realistic path loss models (20 x 20 m² vs. 40 x 40 m² area)

Chapter 5 Partial Coverage Analysis

As we have noted in section 4.4 on the CMS algorithm, QoE in partial coverage conditions varies with the size of the coverage radius, R in relation to the dimensions of the area, D , i.e the factor α . This makes intuitive sense, because as α increases, more and more RPs can be contacted by the user to make distance measurements, and therefore, a more accurate location estimate becomes possible. Therefore, the logical question is: what is the number of RPs that can be observed by a user at any point in the area, and how does that number vary as a function of α ? Before we attempt to answer this question, however, we will pose another one: why is it important to answer this question and what does it have to do with the theme of this dissertation? The basic reason is that the concept of partial coverage (as described by the parameter α) and that of node density (as described by the parameter ρ) are related as we have noted in chapter 2. Therefore, if we know how the number of RPs observable by the user varies as a function of α , we can use this to set up an analytical framework for the analysis of node density effects on infrastructure-based indoor geolocation systems. In this chapter, we present a statistical analysis that answers this question. The results of this analysis will be used in some of the derivations of the QoE bounds which are discussed in chapter 7.

5.1 Statistical Behavior of the QoE Under Partial Coverage

In this system scenario, we show four RPs, all of which have the same *average* coverage radius, R . Even though R is a function of the transmitter power, as well as the

shadow fading characteristics (among other factors) this is certainly a reasonable assumption in practice, since a grid-based deployment of RPs generally would use transceivers with very similar characteristics.

First, we define the *coverage probabilities* $P_i(\alpha)$ as the probability of the user seeing i RPs (where $i \in \{0,1,2,3,4\}$) as a function of α . Referring to Figure 5.1, we see that as the value of α changes, the amount of overlap between the coverage areas of the respective RPs will also change, and that affects the values of the probabilities $P_i(\alpha)$. Therefore, a reasonable approach to the analysis of these probabilities involves the calculation of the size of the areas where a given number of RPs can be observed, and then normalizing that area by the total size of the area covered, which is D^2 , since $P_i(\alpha) \leq 1.0$ by definition. For example, in order to calculate $P_2(\alpha)$, we would calculate the total area where only two RPs can be observed as a function of α , and then normalize that area by D^2 . The end results of this calculation are presented for the following intervals for α .

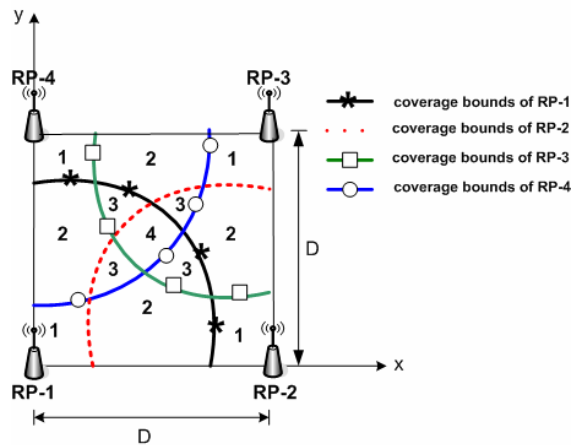


Figure 5.1 System scenario for the statistical analysis of the QoE in partial coverage. The numbers in the various areas represent the number of RPs that are likely to be observed throughout that area.

5.2 Coverage Probabilities

Using the approach that has been outlined in the previous section, it is possible to calculate the coverage probabilities through area calculations. The results are given for the following intervals of values for α and the derivation of the results can be found in Appendix 5.A at the end of this chapter.

Interval I: $0.0 \leq \alpha \leq 0.5$

For these values of α , no more than one RP can be seen at any point in the area.

Therefore, we have:

$$P_2 = P_3 = P_4 = 0 \quad (5.1)$$

$$P_0 = 1 - \pi\alpha^2 \quad (5.2)$$

$$P_1 = \pi\alpha^2 \quad (5.3)$$

Interval II: $0.5 \leq \alpha \leq (\sqrt{2}/2)$

For this interval, the overlap between coverage areas will be such that two RPs can be observed at some points in the area, but there will be no points where three or more RPs can be observed. Therefore, we have:

$$P_3 = P_4 = 0 \quad (5.4)$$

$$P_0 = 1 - \pi\alpha^2 + 4\alpha^2 \tan^{-1}\left(\sqrt{4\alpha^2 - 1}\right) - \sqrt{4\alpha^2 - 1} \quad (5.5)$$

$$P_1 = \pi\alpha^2 - 8\alpha^2 \tan^{-1}\left(\sqrt{4\alpha^2 - 1}\right) + 2\sqrt{4\alpha^2 - 1} \quad (5.6)$$

$$P_2 = 4\alpha^2 \tan^{-1}\left(\sqrt{4\alpha^2 - 1}\right) - \sqrt{4\alpha^2 - 1} \quad (5.7)$$

Interval III: $(\sqrt{2}/2) \leq \alpha \leq 1.0$

For this interval, the overlap between coverage areas is such that three RPs can be seen, and the area of no coverage is reduced to zero. Therefore, we have:

$$P_0 = 0 \quad (5.8)$$

$$\begin{aligned} P_1 = & 1 - 8 \left[\frac{\alpha^2 \theta_x}{2} - \frac{1}{4} \sqrt{\alpha^2 - \frac{1}{4}} \right] \\ & + \left[2b \sqrt{a^2 - \frac{b^2}{4}} + 4\alpha^2 \theta_3 - 4a \sqrt{\alpha^2 - \frac{a^2}{4}} - 2\alpha^2 \theta + 2b \sqrt{\alpha^2 - \frac{b^2}{4}} \right] \\ & + 12 \left[\frac{\alpha^2 \theta}{2} - 2 \sqrt{\beta_1(\alpha) \beta_2(\alpha) \beta_3(\alpha) \beta_4(\alpha)} \right] \end{aligned} \quad (5.9)$$

$$\begin{aligned} P_2 = & 8 \left[\frac{\alpha^2 \theta_x}{2} - \frac{1}{4} \sqrt{\alpha^2 - \frac{1}{4}} \right] \\ & - \left[4b \sqrt{a^2 - \frac{b^2}{4}} + 8\alpha^2 \theta_3 - 8a \sqrt{\alpha^2 - \frac{a^2}{4}} - 4\alpha^2 \theta + 4b \sqrt{\alpha^2 - \frac{b^2}{4}} \right] \\ & - \left[8\alpha^2 \theta - 32 \sqrt{\beta_1(\alpha) \beta_2(\alpha) \beta_3(\alpha) \beta_4(\alpha)} \right] \end{aligned} \quad (5.10)$$

$$\begin{aligned} P_3 = & 4 \left[\frac{b}{2} \sqrt{a^2 - \frac{b^2}{4}} + 2 \left\{ \frac{\alpha^2 \theta_3}{2} - \frac{a}{2} \sqrt{\alpha^2 - \frac{a^2}{4}} \right\} \right] \\ & - 4 \left[\frac{\alpha^2 \theta}{2} - \frac{b}{2} \sqrt{\alpha^2 - \frac{b^2}{4}} \right] \end{aligned} \quad (5.11)$$

$$P_4 = 4 \left[\frac{\alpha^2 \theta}{2} - 2 \sqrt{\beta_1(\alpha) \beta_2(\alpha) \beta_3(\alpha) \beta_4(\alpha)} \right] \quad (5.12)$$

where:

$$\theta = \frac{\pi}{2} - 2 \tan^{-1} \left(\frac{1}{2\sqrt{\alpha^2 - \frac{1}{4}}} \right) \quad (5.13)$$

$$\theta_3 = \frac{\pi}{2} - \left[\tan^{-1} \left(\frac{1 - \sqrt{2\alpha^2 - 1}}{\sqrt{2\alpha^2 + 2(2\alpha^2 - 1)^{1/2}}} \right) + \tan^{-1} \left(2\sqrt{\alpha^2 - \frac{1}{4}} \right) \right] \quad (5.14)$$

$$\beta_1(\alpha) = \left(\frac{\alpha}{2} + \frac{1}{2}\sqrt{\alpha^2 - \frac{1}{4}} \right) + \left(\frac{\sqrt{2}-1}{4} \right) \quad (5.15)$$

$$\beta_2(\alpha) = \left(-\frac{\alpha}{2} + \frac{1}{2}\sqrt{\alpha^2 - \frac{1}{4}} \right) + \left(\frac{\sqrt{2}-1}{4} \right) \quad (5.16)$$

$$\beta_3(\alpha) = \left(\frac{\alpha}{2} - \frac{1}{2}\sqrt{\alpha^2 - \frac{1}{4}} \right) + \left(\frac{\sqrt{2}+1}{4} \right) \quad (5.17)$$

$$\beta_4(\alpha) = \left(\frac{\alpha}{2} + \frac{1}{2}\sqrt{\alpha^2 - \frac{1}{4}} \right) - \left(\frac{\sqrt{2}+1}{4} \right) \quad (5.18)$$

$$a = 2\alpha \sin \left(\frac{\theta_3}{2} \right) \quad (5.19)$$

$$b = 2\alpha \sin \left(\frac{\theta}{2} \right) \quad (5.20)$$

$$\theta_x = \tan^{-1} \left(\frac{1}{2\sqrt{\alpha^2 - \frac{1}{4}}} \right) \quad (5.21)$$

Interval IV: $1.0 \leq \alpha \leq \frac{\sqrt{5}}{2}$

Over this interval, the overlap between coverage areas will be such that:

$$P_0 = P_1 = 0 \quad (5.22)$$

and P_4 will follow the same expression as given in (5.12) . Therefore, all we need to do is derive expressions for P_2 and P_3 .

From area calculations, we find that:

$$P_2 = 4 - 4\sqrt{\alpha^2 - 1} - 2\pi\alpha^2 + 4\alpha^2 \tan^{-1}\left(\sqrt{4\alpha^2 - 1}\right) + 4\alpha^2 \tan^{-1}\left(\sqrt{\alpha^2 - 1}\right) - 2\sqrt{\alpha^2 - \frac{1}{4}} \quad (5.23)$$

$$P_3 = 1 - \left[4 - 4\sqrt{\alpha^2 - 1} - 2\pi\alpha^2 + 4\alpha^2 \tan^{-1}\left(\sqrt{4\alpha^2 - 1}\right) + 4\alpha^2 \tan^{-1}\left(\sqrt{\alpha^2 - 1}\right) - 2\sqrt{\alpha^2 - \frac{1}{4}} \right] - \left[2\alpha^2\theta - 8\sqrt{\beta_1(\alpha)\beta_2(\alpha)\beta_3(\alpha)\beta_4(\alpha)} \right] \quad (5.24)$$

and θ is given by equation (5.13). The functions $\beta_1(\alpha)$ through $\beta_4(\alpha)$ are defined by equations (5.15) through (5.18) respectively.

Interval V: $\frac{\sqrt{5}}{2} \leq \alpha \leq \sqrt{2}$

For these values of α , the overlap between neighboring RPs is such that three or more references can be seen throughout the entire area. Therefore:

$$P_0 = P_1 = P_2 = 0 \quad (5.25)$$

and

$$P_3 = 4 - 4\sqrt{\alpha^2 - 1} - 2\alpha^2\gamma \quad (5.26)$$

$$P_4 = -3 + 4\sqrt{\alpha^2 - 1} + 2\alpha^2\gamma \quad (5.27)$$

where γ is defined as:

$$\gamma = \frac{\pi}{2} - 2 \tan^{-1}(\sqrt{\alpha^2 - 1}) \quad (5.28)$$

Interval VI: $\alpha \geq \sqrt{2}$

For such values of α , all 4 RPs can be seen at all points throughout the area. Therefore, we conclude that

$$P_0 = P_1 = P_2 = P_3 = 0 \quad (5.29)$$

$$P_4 = 1 \quad (5.30)$$

Figure 5.2 below shows the above results for all six intervals plotted as a function of α .

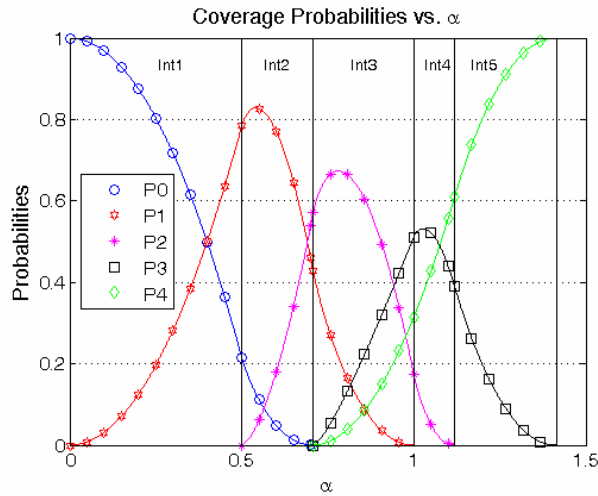


Figure 5.2 Coverage probabilities plotted as a function of α

Appendix 5.A Coverage Probability Analysis

In this appendix, we present derivations of the coverage probabilities, $P_i(\alpha)$ ($0 \leq i \leq 4$) for the different intervals of α .

Interval I: $0.0 \leq \alpha \leq 0.5$

This situation is depicted in Figure A.1 below, where we assume four RPs placed at the at the four corners of a square room. With no loss of generality, we can assume that the dimension of the room is $D = 1$. In this case, from the definition of α , we can say that $R = \alpha$. In this as well as all other intervals discussed below, the RPs are assumed to be at four corners with coordinates $[0,0]$, $[0,1]$, $[1,0]$ and $[1,1]$.

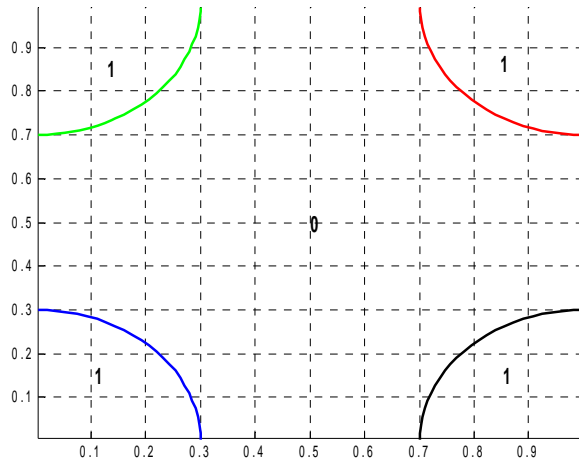


Figure A.1 Showing the coverage probabilities for interval 1

For this case, it is clear from the above figure that:

$$P_2 = P_3 = P_4 = 0 \quad (\text{A.1})$$

since there is no possible way the user can see more than one RP under such coverage conditions. We can calculate P_0 and P_1 by appropriate area calculations as follows. For

each probability, we calculate the total area where the user can see the appropriate number of RPs, and then normalize that area by the total area (which is D^2), since probabilities, by definition have to be between zero and one. This same methodology will be used for the rest of the probabilities in other intervals as well.

Since $R = \alpha$, we can write:

$$P_1 = 4 \left(\frac{\pi \alpha^2}{4} \right) = \pi \alpha^2 \quad (\text{A.2})$$

And since $P_0 + P_1 = 1$

$$P_0 = 1 - P_1 = 1 - \pi \alpha^2 \quad (\text{A.3})$$

Interval II: $0.5 \leq \alpha \leq (\sqrt{2}/2)$

This case is shown in Figure A.2 below. The overlap in coverage is now at a point where two RPs can be seen in some areas. The area of no coverage is seen to shrink and will be zero when $\alpha = \sqrt{2}/2$.

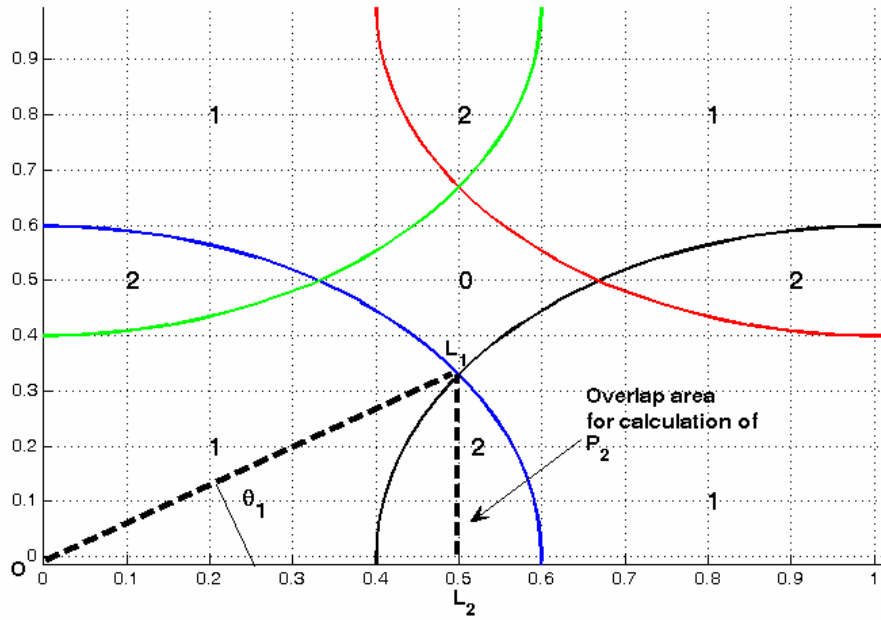


Figure A.2 Showing the coverage scenario for interval II

In order to calculate P_2 , we will use the point marked L_1 and the angle θ_1 which that point makes with the RP at point $[0,0]$. Specifically, we are concerned with calculating the overlap area, A_o , as shown in Figure A.2 above. Under the idealized coverage scenario we are considering, it is clear that:

$$A_o = P_2 / 4 \quad (\text{A.4})$$

From the geometry shown in Figure A.2, we observe that:

$$A_o = 2(A_\theta - A_t) \quad (\text{A.5})$$

Where A_θ is the area of the circular sector of angle θ_1 and A_t is the area of the triangle $\triangle OL_1L_2$. In order to calculate these areas, we first need to determine the

coordinates of the point L_1 , where the two circles intersect. Using the standard equations of the circles, we can show that the coordinates (x_1, y_1) of the point L_1 are:

$$x_1 = \frac{1}{2} \quad (\text{A.6})$$

$$y_1 = \sqrt{\alpha^2 - \frac{1}{4}} \quad (\text{A.7})$$

assuming $D = I$, which implies that $R = \alpha$. From this, we can write:

$$\theta_1 = \tan^{-1} \left(2\sqrt{\alpha^2 - \frac{1}{4}} \right) = \tan^{-1} \left(\sqrt{4\alpha^2 - 1} \right) \quad (\text{A.8})$$

which leads to:

$$A_\theta = \frac{1}{2} \alpha^2 \theta_1 = \frac{1}{2} \alpha^2 \tan^{-1} \left(\sqrt{4\alpha^2 - 1} \right) \quad (\text{A.9})$$

From standard geometrical formulas, we can also calculate the area of the triangle as:

$$A_t = \frac{1}{4} \sqrt{\alpha^2 - \frac{1}{4}} \quad (\text{A.10})$$

Using (A.4) and (A.5), we can then write

$$P_2 = 4A_o = 8(A_\theta - A_t) \quad (\text{A.11})$$

Substituting (A.9) and (A.10) into (A.11) and performing some further algebraic manipulations, we get:

$$P_2 = 4\alpha^2 \tan^{-1} \left(\sqrt{4\alpha^2 - 1} \right) - \sqrt{4\alpha^2 - 1} \quad (\text{A.12})$$

To calculate P_1 , we refer to Figure A.2, and note that:

$$\frac{P_1}{4} + \frac{P_2}{2} = \frac{\pi\alpha^2}{4} \quad (\text{A.13})$$

Rearranging the above equation, we have:

$$\begin{aligned}
 P_1 &= \pi\alpha^2 - 2P_2 \\
 &= \pi\alpha^2 - 8\alpha^2 \tan^{-1}\left(\sqrt{4\alpha^2 - 1}\right) + 2\sqrt{4\alpha^2 - 1}
 \end{aligned}
 \tag{A.14}$$

By axioms of probability:

$$P_0 = 1 - (P_1 + P_2) \tag{A.15}$$

Substituting (A.12) and (A.14) into (A.15), we get

$$P_0 = 1 - \pi\alpha^2 + 4\alpha^2 \tan^{-1}\left(\sqrt{4\alpha^2 - 1}\right) - \sqrt{4\alpha^2 - 1} \tag{A.16}$$

Interval III: $(\sqrt{2}/2) \leq \alpha \leq 1.0$

This coverage situation is as shown in Figure A.3 below, where we see clearly that for this interval:

$$P_0 = 0 \tag{A.17}$$

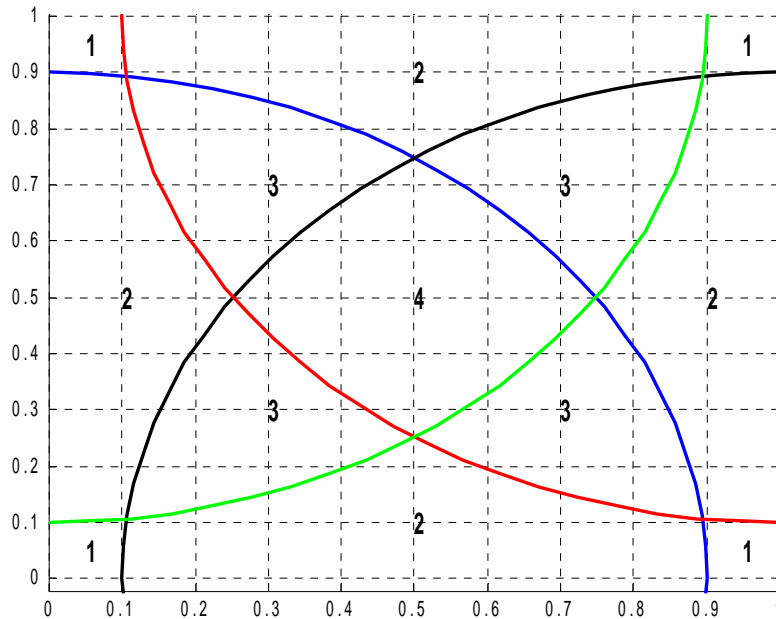


Figure A.3 Coverage scenario pertaining to Interval III

We shall start by deriving the coverage probability P_4 , i.e. the normalized size of the overlap area, labeled ‘4’ in Figure A.3, where the sensor would be able to see all four RPs. The geometry relating to this calculation is shown in Figure A.4, where we will specifically calculate the normalized size of the area A_4 in terms of the triangular areas A_1 and A_2 as well as the area of the circular sector, A_θ , created by angle θ . We can immediately observe that:

$$P_4 = 4A_4 \tag{A.18}$$

$$A_4 = A_\theta - (A_1 + A_2) \tag{A.19}$$

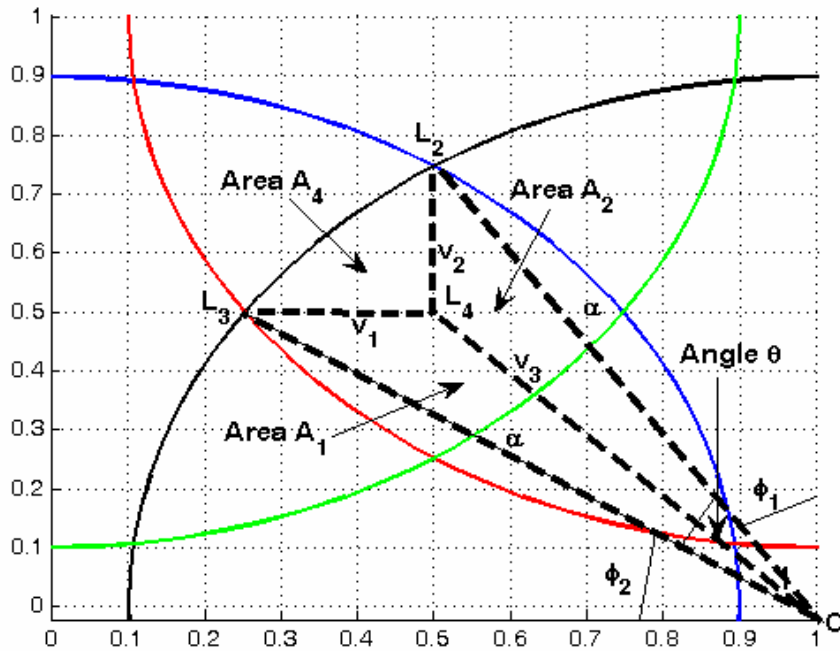


Figure A.4 Illustration of the geometry to calculate P_4

To start, we need to first determine the coordinates of the points L_2 , and L_3 . These are seen to be intersection points for the respective circles each of radius $R = \alpha$. The

location of the x and y coordinates of these points can be derived using the straightforward equations for a circle and can be shown to be as follows. For L_2 :

$$x_2 = \frac{1}{2} \quad (\text{A.20})$$

$$y_2 = \sqrt{\alpha^2 - \frac{1}{4}} \quad (\text{A.21})$$

For L_3 :

$$x_3 = 1 - \sqrt{\alpha^2 - \frac{1}{4}} \quad (\text{A.22})$$

$$y_3 = \frac{1}{2} \quad (\text{A.23})$$

L_4 , by definition, is the midpoint of the area; therefore, its coordinates are:

$$x_4 = y_4 = \frac{1}{2} \quad (\text{A.24})$$

Now we can find the lengths of the sides of the two triangles in Figure A.4.

Specifically,

$$v_1 = x_4 - x_3 = -\frac{1}{2} + \sqrt{\alpha^2 - \frac{1}{4}} \quad (\text{A.25})$$

$$v_2 = y_2 - y_4 = \sqrt{\alpha^2 - \frac{1}{4}} - \frac{1}{2} \quad (\text{A.26})$$

$$v_3 = \sqrt{(1 - x_4)^2 + y_4^2} = \frac{1}{\sqrt{2}} \quad (\text{A.27})$$

We note that $v_1 = v_2$. This means that the two triangles depicted in Figure A.4, are identical and will therefore have the same area, A . This area can be calculated through the use of Heron's formula:

$$A = \sqrt{s_1(s_1 - \alpha)(s_1 - v_2)(s_1 - v_3)} \quad (\text{A.28})$$

where

$$s_1 = \frac{\alpha + v_2 + v_3}{2} \quad (\text{A.29})$$

Substituting (A.26) and (A.27) into (A.29), we have:

$$s_1 = \left(\frac{\alpha}{2} + \frac{1}{2} \sqrt{\alpha^2 - \frac{1}{4}} \right) + \left(\frac{\sqrt{2} - 1}{4} \right) = \beta_1(\alpha) \quad (\text{A.30})$$

Similarly, using (A.30) we can write:

$$s_1 - \alpha = \left(-\frac{\alpha}{2} + \frac{1}{2} \sqrt{\alpha^2 - \frac{1}{4}} \right) + \left(\frac{\sqrt{2} - 1}{4} \right) = \beta_2(\alpha) \quad (\text{A.31})$$

Now, we substitute (A.26) into (A.30) to get:

$$s_1 - v_2 = \left(\frac{\alpha}{2} - \frac{1}{2} \sqrt{\alpha^2 - \frac{1}{4}} \right) + \left(\frac{\sqrt{2} + 1}{4} \right) = \beta_3(\alpha) \quad (\text{A.32})$$

And substituting (A.27) into (A.30) we have:

$$s_1 - v_3 = \left(\frac{\alpha}{2} + \frac{1}{2} \sqrt{\alpha^2 - \frac{1}{4}} \right) - \left(\frac{\sqrt{2} + 1}{4} \right) = \beta_4(\alpha) \quad (\text{A.33})$$

Therefore, in reference to Figure A.4, we can write:

$$A_1 = A_2 = A = \sqrt{\beta_1(\alpha)\beta_2(\alpha)\beta_3(\alpha)\beta_4(\alpha)} \quad (\text{A.34})$$

with $\beta_1(\alpha)$ through $\beta_4(\alpha)$ defined by equations (A.30) through (A.33).

Next, we need to find the area of the circular sector created by the angle θ in Figure A.4. For this, we need to find the angles ϕ_1 and ϕ_2 . From the symmetry of the problem

(i.e. the room is square and all the RPs have the same coverage radius, R), we note that

$\phi_1 = \phi_2 = \phi$. Therefore

$$\theta = \frac{\pi}{2} - 2\phi \quad (\text{A.35})$$

We can find ϕ as:

$$\phi = \tan^{-1}\left(\frac{y_3}{1-x_3}\right) = \tan^{-1}\left(\frac{1}{2\sqrt{\alpha^2 - \frac{1}{4}}}\right) \quad (\text{A.36})$$

Therefore

$$\theta = \frac{\pi}{2} - 2 \tan^{-1}\left(\frac{1}{2\sqrt{\alpha^2 - \frac{1}{4}}}\right) \quad (\text{A.37})$$

Using (A.37), we can now write the expression for area of the sector, A_θ , as:

$$A_\theta = \frac{\alpha^2 \theta}{2} \quad (\text{A.38})$$

Substituting (A.34) and (A.38) into (A.19) and then into (A.18), we obtain:

$$P_4 = 4 \left[\frac{\alpha^2 \theta}{2} - 2\sqrt{\beta_1(\alpha)\beta_2(\alpha)\beta_3(\alpha)\beta_4(\alpha)} \right] \quad (\text{A.39})$$

To derive an expression for P_3 , we refer to the geometry as shown in the diagram below.

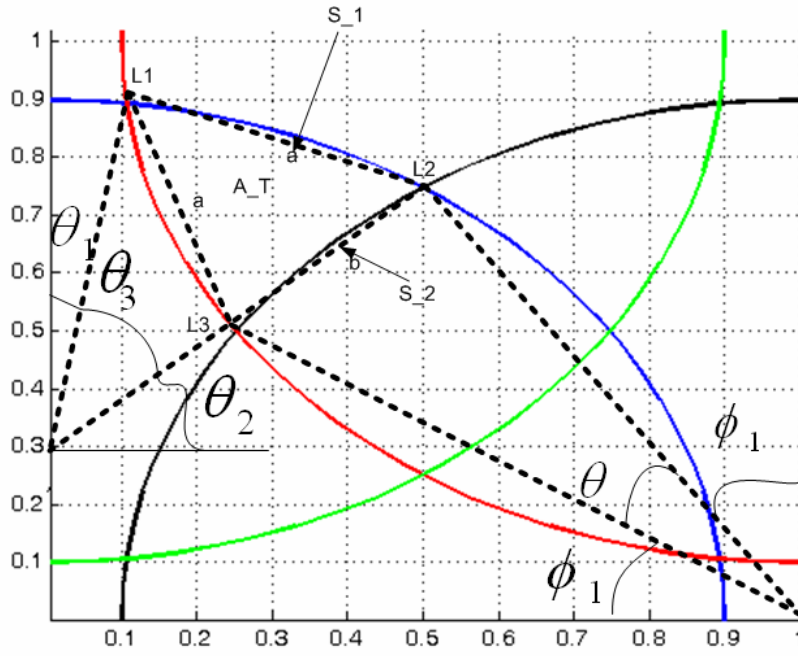


Figure A.5 Illustration of the geometry for the calculation of P_3

In terms of the normalized areas, we note that:

$$P_3 = 4(A_T + 2S_1 - S_2) \quad (\text{A.40})$$

In order to find these areas, we first find the coordinates of the point L_1 using standard geometrical formulas for the intersection of two circles to get:

$$x_1 = \frac{1}{2}(1 - \sqrt{2\alpha^2 - 1}) \quad (\text{A.41})$$

$$y_1 = \sqrt{\frac{\alpha^2}{2} + \frac{1}{2}(2\alpha^2 - 1)^{1/2}} \quad (\text{A.42})$$

Therefore:

$$\theta_1 = \tan^{-1} \left(\frac{1 - \sqrt{2\alpha^2 - 1}}{\sqrt{2\alpha^2 + 2(2\alpha^2 - 1)^{1/2}}} \right) \quad (\text{A.43})$$

Now, we find the coordinates of the points L_2 similarly using the standard formulas for circles and finding the intersection points of them. The results are:

$$x_2 = \frac{1}{2} \quad (\text{A.44})$$

$$y_2 = \sqrt{\alpha^2 - \frac{1}{4}} \quad (\text{A.45})$$

Therefore

$$\theta_2 = \tan^{-1}\left(\frac{y_2}{x_2}\right) = \tan^{-1}\left(2\sqrt{\alpha^2 - \frac{1}{4}}\right) \quad (\text{A.46})$$

Therefore we have

$$\begin{aligned} \theta_3 &= \frac{\pi}{2} - (\theta_1 + \theta_2) \\ &= \frac{\pi}{2} - \left(\tan^{-1}\left(\frac{1 - \sqrt{2\alpha^2 - 1}}{\sqrt{2\alpha^2 + 2(2\alpha^2 - 1)^{1/2}}}\right) + \tan^{-1}\left(2\sqrt{\alpha^2 - \frac{1}{4}}\right) \right) \end{aligned} \quad (\text{A.47})$$

Next, we need to find the angle θ . First note that $\phi_1 = \phi_2 = \phi$ due to the symmetry of the problem. In order to find ϕ , we need to find the coordinates of the point L_3 . These coordinates are:

$$x_3 = 1 - \sqrt{\alpha^2 - \frac{1}{4}} \quad (\text{A.48})$$

$$y_3 = 1/2 \quad (\text{A.49})$$

Therefore, we can write:

$$\phi = \tan^{-1}\left(\frac{y_3}{1 - x_3}\right) = \tan^{-1}\left(\frac{1}{2\sqrt{\alpha^2 - \frac{1}{4}}}\right) \quad (\text{A.50})$$

and

$$\theta = \frac{\pi}{2} - 2\phi = \frac{\pi}{2} - 2 \tan^{-1} \left(\frac{1}{2\sqrt{\alpha^2 - \frac{1}{4}}} \right) \quad (\text{A.51})$$

Next we note that:

$$a = 2\alpha \sin \left(\frac{\theta_3}{2} \right) \quad (\text{A.52})$$

And that

$$\begin{aligned} S_1 &= \left(\text{area of circular sector } \widehat{O_1L_1L_2} \right) - (\text{area of } \triangle O_1L_1L_2) \\ &= \left[\frac{\alpha^2 \theta_3}{2} \right] - \left[\sqrt{s_1(s_1 - \alpha)(s_1 - \alpha)(s_1 - a)} \right] \end{aligned} \quad (\text{A.53})$$

Where

$$s_1 = \frac{2\alpha + a}{2} \quad (\text{A.54})$$

Therefore,

$$S_1 = \left[\frac{\alpha^2 \theta_3}{2} \right] - \frac{a}{2} \sqrt{\alpha^2 - \frac{a^2}{4}} \quad (\text{A.55})$$

In a similar vein, we have:

$$S_2 = \left[\frac{\alpha^2 \theta}{2} \right] - \frac{b}{2} \sqrt{\alpha^2 - \frac{b^2}{4}} \quad (\text{A.56})$$

$$b = 2\alpha \sin \left(\frac{\theta}{2} \right) \quad (\text{A.57})$$

As for the area of the triangle, we have using Heron's formula:

$$\begin{aligned}
A_T &= \text{area of } \triangle L_1 L_2 L_3 \\
&= \sqrt{s_3(s_3 - a)(s_3 - a)(s_3 - b)}
\end{aligned} \tag{A.58}$$

where

$$s_3 = \frac{2a + b}{2} \tag{A.59}$$

Therefore,

$$A_T = \frac{b}{2} \sqrt{a^2 - \frac{b^2}{4}} \tag{A.60}$$

Substituting (A.60), (A.55) and (A.56) into (A.40) we get:

$$\begin{aligned}
P_3 &= 4 \left[\frac{b}{2} \sqrt{a^2 - \frac{b^2}{4}} + 2 \left\{ \left[\frac{\alpha^2 \theta_3}{2} \right] - \frac{a}{2} \sqrt{\alpha^2 - \frac{a^2}{4}} \right\} \right] \\
&\quad - 4 \left[\frac{\alpha^2 \theta}{2} - \frac{a}{2} \sqrt{\alpha^2 - \frac{a^2}{4}} \right]
\end{aligned} \tag{A.61}$$

where θ and θ_3 are defined in (A.51) and (A.47) respectively.

In order to find P_2 and P_1 , we refer to both Figure A.3 above as well as Figure A.6

below to understand the geometry. Specifically we note that:

$$2A = P_4 + \frac{1}{2} P_3 + \frac{1}{4} P_2 \tag{A.62}$$

where A is the overlap area shown in Figure A.6.

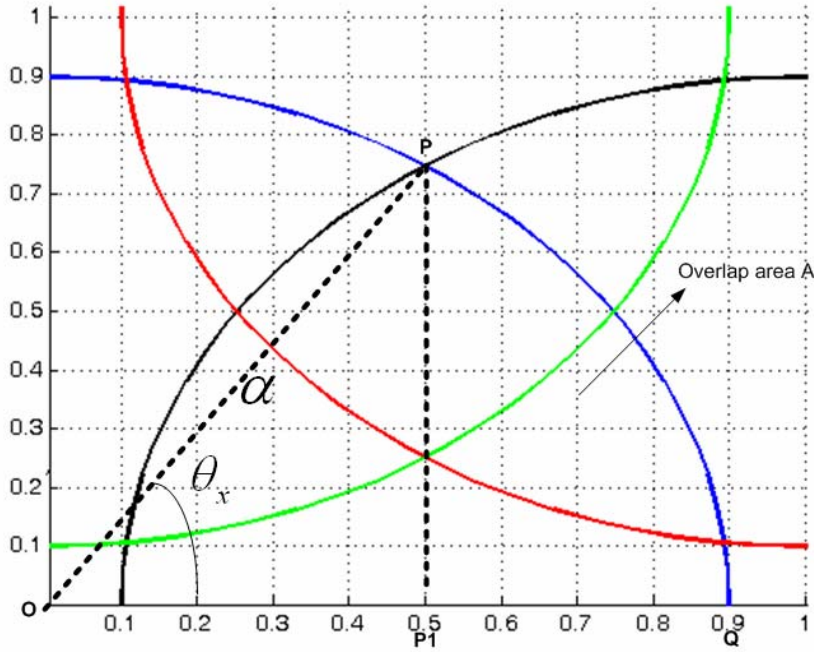


Figure A.6 Illustration of the geometry for the calculation of P2 for interval III

To find the overlap area A, we first find the area covered by the circular sector of angle θ_x :

$$\text{Area of } \widehat{OPQ} = A_s = \frac{\alpha^2 \theta_x}{2} \quad (\text{A.63})$$

Now we find the area of the triangle $\triangle OPP_1$. To do this, we need to know the coordinates of point P. This has been previously determined to be

$$x_p = \frac{1}{2} \quad (\text{A.64})$$

$$y_p = \sqrt{\alpha^2 - \frac{1}{4}} \quad (\text{A.65})$$

Therefore

$$\theta_x = \tan^{-1} \left(\frac{1}{2\sqrt{\alpha^2 - \frac{1}{4}}} \right) \quad (\text{A.66})$$

Therefore, the area of the triangle $\triangle OPP_1$, A_T is

$$A_T = \frac{1}{4} \sqrt{\alpha^2 - \frac{1}{4}} \quad (\text{A.67})$$

So we have

$$A = A_S - A_T = \frac{\alpha^2 \theta_x}{2} - \frac{1}{4} \sqrt{\alpha^2 - \frac{1}{4}} \quad (\text{A.68})$$

Substituting (A.68), (A.66), (A.61) and (A.39) into (A.62) and solving for P_2 , we get:

$$\begin{aligned} P_2 = & 8 \left[\frac{\alpha^2 \theta_x}{2} - \frac{1}{4} \sqrt{\alpha^2 - \frac{1}{4}} \right] \\ & - \left[4b \sqrt{a^2 - \frac{b^2}{4}} + 8\alpha^2 \theta_3 - 8a \sqrt{\alpha^2 - \frac{a^2}{4}} - 4\alpha^2 \theta + 4b \sqrt{\alpha^2 - \frac{b^2}{4}} \right] \\ & - \left[8\alpha^2 \theta - 32 \sqrt{\beta_1(\alpha) \beta_2(\alpha) \beta_3(\alpha) \beta_4(\alpha)} \right] \end{aligned} \quad (\text{A.69})$$

Finally, to obtain P_1 , we use the axioms of probability:

$$P_1 = 1 - (P_2 + P_3 + P_4) \quad (\text{A.70})$$

Substituting (A.69), (A.61) and (A.39) into the above equation yields

$$\begin{aligned} P_1 = & 1 - 8 \left[\frac{\alpha^2 \theta_x}{2} - \frac{1}{4} \sqrt{\alpha^2 - \frac{1}{4}} \right] \\ & + \left[2b \sqrt{a^2 - \frac{b^2}{4}} + 4\alpha^2 \theta_3 - 4a \sqrt{\alpha^2 - \frac{a^2}{4}} - 2\alpha^2 \theta + 2b \sqrt{\alpha^2 - \frac{b^2}{4}} \right] \\ & + 12 \left[\frac{\alpha^2 \theta}{2} - 2 \sqrt{\beta_1(\alpha) \beta_2(\alpha) \beta_3(\alpha) \beta_4(\alpha)} \right] \end{aligned} \quad (\text{A.71})$$

Interval IV: $1.0 \leq \alpha \leq \frac{\sqrt{5}}{2}$

Figure A.7 below depicts the coverage scenario for this interval. For these values of α , we can see that $P_1 = 0$. We also note that the geometrical shape of the area where all four RPs are seen is unchanged, and therefore, the expression for P_4 will be the same as the one presented above for interval III, i.e. equation (A.39). Therefore, we will focus on deriving expressions for P_2 and P_3 .

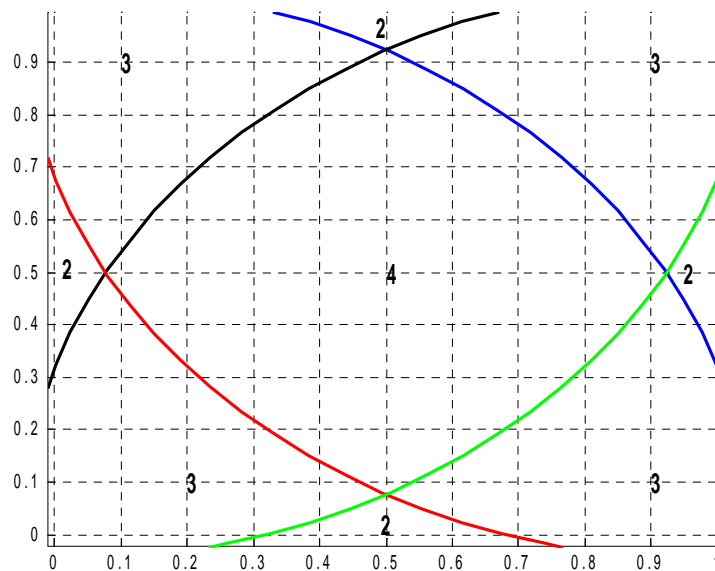


Figure A.7 Illustration of the coverage scenario for interval IV

We start by finding P_2 . Figure A.8 shows the required geometry for this task. We first need to find the x and y coordinates of the points L_1 and L_2 . The coordinates of points L_3 and L_4 are known to be (0,0) and (0.5,1) respectively.

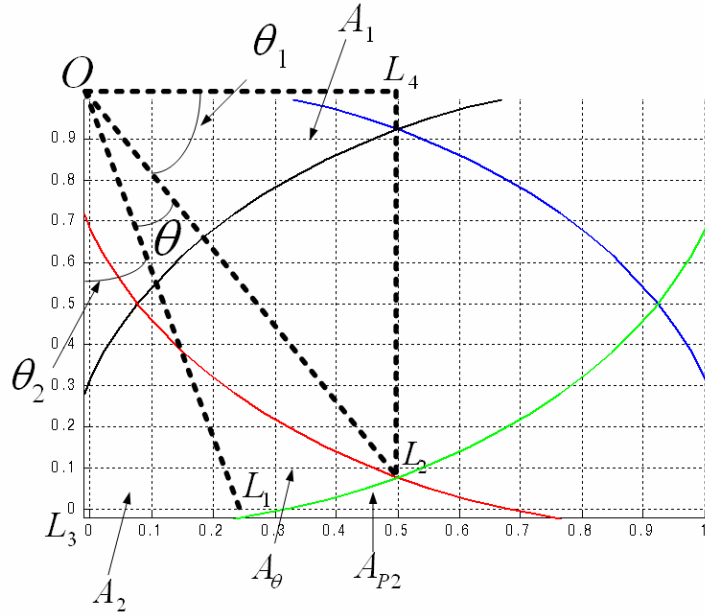


Figure A.8 Illustration of the geometry required for calculating P_2 in interval IV

Through the use of appropriate formulas for circles, we can find the coordinates of L_1 as:

$$x_1 = \sqrt{\alpha^2 - 1} \quad (\text{A.72})$$

$$y_1 = 0 \quad (\text{A.73})$$

Similarly, we can find the coordinates of L_2 as:

$$x_2 = \frac{1}{2} \quad (\text{A.74})$$

$$y_2 = 1 - \sqrt{\alpha^2 - \frac{1}{4}} \quad (\text{A.75})$$

From this, we can write:

$$\theta_1 = \tan^{-1} \left(\frac{y_4 - y_2}{x_4} \right) = \tan^{-1} \left(\sqrt{4\alpha^2 - 1} \right) \quad (\text{A.76})$$

$$\theta_2 = \tan^{-1} \left(\frac{x_1 - x_3}{1} \right) = \tan^{-1} \left(\sqrt{\alpha^2 - 1} \right) \quad (\text{A.77})$$

Therefore, referring to Figure A.8, we can write:

$$\begin{aligned}\theta &= \frac{\pi}{2} - (\theta_1 + \theta_2) \\ &= \frac{\pi}{2} - \left(\tan^{-1}(\sqrt{4\alpha^2 - 1}) + \tan^{-1}(\sqrt{\alpha^2 - 1}) \right)\end{aligned}\tag{A.78}$$

Now, we can write the following for the different area values:

$$A_1 = \frac{1}{2} \left(\frac{1}{2} \right) (y_4 - y_2) = \frac{1}{4} \sqrt{\alpha^2 - \frac{1}{4}}\tag{A.79}$$

$$A_2 = \frac{1}{2} (x_1 - x_3) (1) = \frac{1}{2} \sqrt{\alpha^2 - 1}\tag{A.80}$$

$$A_\theta = \frac{\alpha^2 \theta}{2}\tag{A.81}$$

Since we are dealing with normalized areas for the purposes of these derivations (i.e. $D = 1$ with no loss of generality), it is clear that

$$A_{P_2} = P_2\tag{A.82}$$

Therefore, we can write:

$$\frac{P_2}{2} = \frac{1}{2} - (A_\theta + A_2 + A_1)\tag{A.83}$$

Rearranging the above equation and substituting the results from (A.79), (A.80) and (A.81), we obtain:

$$P_2 = 4 - 4\sqrt{\alpha^2 - 1} - 2\pi\alpha^2 + 4\alpha^2 \tan^{-1}(\sqrt{4\alpha^2 - 1}) + 4\alpha^2 \tan^{-1}(\sqrt{\alpha^2 - 1}) - 2\sqrt{\alpha^2 - \frac{1}{4}}\tag{A.84}$$

To obtain P_3 , we will use the fact that:

$$P_3 = 1 - (P_2 + P_4)\tag{A.85}$$

Substituting the results of (A.84) and (A.39) into (A.85) yields

$$P_3 = 1 - \left[4 - 4\sqrt{\alpha^2 - 1} - 2\pi\alpha^2 + 4\alpha^2 \tan^{-1}(\sqrt{4\alpha^2 - 1}) + 4\alpha^2 \tan^{-1}(\sqrt{\alpha^2 - 1}) - 2\sqrt{\alpha^2 - \frac{1}{4}} \right] - \left[2\alpha^2\theta - 8\sqrt{\beta_1(\alpha)\beta_2(\alpha)\beta_3(\alpha)\beta_4(\alpha)} \right] \quad (\text{A.86})$$

Interval V: $\frac{\sqrt{5}}{2} \leq \alpha \leq \sqrt{2}$

The overall situation for this case is shown in Figure A.9 below. In essence, the overlap between RP coverage areas is such that three or more RPs can be seen at all points throughout the area. Therefore, we see that:

$$P_0 = P_1 = P_2 = 0 \quad (\text{A.87})$$

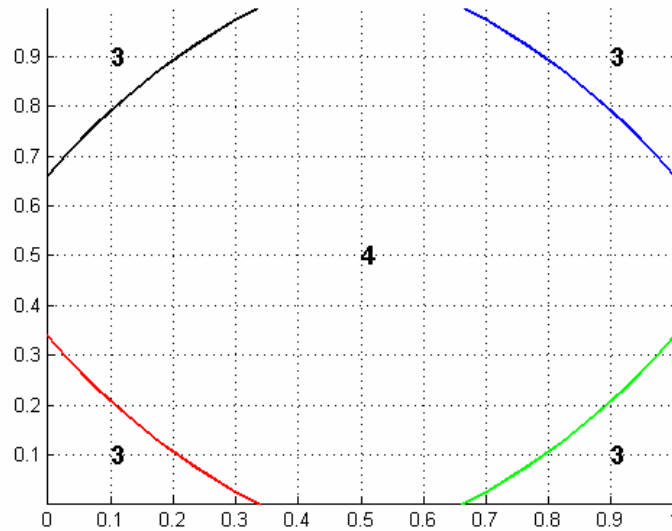


Figure A.9 Illustration of RP coverage areas for Interval V

This being the case we will only need to focus on calculating P_3 and P_4 . In order to do this, we will first depict the geometry and the variables we use in Figure A.10 below.

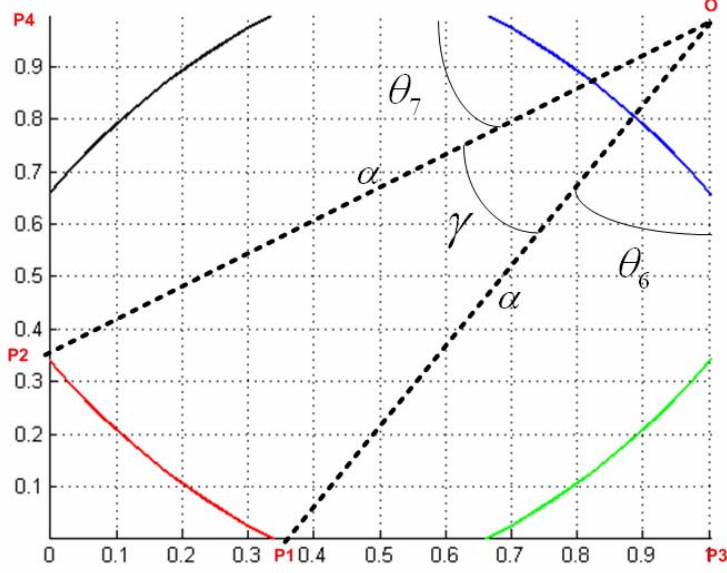


Figure A.10 Illustrating the geometry that will be used in the calculation of the coverage probabilities for interval V.

We first find the x-y coordinates of the point P1. Given that the arc $\widehat{OP_1P_2}$ is from the circle centered at (1,1), the coordinates are found to be:

$$y_1 = 0 \tag{A.88}$$

$$x_1 = 1 - \sqrt{\alpha^2 - 1} \tag{A.89}$$

Therefore

$$\theta_6 = \tan^{-1}\left(\frac{x_3 - x_1}{1}\right) = \tan^{-1}\left(\sqrt{\alpha^2 - 1}\right) \tag{A.90}$$

We also observe that $\theta_6 = \theta_7$ since the area is a square. Therefore, we have

$$\gamma = \frac{\pi}{2} - 2\theta_6 = \frac{\pi}{2} - 2 \tan^{-1}\left(\sqrt{\alpha^2 - 1}\right) \tag{A.91}$$

Now, we find the area of the circular sector bounded by the angle γ as:

$$\text{Area of } \widehat{OP_1P_2} = A_\gamma = \frac{\alpha^2\gamma}{2} \quad (\text{A.92})$$

Since $\theta_6 = \theta_7$, we can write

$$\text{Area of } \triangle OP_1P_3 = \text{Area of } \triangle OP_2P_4 = A_T = \frac{1}{2}\sqrt{\alpha^2 - 1} \quad (\text{A.93})$$

Referring to Figure A.9 and A.10, we can write

$$\frac{P_3}{4} = 1 - (A_\gamma + 2A_T) \quad (\text{A.94})$$

Substituting (A.92) and (A.93) into (A.94) and rearranging, we obtain:

$$P_3 = 4 - 4\sqrt{\alpha^2 - 1} - 2\alpha^2\gamma \quad (\text{A.95})$$

and since $P_4 = 1 - P_3$ in this case, we have

$$P_4 = -3 + 4\sqrt{\alpha^2 - 1} + 2\alpha^2\gamma \quad (\text{A.96})$$

with γ given by (A.91).

Chapter 6 Effects of Node Density on QoE: Full Coverage

In chapter 2, we presented the main concepts of node density and illustrated the relationship between node density, ρ , and the coverage factor, α . In chapter 3, we presented an evaluation of the QoE of LS, RWGH and CN algorithms for indoor geolocation purposes using the RT-based DME model and different node densities. We saw that CN algorithm had a very poor performance compared with the other algorithms, and we proposed a new algorithm, known as CN-TOAG, in chapter 4. We demonstrated that it can outperform LS and RWGH algorithms. We also proposed an extension to CN-TOAG, known as CMS, for the partial coverage scenario. The previous chapter presented a more analytical treatment of the partial coverage case. In this chapter, we present an analysis for the full coverage case, specifically focusing on both the effects of node density on QoE ([Kan06a]) as well as the relationship between the QoE and the Quality of Link (QoL) ([Kan06b], [Kan08a]).

6.1 Full Coverage

In this section, we assume that $\alpha \geq \sqrt{2}$, i.e. R is such that all the RPs can be observed at all points in the area and that $P_4(\alpha) = 1$. In this case, there are two issues to be considered with respect to the QoE:

1. **Bipolar channel behavior:** the indoor radio channel can suddenly switch from the DDP (i.e. pure multipath) state to the UDP state in a probabilistic manner, thereby introducing a lot of errors. This means that the Quality of Link (QoL) can change

dramatically. The statistical behavior of the QoE under such channel conditions needs to be characterized.

2. **Effects of Node Density (ρ):** we need to characterize the effects of node density on the QoE given this bipolar channel behavior.

The two remaining sections below are devoted to a discussion of these issues.

6.2 QoE as a function of Reference Point (RP) Density

We have previously noted in chapter 3 that given a *fixed* number of RPs, the performance of certain positioning algorithms tends to degrade as the size of the area to be covered is increased (i.e the RP density, ρ as defined by (2.3) is decreased) [Kan04a]. This observation makes intuitive sense given that the DME depends on the actual distance (since the DP will be attenuated more as the distance between the RP and the user is increased). This will give rise to more distance measurement error (DME) which, in turn, will lead to degraded location estimation performance.

Although the effects of RP density on QoE has been known, the exact functional relationship between these two quantities has not, to the best of our knowledge, been formulated to date. This raises a valid question: why is it important to characterize this relationship? The answer fundamentally lies in the fact that different indoor positioning applications have different QoE requirements. This implies that the RP densities required for the various application domains would be different. Knowledge of the functional relationship between RP density and QoE enables a system designer to figure out how many RPs are required to meet a given QoE target, thereby resulting in a cost-effective network deployment ([Kan06a]).

The manner in which RP density affects positioning accuracy depends principally on two factors: the particular algorithm used for the location estimation, and the DME model. Our goal now is to explore these kinds of relationships for different geolocation algorithms, both to get an insight into their performance, and also to provide a useful tool for designers of indoor positioning networks. We use the LS and CN-TOAG algorithms for this study. In addition, we leverage the DME model based on UWB measurements [Ala05] in order to account for the existence of UDP conditions.

The relationship between RP density and positioning accuracy has been studied, mainly for ad-hoc sensor networks. Savarese, Rabaey and Beutel have studied positioning in distributed ad-hoc sensor networks through cooperative ranging [Sav01]. The paper by Chintalapudi et al. studied the effects of density of RPs on ad-hoc positioning algorithms employing both distance and bearing measurements [Chi02]. In addition Patwari [Pat05] and Savvides [Sav05] have presented performance bounds as a function of node density, once again for sensor networks.

While these works have identified the relationship between positioning accuracy and RP density, they have not explicitly presented that relationship mathematically. Also, the DME models used in these studies are generally very simple. In the study that follows, we seek to explore the functional dependency of the QoE (as expressed by the *mean square error*, or *MSE*) on RP density in the presence of DME models based on empirical measurements within actual indoor environments.

As in the other performance evaluations, the general system scenario is as shown in Figure 3.2 . The important parameter that determines performance is not the

absolute number of RPs, but the ratio of the number of RPs to the area, as given by the parameter ρ , defined by (2.3).

Here, we consider varying sizes of the room size, D , for each algorithm. By varying the room size while keeping the number of RPs fixed at each of the four corners, we evaluate the performance of positioning algorithms as a function of RP density in the scenario and also show the effect of system bandwidth on overall performance. We vary room size from 20m x 20m to 40m x 40m in two-meter increments in each dimension. Synchronization mismatch between the transmitter and receiver is assumed to be small, i.e. the indoor channel is the dominant source of errors in the distance measurements. For each algorithm, a total of 5000 uniformly distributed random user locations are simulated for different bandwidth values and for varying room dimensions.

Once a user is placed randomly within the area, DME is added to the actual distance measurements from each RP in accordance with the UWB measurement-based DME model [Ala05]. The corrupted distance measurements are then fed into the positioning algorithm to get the position estimate. As noted in [Kan04b], the performance of the CN-TOAG algorithm is dependent on the size of the TOA grid, as determined by the bin size, h , which for the purposes of this study, was fixed at 0.3125 m.

The results are shown in Figure 6.1 and Figure 6.2. From these figures, we can immediately see that as the node density is increased, the MSE decreases. This is an expected result, since a finer installation of the RPs will reduce the probability of the

occurrence of UDP conditions and hence will result in better positioning accuracy. Another key observation is that as the bandwidth of the system is increased, the estimation accuracy is also increased with the exception of 3 GHz. Increasing the system bandwidth provides a better time resolution, thereby ensuring accurate estimation of the TOA of the DP. However, increasing the bandwidth beyond a certain point (2000 MHz in this case) also gives rise to increased probability of UDP conditions; this is because the higher time resolution also means that the powers in the individual paths will be resolved, but that their individual powers will be less than their combined power [Ala05].

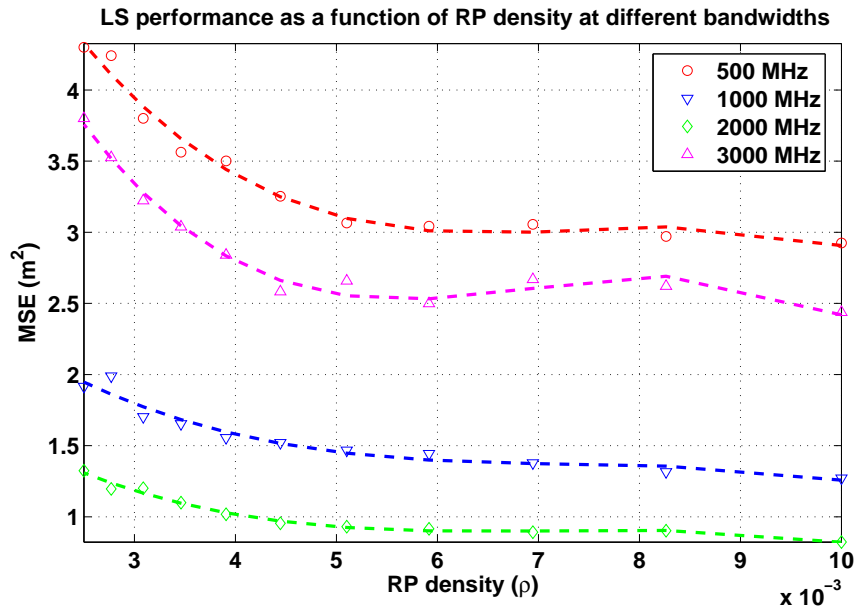


Figure 6.1 LS performance as a function of RP density

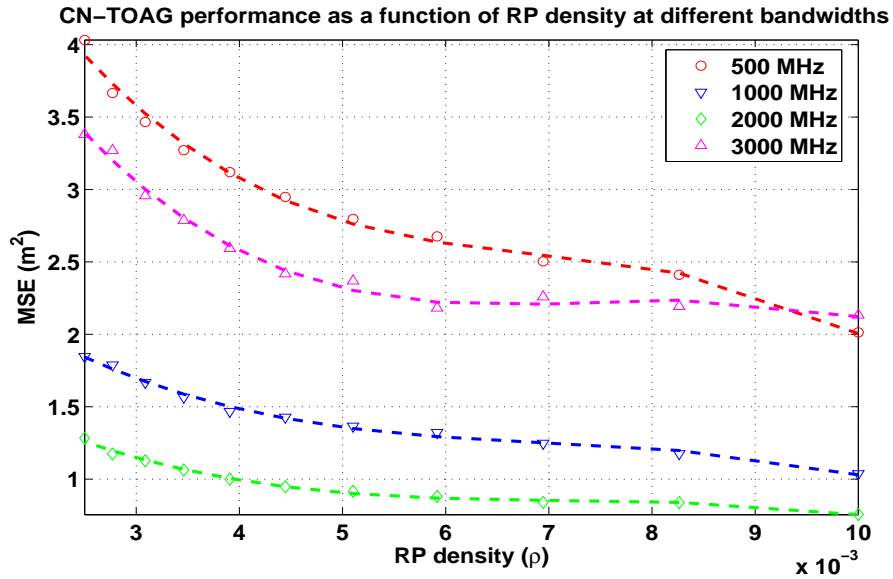


Figure 6.2 CN-TOAG Performance as a function of RP density

In Figure 6.3, we compare the performance of LS and CNTOAG as a function of RP density using a system bandwidth of 2000 MHz. This bandwidth was arbitrarily selected, since it appears to be the bandwidth where both algorithms perform best. The results clearly indicate that CN-TOAG has better performance, particularly for higher values of ρ . Since CN-TOAG is based on the concept of a TOA grid, increasing ρ (i.e. decreasing the area) for a fixed bin size h results in a smaller grid. This, in turn, places a much tighter bound on the positioning error for CN-TOAG. Particularly for values of $\rho \geq 6 \times 10^{-3}$, we can see that CN-TOAG provides an MSE that is about 5.6% lower, although this improvement factor will also depend on the bandwidth used.

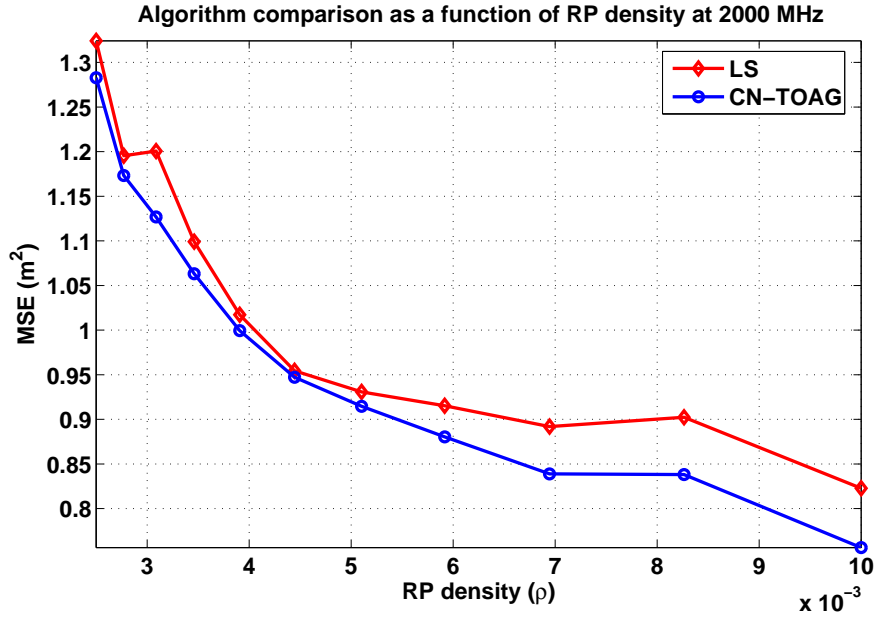


Figure 6.3 Comparison of LS and CN-TOAG as a function of RP density

By examining the results of the simulation, we can derive a mathematical relationship between RP density and MSE by applying a third order polynomial fit to the results. Our choice of the third order polynomial was simply influenced by the fact such a fit showed better agreement with simulation results than, say, a second-order fit. We have chosen to derive these relationships on the basis of Monte-Carlo simulations, rather than analytically, in order to be able to compare and contrast the performance of the LS and CN-TOAG algorithms. It is certainly possible to derive these relationships analytically for the LS algorithm, but not necessarily for CN-TOAG due to the complexity of the objective function. These relationships can be a valuable tool in determining the RP density for a required positioning accuracy. The third order polynomial is given as:

$$MSE(\rho) = a_3\rho^3 + a_2\rho^2 + a_1\rho + a_0 \quad (6.1)$$

where a_i ($i \in \{0,1,2,3\}$) denote the polynomial coefficients. Table 6-1 and Table 6-2 show the coefficient values for the two algorithms. These values are dependent on the DME model used; however, we note that the DME model parameters are still representative of typical indoor environments.

Table 6-1 Coefficients of the third degree polynomial for the LS algorithm

Bandwidth, w (MHz)	a_3	a_2	a_1	a_0
500	-1.20E+07	2.69E+05	-1.98E+03	7.7776
1000	-4.53E+06	1.00E+05	-749.52	3.2647
2000	-4.36E+06	93645	-662.95	2.4484
3000	-1.72E+07	3.60E+05	-2427.4	7.8446

Table 6-2 Coefficients of the third degree polynomial for the CN-TOAG algorithm

Bandwidth, w (MHz)	a_3	a_2	a_1	a_0
500	-1.15E+07	2.42E+05	-1771	7.0203
1000	-4.61E+06	97736	-725.22	3.1171
2000	-3.51E+06	76142	-557.93	2.2317
3000	-1.04E+07	2.34E+05	-1728.7	6.4152

A simple numerical example illustrates how these relationships could be used. Suppose we have a 900 m² indoor area where we would like to implement an infrastructure-based indoor geolocation system using CN-TOAG at a bandwidth of 1 GHz, and we would like the MSE to be no more than 1.5 m². Referring to Figure 6.2,

we see that the corresponding value of ρ should be no less than 0.004. Using our knowledge of the size of the area, the value of ρ needed, and the definition of ρ given in chapter 2, we see that we need to have a minimum of 4 RPs in order to ensure satisfactory performance.

Since CN-TOAG appears to have better performance than LS, we have found it informative to characterize its performance in greater detail. Specifically, we see from Table 6-1 and Table 6-2 that the polynomial coefficients in equation (6.1) are dependent on the bandwidth; therefore, we have done another polynomial fit on these to derive relationships for the polynomial coefficients in terms of bandwidth. These relationships are presented below.

$$\begin{aligned}
 a_3(w) &= 0.0018w^3 - 15w^2 + (3.3 \times 10^4)w - (2.4 \times 10^7) \\
 a_2(w) &= (-3.5 \times 10^{-5})w^3 + 0.3w^2 - (6.8 \times 10^2)w + (5.1 \times 10^5) \\
 a_1(w) &= (2.5 \times 10^{-7})w^3 - 0.0021w^2 + 4.9w - (3.7 \times 10^3) \\
 a_0(w) &= (-8.3 \times 10^{-10})w^3 + (7.5 \times 10^{-6})w^2 - 0.018w + 14
 \end{aligned} \tag{6.2}$$

The usage of these relationships allows us to determine the appropriate coefficients for the third degree polynomial in terms of the operating bandwidth. Thus we are able to determine a unique expression for the performance of the CN-TOAG as a function of the RP density, ρ , for that specific bandwidth.

Another interesting observation from Figure 6.1 and Figure 6.2 is that as the RP density is increased by a factor of four (as we go from the origin to the maximum value on the x-axis), the MSE does not seem to improve by a factor of two, as might be expected, but on average by a factor of 1.54 for the LS algorithm, and about 1.77 for

CN-TOAG. It should be remembered at this point that we have used the DME model based on UWB measurements, which allows us to incorporate the UDP conditions into our evaluation. This fact could help explain our observation in the following way. At a fixed bandwidth, as the RP density is increased, the finer installation of RPs could help reduce the likelihood of UDP conditions, since the occurrence of UDP conditions depends on the actual distance; however, UDP conditions always exist at any distance with a nonzero probability of occurrence. As a result, even if the node density is increased, the occurrence of UDP conditions may introduce additional errors into the distance measurements, and thus prevent the QoE from improving by a factor of two when the RP density is increased by a factor of four. This is an important observation in that the statistical behavior of the channel should also be considered when examining the effects of node density on the QoE for infrastructure-based indoor geolocation. All this now motivates us to more carefully examine the QoE as a function of the statistical behavior of the channel. This is the subject of the following section.

6.3 Statistical behavior of the QoE under Bipolar Channel Behavior: MSE Profile

Due to the site-specific nature of indoor radio propagation, the very occurrence of UDP conditions is random and is best described statistically [Ala05]. That being the case, the QoE (i.e. location estimation accuracy) will also need to be characterized in the same manner. Different location-based applications will have different requirements for QoE. In a military or public-safety application (such as keeping track of the locations of fire-fighters or soldiers inside a building), high QoE is desired. In contrast,

lower QoE might be acceptable for a commercial application (such as inventory control in a warehouse). In such cases, it is essential to be able to answer questions like: “what is the probability of being able to obtain an MSE of 1 m² from an algorithm x over different building environments that give rise to different amounts of UDP?” or “what algorithm should be used to obtain an MSE of 0.1 cm² over different building environments?” Answers to such questions will heavily influence the design, operation and performance of indoor geolocation systems [Kan06b].

Given the variability of the indoor propagation conditions, it is possible that the distance measurements performed by some of the RPs will be subject to DDP errors, while some will be subject to UDP-based errors. The DDP/UDP errors can be observed in various combinations. To illustrate, consider the system scenario shown in Figure 3.2. For example, the distance measurements performed by RP-1 may be subject to UDP-based DME, while the measurements performed by the other RPs may be subject to DDP-based DME; we can denote this combination as *UDDD*. Other combinations can be considered in a similar manner.

Since the occurrence of UDP conditions is random, the performance metric used for the location estimate (such as the MSE) will also vary stochastically and depends on the particular combination observed. For the four-RP case shown in Figure 3.2, it is clear that we will have the following distinct combinations: *UUUU*, *UUUD*, *UUDD*, *UDDD*, and *DDDD*. Each of these combinations can be used to characterize a different Quality of Link (QoL) class. The occurrence of each of these combinations will give rise to a certain MSE value in the location estimate. This MSE value will also depend

on the specific algorithm used. There may be more than one way to obtain each DDP/UDP combination. If UDP conditions occur with probability P_{udp} , then the overall probability of occurrence of the i -th combination, P_i (not to be confused with the coverage probability, which is generally shown as $P_i(\alpha)$), can be generally expressed as:

$$P_i = \binom{N}{N_{udp,i}} P_{udp}^{N_{udp,i}} (1 - P_{udp})^{N - N_{udp,i}} \quad (6.3)$$

where N is the total number of RPs (in this case four), and $N_{udp,i}$ is the number of RPs where UDP-based DME is observed. Combining the probabilities, P_i , with the associated MSE values for each QoL class we can obtain a discrete CDF of the MSE. We call this discrete CDF the *MSE Profile*. We will now illustrate the use of the MSE Profile with examples, focusing on LS and CN-TOAG algorithms.

We consider the system scenario in Figure 3.2 with $D = 20$ m for each algorithm. A total of 1000 uniformly distributed random user locations are simulated for different bandwidth values. In line with the FCC's formal definition of UWB signal bandwidth as being equal to or more than 500 MHz [FCC02], we will present our results for bandwidths of 500, 1000, 2000, and 3000 MHz. For each bandwidth value we also simulate different QoL classes, specifically *UUUU*, *UUUD*, *UUDD*, *UDDD*, *DDDD*. Once a user is randomly placed in the simulation area, each RP calculates TOA-based distances to it. The calculated distances are then corrupted with UDP and DDP-based DMEs in accordance with the DME model based on UWB measurements as given in [Ala05]. The positioning algorithm is then applied to estimate the user location.

Based on 1000 random trials, the MSE is calculated for each bandwidth value and the corresponding combinations of UDP and DDP-based DMEs. The probability of each combination is also calculated in accordance with (6.3).

The results are shown in Figure 6.4 and Figure 6.5. These show the MSE Profiles for the LS and CN-TOAG algorithms respectively. From these plots, we observe that as the bandwidth increases from 500 MHz to 2000 MHz, the range of MSE Profile values gets smaller. This correlates with the findings of [Ala05], where it has been observed that the overall DME goes down over this specific range of bandwidths. Above 2000 MHz, however, the MSE Profile becomes wider as a result of increased probability of UDP conditions, which increases the overall DME. This, in turn, translates into an increase in the position estimation error for both algorithms.

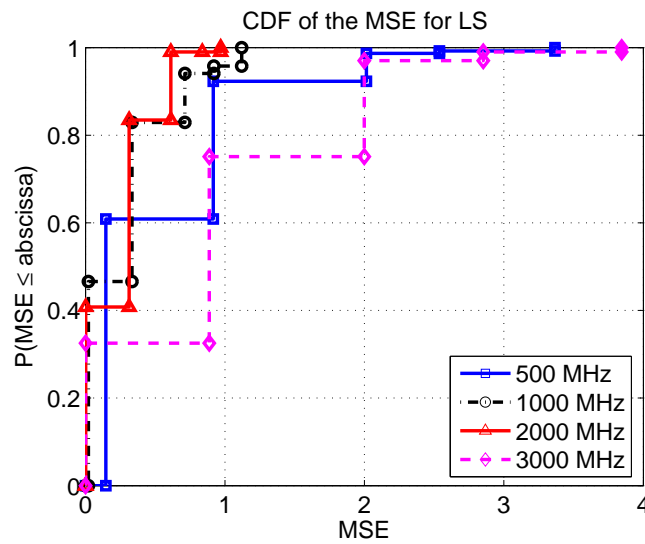


Figure 6.4 MSE Profile for the LS algorithm. The system bandwidth is a parameter

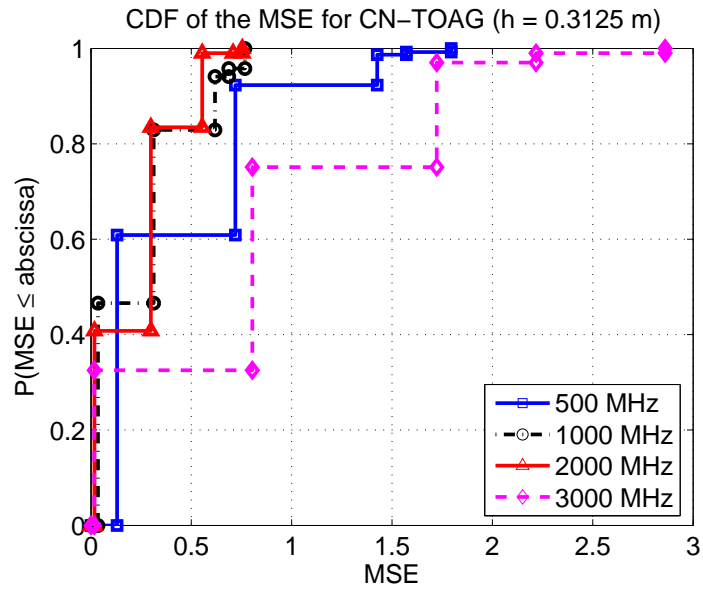


Figure 6.5 MSE Profile for the CN-TOAG algorithm

In order to gain further insight into the variation of the QoE across the different QoL classes, again considering bandwidth as a parameter, we have also plotted just the MSE, as shown in Figure 6.6.

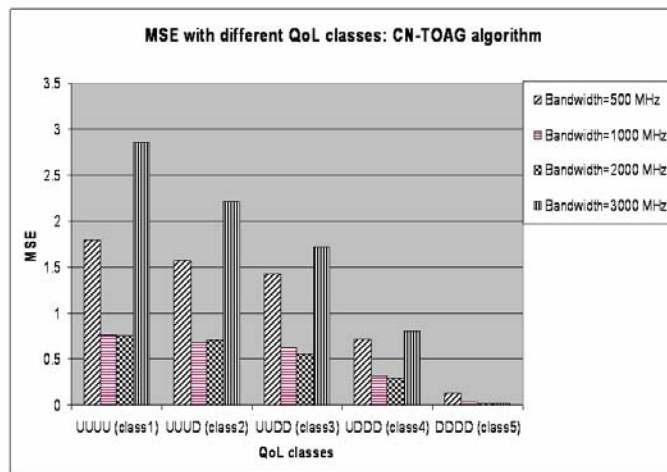


Figure 6.6 QoE variation across different QoL classes

Using the MSE Profile, we can gain insight into the MSE behavior of a given algorithm under varying amounts of UDP (i.e. different QoL classes) by calculating the mean and the variance of the MSE for a given bandwidth value. The results of these calculations are shown as a function of bandwidth in Figure 6.7 and Figure 6.8. These results clearly indicate that CN-TOAG can outperform LS as long as h is about 0.3125 m. In addition, there appears to be an optimal bandwidth for both algorithms where the average MSE is minimized. Our results indicate that this bandwidth value is 1000 MHz.

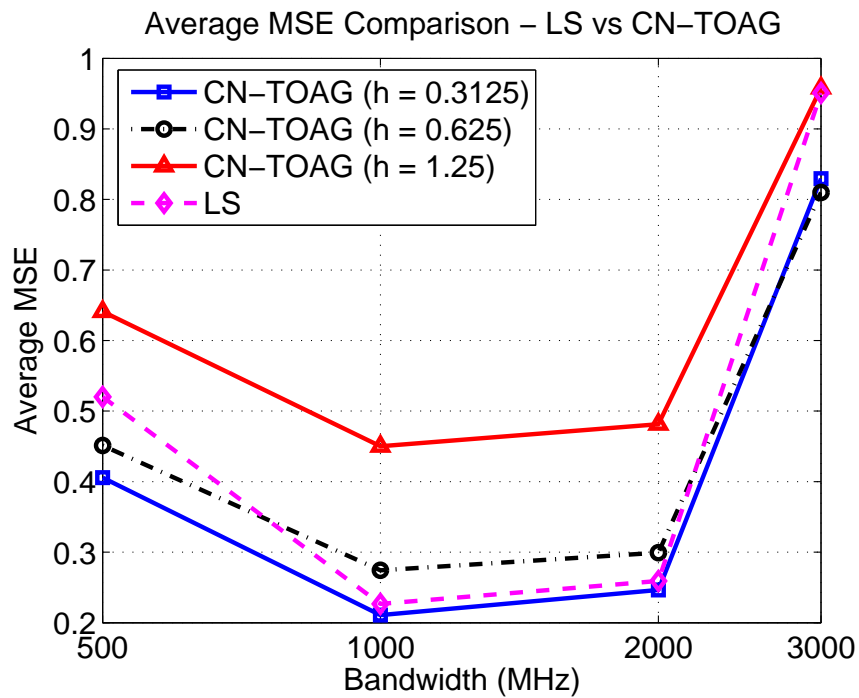


Figure 6.7 Average MSE comparison: LS vs. CN-TOAG

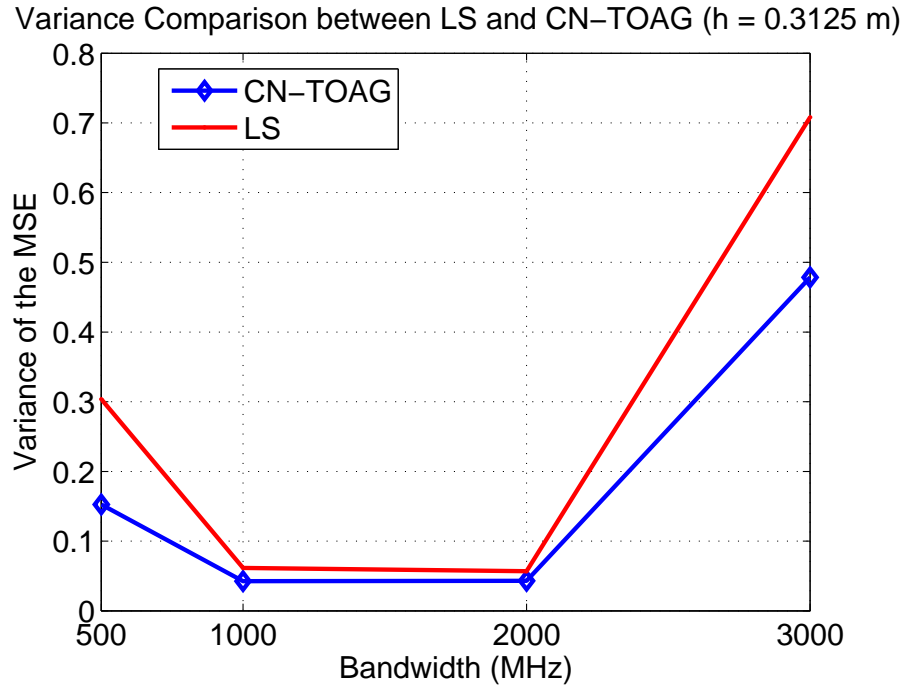


Figure 6.8 Variance comparison: LS vs. CN-TOAG

Based on the results presented above, we find that the QoE behavior exhibited by both algorithms is in line with previously reported observations on DME behavior. Specifically, we see that the QoE increases from 500 MHz to 2000 MHz and then decreases as the bandwidth is increased to 3000 MHz. The reason for this is that at such high bandwidths, the multipath resolution capability of the receiver gets better; however the amplitude of the various paths goes down to the point where they are below the receiver sensitivity threshold. This might lead to the direct path not being detected properly, thereby giving rise to UDP conditions. This physical behavior manifests itself as a reduction in the mean and variance of the UDP-based DME up until 2000 MHz, and then an increase afterward. For the scenario and system bandwidths considered, we can see that CN-TOAG can outperform LS as long as the number of points in the grid

(as determined by the parameter h) is large enough. Specifically, we note that h needs to be about 0.3125 m for the case of a 20m x 20m area in order for CN-TOAG to outperform LS. We also observe that bandwidth of operation of both algorithms needs to be about 1000 MHz in order to guarantee optimal performance across different building configurations.

Chapter 7 Analysis of Performance Bounds

In the previous chapters, we evaluated the performance of existing and new algorithms with different node densities, different types of coverage conditions (full vs. partial) in the presence of models to describe the channel behavior. In this chapter, our goal is to bring these concepts together under a common analytical framework for performance analysis. This framework is provided by the Cramer-Rao Lower Bound (CRLB). The CRLB is derived in the presence of the empirically derived UWB DME model that was briefly discussed in chapter 2. We present the preliminaries in section 7.1, and the bound derivation in section 7.2. In section 7.3, we compare the performance of the CN-TOAG algorithm with the CRLB under various conditions. Following this, we present the CRLB as a function of node density for the full coverage case in section 7.4 and the partial coverage case in section 7.5.

7.1 Cramer-Rao Lower Bound (CRLB): The Preliminaries

The Cramer-Rao Lower Bound (CRLB) is a fundamental bound on the performance of an unbiased estimator [Van68]. It has been well-studied for the geolocation problem by a number of researchers, using the main geolocation metrics (AOA, TOA, RSS) as well as their combinations. It has been used in performance analyses for geolocation in other infrastructure-based wireless networks (such as cellular networks) as well as wireless ad-hoc sensor networks. A general overview of CRLB and its application to the geolocation problem are given by Gustafsson and

Gunnarsson [Gus05] and the references therein. A CRLB analysis for a cellular geolocation system using Received Signal Strength (RSS) as a location metric is presented in [Wei03], and a similar analysis for the TOA and Time Difference of Arrival (TDOA) case is given in [Spi01]. A comparison of the CRLB performance of the RT-TOA technique (a variant of TOA that does not require accurate synchronization between the transmitter and receiver) to the TOA and TDOA techniques is presented in [Mai07]. Other studies relating the CRLB to system parameters for cellular geolocation using TOA and TDOA metrics can be found in [Bot04a] and [Bot04b]. A comparative average performance analysis of TOA and TDOA techniques is presented in [Urr06]. For the case of ad-hoc wireless sensor networks, a CRLB analysis is presented in [Pat03] assuming the use of TOA and RSS as location metrics. A CRLB analysis specifically focusing on *indoor* wireless and ad-hoc sensor networks appears in [Als08]. Another analysis for sensor networks that employ hybrid location estimation schemes such as TOA/RSS and TDOA/RSS is presented in [Cat04].

In the context of TOA-based indoor geolocation, we have a number of TOA measurements from each of the reference points (RPs), which are corrupted by noise as well as additive bias associated with the existence of multipath and UDP conditions. Recall that a TOA measurement, τ , is related to a distance measurement, d , through the relationship $d = c \times \tau$, where c is the speed of light. This observation model for the general case of N RPs covering an indoor area can be expressed as:

$$\hat{\mathbf{\tau}} = \boldsymbol{\tau} + \mathbf{n} \quad (7.1)$$

where $\hat{\mathbf{t}} = (\hat{\tau}_1 \quad \hat{\tau}_2 \quad \cdots \quad \hat{\tau}_N)^T$ is the vector of TOA measurements observed at the output of a matched filter receiver at the respective RPs, and $\mathbf{n} = (n_1 \quad n_2 \quad \cdots \quad n_N)^T$ is a vector of independent zero-mean Gaussian noise samples with variance σ_i^2 ($i=1, \dots, N$), with ([Qi06])

$$\sigma_i^2 = \frac{1}{8\pi^2 \beta^2 R_i} \quad (7.2)$$

where R_i is the signal-to-noise ratio at the receiver and β is the effective bandwidth of the system defined as

$$\beta^2 = \frac{\int_{-\infty}^{+\infty} f^2 |S(f)|^2 df}{\int_{-\infty}^{+\infty} |S(f)|^2 df} \quad (7.3)$$

and $S(f)$ is the Fourier transform of the transmitted pulse used for the TOA estimation. Equation (7.3) can be simplified in certain circumstances [Qi03]. Specifically, we assume that the power spectrum is two-sided and approximately constant over a bandwidth $[-W, W]$, i.e.

$$|S(f)|^2 \cong |S(0)|^2 \quad -W \leq f \leq W \quad (7.4)$$

and that the power spectrum is normalized, i.e.

$$\int_{-\infty}^{+\infty} |S(f)|^2 df = \int_{-\infty}^{+\infty} |s(t)|^2 dt = 1 \quad (7.5)$$

which leads to

$$\beta \cong \frac{W}{\sqrt{3}} \quad (7.6)$$

The TOA measurements, $\boldsymbol{\tau} = (\tau_1 \ \tau_2 \ \dots \ \tau_N)^T$, are subjected to various amounts of bias due to multipath and UDP conditions as expressed by

$$\tau_i = \frac{1}{c}(d_i + \varepsilon_i) = \frac{1}{c} \left(\sqrt{(x - x_i)^2 + (y - y_i)^2} + \varepsilon_i \right) \quad (7.7)$$

where $(x_i, y_i)^T$ represents the coordinates of the i -th RP and ε_i represents the bias value, which is assumed to be statistically independent for different values of i .

7.2 CRLB Derivation for the DME Model based on UWB Measurements

For the case of the empirical UWB measurement-based DME model in section 2.4.2 ([Ala05]), the bias in the distance measurements is given by

$$\varepsilon_i = K_i \cdot G(m_w, \sigma_w) + \zeta_i \cdot G(m_{UDP,w}, \sigma_{UDP,w}) \quad (7.8)$$

with

$$K_i = \log(1 + d_i) \quad (7.9)$$

We can therefore write the joint PDF of the bias values, $\boldsymbol{\varepsilon} = (\varepsilon_1 \ \varepsilon_2 \ \dots \ \varepsilon_N)^T$ as

$$p_{\boldsymbol{\varepsilon}}(\boldsymbol{\varepsilon}) = \prod_{i=1}^N p_{\varepsilon_i}(\varepsilon_i) \quad (7.10)$$

In equation (7.8), the first term represents the additive bias due to DDP and the second term represents the bias due to UDP. In general, one has to estimate the unknown (but nonrandom) coordinates $\mathbf{r} = (x, y)^T$ as well as the set of unknown bias values, $\boldsymbol{\varepsilon} = (\varepsilon_1 \ \varepsilon_2 \ \dots \ \varepsilon_N)^T$. Therefore, the overall parameter vector, denoted by $\boldsymbol{\theta}$ becomes

$$\boldsymbol{\theta} = \begin{pmatrix} \mathbf{r} \\ \boldsymbol{\varepsilon} \end{pmatrix} = (x \ y \ \varepsilon_1 \ \varepsilon_2 \ \dots \ \varepsilon_N)^T \quad (7.11)$$

Note that since the statistics of $\boldsymbol{\varepsilon} = (\varepsilon_1 \ \varepsilon_2 \ \dots \ \varepsilon_N)^T$ are known through (7.10), the overall joint PDF of $\boldsymbol{\theta}$ is also known and is given by

$$p_{\boldsymbol{\theta}}(\boldsymbol{\theta}) = p_{\boldsymbol{\varepsilon}}(\boldsymbol{\varepsilon}) \quad (7.12)$$

In general, the CRLB for an unbiased estimator, $\hat{\boldsymbol{\theta}}$, of a parameter $\boldsymbol{\theta}$ is defined as:

$$E\left\{\left(\hat{\boldsymbol{\theta}} - \boldsymbol{\theta}\right)\left(\hat{\boldsymbol{\theta}} - \boldsymbol{\theta}\right)^T\right\} \geq \mathbf{J}^{-1} \quad (7.13)$$

where \mathbf{J} is the Fisher information matrix (FIM). The FIM can be defined in two ways, depending on whether the a-priori PDF of the parameter vector, $\boldsymbol{\theta}$, $p_{\boldsymbol{\theta}}(\boldsymbol{\theta})$, is known or unknown [Van68]. For the current analysis, the focus will be on the case where $p_{\boldsymbol{\theta}}(\boldsymbol{\theta})$ is known. In this case, the FIM is given by

$$\mathbf{J} = \mathbf{J}_D + \mathbf{J}_P \quad (7.14)$$

where \mathbf{J}_D and \mathbf{J}_P are the components of the Fisher matrix that correspond to the observations, and the a-priori parameter distribution respectively. They are specifically defined as

$$\mathbf{J}_D = E\left[\left(\frac{\partial}{\partial \boldsymbol{\theta}} \ln p(\hat{\boldsymbol{\tau}}|\boldsymbol{\theta})\right)\left(\frac{\partial}{\partial \boldsymbol{\theta}} \ln p(\hat{\boldsymbol{\tau}}|\boldsymbol{\theta})\right)^T\right] \quad (7.15)$$

where $p(\hat{\boldsymbol{\tau}}|\boldsymbol{\theta})$ is the likelihood function of the measurements conditioned on the parameter vector and

$$\mathbf{J}_P = E\left[\left(\frac{\partial}{\partial \boldsymbol{\theta}} \ln p_{\boldsymbol{\theta}}(\boldsymbol{\theta})\right)\left(\frac{\partial}{\partial \boldsymbol{\theta}} \ln p_{\boldsymbol{\theta}}(\boldsymbol{\theta})\right)^T\right] \quad (7.16)$$

As can be inferred from equation (7.8), there will be a certain amount of bias introduced to the TOA measurements regardless of whether the channel profile is DDP or UDP. The reason for this is that in the indoor environment there is generally a very low probability of obtaining a direct LOS path between a transmitter and receiver for geolocation purposes [Pah02]. For this all-NLOS case, it has been shown that ([Qi03])

$$\mathbf{J}_d = \frac{1}{c^2} \begin{bmatrix} \mathbf{H}\mathbf{\Lambda}\mathbf{H}^T & \mathbf{H}\mathbf{\Lambda} \\ \mathbf{\Lambda}\mathbf{H}^T & \mathbf{\Lambda} \end{bmatrix} \quad (7.17)$$

where \mathbf{H} represents the geometric relationship between the actual user location and the RPs and is given by

$$\mathbf{H} = [\mathbf{h}_1 \quad \mathbf{h}_2 \quad \dots \quad \mathbf{h}_N] \quad (7.18)$$

$$\mathbf{h}_i = \begin{bmatrix} \frac{x - x_i}{d_i} \\ \frac{y - y_i}{d_i} \end{bmatrix} \quad (7.19)$$

and $\mathbf{\Lambda}$ represents the noise effects and is given by

$$\mathbf{\Lambda} = \text{diag}(\sigma_1^{-2} \quad \sigma_2^{-2} \quad \dots \quad \sigma_N^{-2}) \quad (7.20)$$

with noise variances σ_i^2 defined in (7.2).

Next, an expression for $p_\varepsilon(\boldsymbol{\varepsilon})$ is derived. First, note that the distribution of ε_i will be

Gaussian in both DDP and UDP cases, with mean and variance given by

$$\mu_{\varepsilon_i} = \begin{cases} \mu_{1i} = \mu_{M,w} K_i & \text{if DDP} \\ \mu_{2i} = \mu_{M,w} K_i + \mu_{U,w} & \text{if UDP} \end{cases} \quad (7.21)$$

$$\sigma_{\varepsilon_i}^2 = \begin{cases} \sigma_{1i}^2 = \sigma_{M,w}^2 K_i^2 & \text{if DDP} \\ \sigma_{2i}^2 = \sigma_{M,w}^2 K_i^2 + \sigma_{U,w}^2 & \text{if UDP} \end{cases} \quad (7.22)$$

An important observation from (7.21) and (7.22) is that both μ_{ε_i} and $\sigma_{\varepsilon_i}^2$ are nonlinear functions of the actual distance, d_i , because of the K_i parameter defined in (7.9). Using (7.21), (7.22), (7.8), and (7.10) we can write

$$p_{\varepsilon}(\boldsymbol{\varepsilon}) = \prod_{i=1}^N \left[\frac{1 - P_{udp}}{\sqrt{2\pi}\sigma_{1i}} \exp\left(-\frac{(\varepsilon_i - \mu_{1i})^2}{2\sigma_{1i}^2}\right) + \frac{P_{udp}}{\sqrt{2\pi}\sigma_{2i}} \exp\left(-\frac{(\varepsilon_i - \mu_{2i})^2}{2\sigma_{2i}^2}\right) \right] \quad (7.23)$$

Because of the structure of $p_{\varepsilon}(\boldsymbol{\varepsilon})$, direct calculation of $\mathbf{J}_{\mathbf{p}}$ is analytically intractable for the case of the DME model given by (7.8). Therefore, an alternative method of calculating $\mathbf{J}_{\mathbf{p}}$, and thus the CRLB is discussed next.

First, we note that for each of the two “states” of the channel (DDP or UDP), ε_i has a Gaussian distribution, albeit with a different mean and variance for each case. For the set of N RPs, different QoL combinations can be observed at a given point. Referring again to the familiar four-RP scenario (reproduced for easy reference in Figure 7.1), we see that at a given point in the area, a total of 16 QoL combinations can be observed, which can be denoted as the set $S_{QoL} = \{DDDD \quad DDDU \quad \dots \quad UUUU\}$. Each of these combinations refers to specific channel conditions that will give rise to various amounts of DME; for example, the combination $DDUD$ refers to the case where we observe DDP-based error on the distance measurements from RPs 1, 2 and 4, but UDP-based error on the distance measurement from RP-3. It is clear that the total number of combinations is $M = 2^N$, where N is the number of RPs.

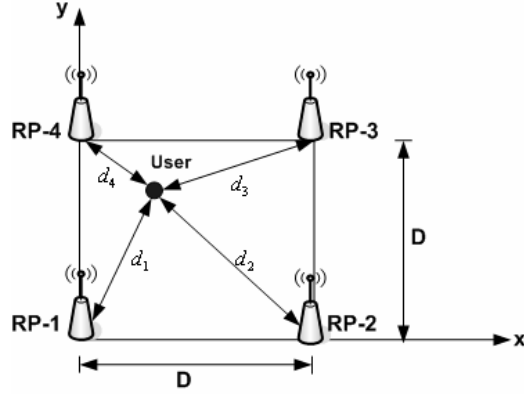


Figure 7.1 Example scenario for infrastructure-based indoor geolocation

Proceeding along these lines, we can see that for every combination in S_{QoL} , $p_{\boldsymbol{\varepsilon}}(\boldsymbol{\varepsilon})$ becomes a product of simple Gaussian PDFs, for which the $\mathbf{J}_{\mathbf{p}}$ matrix can be calculated. As an example, for the combination $DDUU$, we have

$$\begin{aligned}
 p_{\boldsymbol{\varepsilon}}(\boldsymbol{\varepsilon}) &= \prod_{i=1}^N p_{\varepsilon_i}(\varepsilon_i) \\
 &= \prod_{i=1}^N \left[\frac{1}{\sqrt{2\pi}\sigma_i} \exp\left(-\frac{(\varepsilon_i - \mu_i)^2}{2\sigma_i^2}\right) \right]
 \end{aligned} \tag{7.24}$$

where $\mu_i = \mu_{1i}$, $\sigma_i^2 = \sigma_{1i}^2$ for $i=1,2$ and $\mu_i = \mu_{2i}$, $\sigma_i^2 = \sigma_{2i}^2$ for $i=3,4$, where μ_{1i} , μ_{2i} , σ_{1i}^2 , σ_{2i}^2 are as defined in equations (7.21) and (7.22). For the case of independent bias values with Gaussian distribution, it has been shown that $\mathbf{J}_{\mathbf{p}}$ is of the form [Qi06]:

$$\mathbf{J}_{\mathbf{p}} = \begin{bmatrix} \mathbf{0} & \mathbf{0} \\ \mathbf{0} & \boldsymbol{\Omega} \end{bmatrix} \tag{7.25}$$

where

$$\boldsymbol{\Omega} = \text{diag}\left(\frac{1}{\sigma_1^2} \quad \frac{1}{\sigma_2^2} \quad \dots \quad \frac{1}{\sigma_N^2}\right) \tag{7.26}$$

It is clear that each combination in S_{QoL} will change Ω , thereby giving rise to a different \mathbf{J}_p matrix at a given point. This will also be the case for \mathbf{J}_D matrix as well for the following reason. Since UDP conditions typically occur at the edges of the coverage area, or in areas where coverage from a given RP is uncertain, it is also conceivable that the SNR of the received signal under UDP conditions will be a lot lower than in the case of DDP conditions. Since noise variance values on the Λ matrix in equation (7.20) depend on the SNR, it is clear that the different combinations in S_{QoL} will change the Λ matrix, and therefore give rise to a different \mathbf{J}_D matrix at a given point for each combination in S_{QoL} . The net result of all this is that there will be a different value of the CRLB for each QoL combination. Specifically, the value that is of practical interest is the so-called *Root Mean Square Error (RMSE)*, which is simply the square root of the trace of the first 2x2 diagonal sub-matrix within the inverse of the FIM, i.e.

$$RMSE = \sqrt{\text{tr} \left\{ \left[\mathbf{J}^{-1} \right]_{2 \times 2} \right\}} = \sqrt{\sigma_{x,\min}^2 + \sigma_{y,\min}^2} \quad (7.27)$$

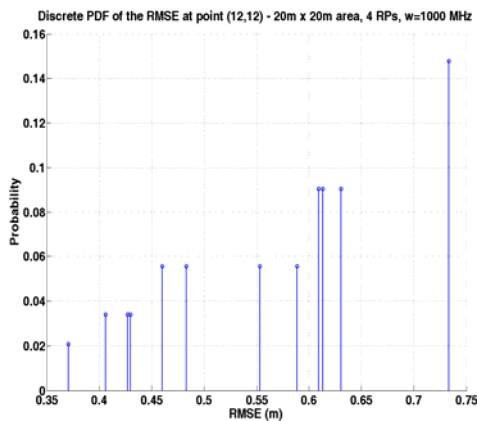
In the second stage of the analysis, the statistics of UDP occurrence are incorporated by using them to calculate the probability of each combination, P_i , in the set S_{QoL} . This is done under the assumption that the links between each RP and the user are statistically independent, i.e. the probability of UDP occurrence on the link between, say, RP i and the user does not alter the probability of UDP occurrence on, for example, the link between RP j and the user. This is a reasonable assumption, since radio transceivers in most indoor wireless networks are typically placed far enough apart to minimize interference. Here, one has to be cognizant of the fact that at a given point,

$P_{udp,w}$ will not necessarily be the same across all RPs. The reason for this is that $P_{udp,w}$ at a given point is dependent on the actual distance as detailed in [Ala05].

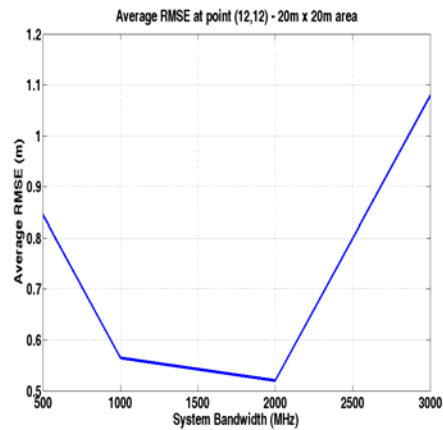
Combining the probabilities, P_i , of each combination together with the CRLB value, denoted by $RMSE_i$, for each combination, it is possible to construct the discrete PDF of the CRLB at a given point. Once this distribution is obtained, it is possible to calculate, for example, the average value of the RMSE at a given point over all the combinations as

$$RMSE_{av} = \sum_{i=1}^M P_i(RMSE_i) \quad (7.28)$$

Intuitively, the average RMSE value calculated in (7.28) will give an idea of what the *average* theoretically optimal estimation performance is likely to be at a given point over all possible QoL combinations. Figure 7.7 shows a sample discrete PDF of the CRLB at a point (12,12) within a 20m x 20m area at a bandwidth of 1000 MHz, as well as the calculated values of $RMSE_{av}$ at that same point as a function of bandwidth. These results clearly indicate the general trends on the estimation errors as a function of bandwidth. We note the increase in $RMSE_{av}$ as the system bandwidth is increased from 2000 to 3000 MHz; this is due to increased likelihood of UDP conditions.



(a)



(b)

Figure 7.2 (a) Discrete PDF of the CRLB at a given point, (b) Average RMSE as a function of bandwidth

Some sample results of the CRLB for different bandwidths and QoL combinations over a 20m x 20m area are shown in Figure 7.3 and Figure 7.4. We can make two observations. First, increasing the bandwidth may reduce the CRLB by a factor that depends on the geometry between the user location and the RP locations. This is not to say, however, that increasing the bandwidth indefinitely will translate to better performance, since the UWB measurements have also revealed that increasing the bandwidth beyond 2000 MHz will result in increased likelihood of UDP conditions, and may actually degrade performance [Ala05] at a given point. This behavior can also be seen from the average RMSE results of Figure 7.2b. Second, having only one measurement with UDP conditions can degrade performance quite noticeably, sometimes by as much as 20% on average across the whole area, depending on geometry. This implies that two factors are absolutely critical for accurate infrastructure-based indoor geolocation:

1. Accurately identifying UDP-based distance measurements,

- Excluding them from the geolocation process or correcting these measurements through preprocessing before use.

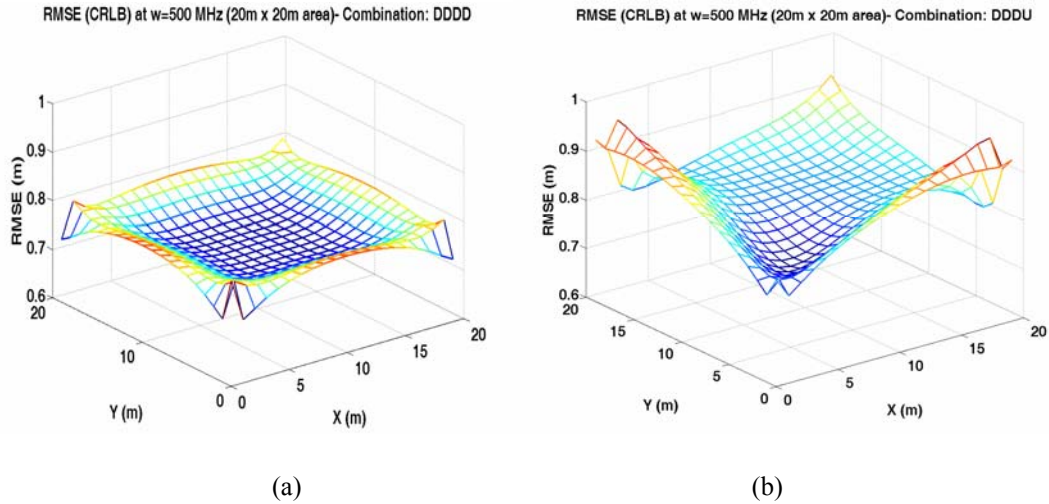


Figure 7.3 CRLB Calculations over a 20m x 20m area with 4 RPs at a bandwidth of 500 MHz: (a) All-DDP (DDDD) case, (b) 3-DDP, one-UDP (DDDU) case

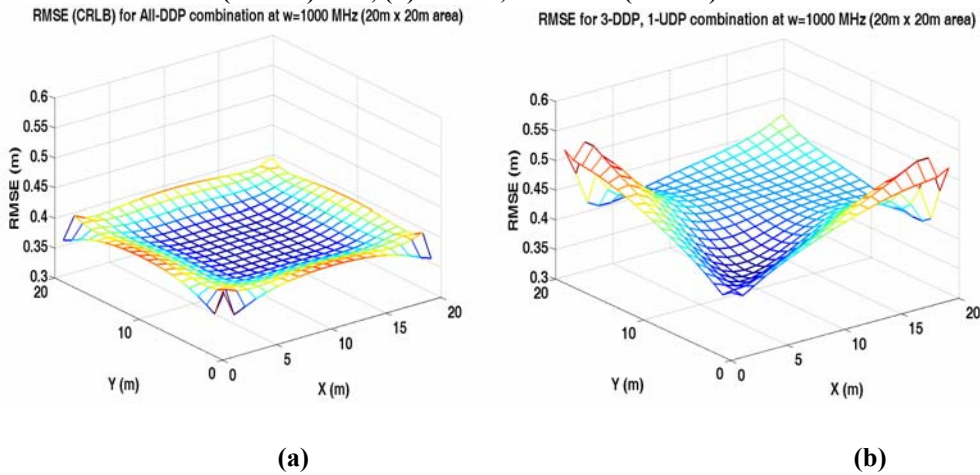


Figure 7.4 CRLB results over a 20m x 20m area with 4 RPs at a bandwidth of 1000 MHz: (a) All-DDP (DDDD) case, (b) 3-DDP, one-UDP (DDDU) case

7.3 Comparison of CN-TOAG Performance with the CRLB

With the above analytical infrastructure in place, it is now possible to undertake a performance comparison of the CN-TOAG algorithm first proposed in chapter 4 with the CRLB. In the existing literature, the traditional method of doing this for the two-dimensional case is via the *concentration ellipse* ([Tor84], [Van68]), also referred to as

the *uncertainty ellipse* by some authors ([Wil05], [Mos03]). Under the assumption that estimation errors are jointly Gaussian, the concentration ellipse basically gives an idea about the spread of estimation errors with respect to the true value of the parameter being estimated. If the estimation errors, $\mathbf{e} = [e_1 \ e_2 \ \dots \ e_N]^T$, are jointly Gaussian, then their joint PDF is given by:

$$p_{\mathbf{e}}(\mathbf{e}) = \frac{1}{(2\pi)^{N/2} |\mathbf{R}_{\mathbf{e}}|^{1/2}} \exp\left(-\frac{1}{2} \mathbf{e}^T \mathbf{R}_{\mathbf{e}}^{-1} \mathbf{e}\right) \quad (7.29)$$

where $\mathbf{R}_{\mathbf{e}}$ is the covariance matrix of \mathbf{e} . The equal-probability contours are then described by ([Van68])

$$\mathbf{e}^T \mathbf{R}_{\mathbf{e}}^{-1} \mathbf{e} = \kappa \quad (7.30)$$

which is actually the equation of an ellipse when $N = 2$, and is known as the *concentration ellipse*. An interesting property of these ellipses is that the probability, $P_{\mathbf{e}}$, that \mathbf{e} lies inside any one of them is only a function of κ , i.e.

$$P_{\mathbf{e}} = 1 - \exp\left(-\frac{\kappa}{2}\right) \quad (7.31)$$

A proof this property can be found in [Van68].

Equation(7.31), then, allows the concentration ellipse to be calculated for any desired probability, $P_{\mathbf{e}}$, by solving for the corresponding value of κ , i.e.

$$\kappa = -2 \ln(1 - P_{\mathbf{e}}) \quad (7.32)$$

These ideas are now used to compare the performance of the CN-TOAG algorithm with the CRLB. The first step is to calculate the eigenvalues of the following 2 x 2 sub-

matrix within the inverse of the FIM that include the minimum error variances in the x and y directions [Tor84]:

$$\mathbf{P}_{CRLB} = \begin{bmatrix} \sigma_{x,\min}^2 & \sigma_{xy,\min} \\ \sigma_{xy,\min} & \sigma_{y,\min}^2 \end{bmatrix} \quad (7.33)$$

and since \mathbf{P}_{CRLB} is a covariance matrix, it is nonnegative-definite and thus will have two real, non-negative eigenvalues ([Str88]), which are denoted by λ_1 and λ_2 . The two eigenvalues are:

$$\lambda_1 = \frac{1}{2} \left[(\sigma_{x,\min}^2 + \sigma_{y,\min}^2) + \sqrt{(\sigma_{x,\min}^2 - \sigma_{y,\min}^2)^2 + 4\sigma_{xy,\min}^2} \right] \quad (7.34)$$

$$\lambda_2 = \frac{1}{2} \left[(\sigma_{x,\min}^2 + \sigma_{y,\min}^2) - \sqrt{(\sigma_{x,\min}^2 - \sigma_{y,\min}^2)^2 + 4\sigma_{xy,\min}^2} \right] \quad (7.35)$$

These eigenvalues help determine the semi-major and semi-minor axis of an ellipse in 2-dimensional space given by $\sqrt{\kappa\lambda_1}$ and $\sqrt{\kappa\lambda_2}$ respectively, with κ being defined as in (7.32) [Tor84]. The same procedure could also be used to derive the concentration ellipse for CN-TOAG, with the slight modification that the covariance matrix, $\mathbf{P}_{CN-TOAG}$, needs to be derived empirically from the results of Monte-Carlo simulations. Since the CN-TOAG estimator is actually a numerical technique for minimizing an objective function (see chapter 4 for details), it is not possible to derive a closed-form analytical expression for its covariance matrix.

With all this said, it is now possible to provide objective answers to the following questions. How does the CN-TOAG performance compare against the

theoretically optimal performance as expressed by the CRLB for different QoL conditions? And how do parameters like bandwidth influence the performance?

To begin to answer these questions, scatter plots are shown Figure 7.5 for the case of 500 and 1000 MHz bandwidth in a 20m x 20m room, and for the case of four RPs, with the RPs deployed in a grid configuration as shown in Figure 7.1. The actual user location is assumed to be (18,18), and the QoL in all links is assumed to DDP. The dots represent CN-TOAG estimates that are obtained from 1000 Monte-Carlo trials and the red ellipse represents the concentration ellipse based on $\mathbf{P}_e = 90\%$, i.e. the region in which 90% of the estimates will lie. The CN-TOAG results are based on a TOA grid of bin size, $h = 0.1$ m.

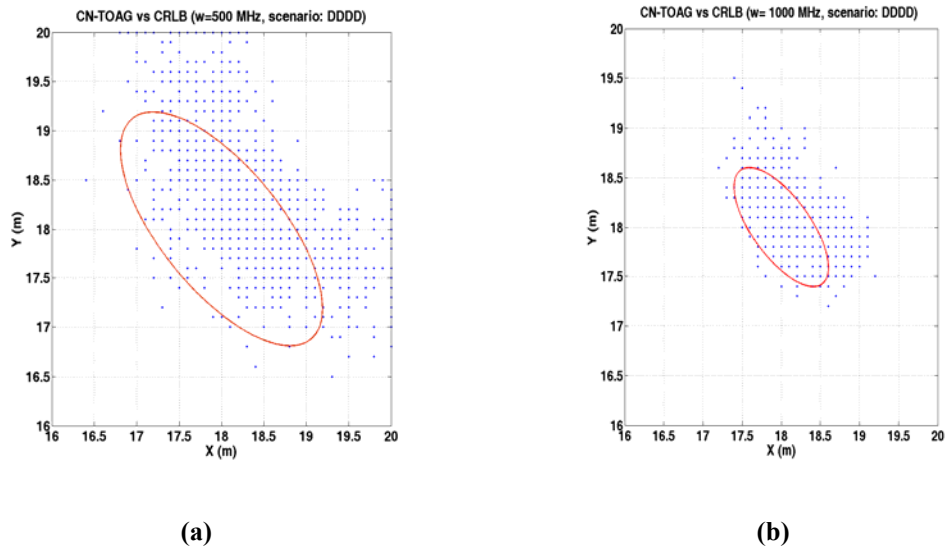


Figure 7.5 Scatter plots of CN-TOAG performance vs. CRLB for the all-DDP case: (a) 500 MHz, (b) 1000 MHz

Our initial observation from these results is that as the bandwidth increases, the CN-TOAG estimates have less spread with respect to the concentration ellipse. This is

due to the fact that all the links are assumed to be DDP in this case, so that the overall DME will decrease as the bandwidth is increased. Another set of results for the case with a single measurement with UDP-based DME is shown in Figure 7.6 below. Here, we clearly see that the size of the bound concentration ellipse because the variance of the DME increases. As a result of this increase in the DME variance, CN-TOAG estimates also show more spread with respect to the concentration ellipse for the same bandwidth.

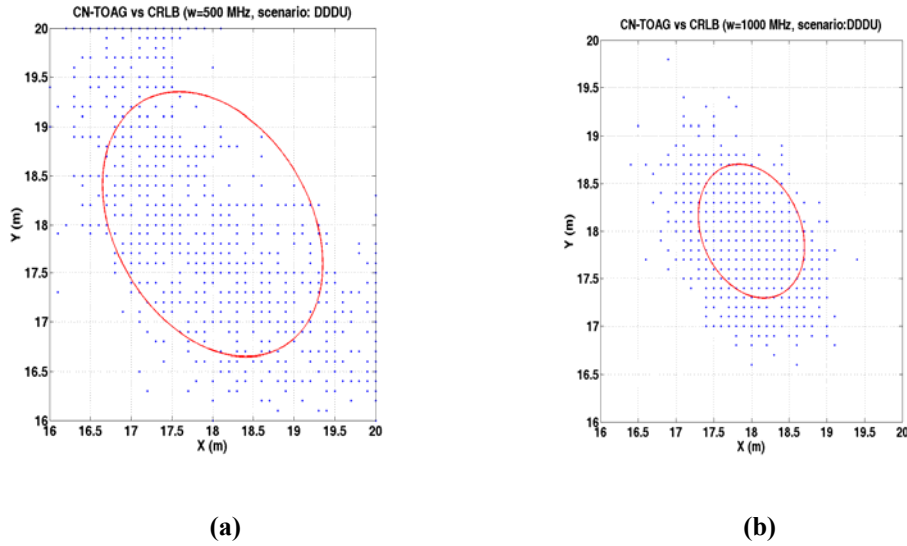


Figure 7.6 Scatter plots of CN-TOAG performance vs. CRLB for the case of UDP-based DME in the measurement set: (a) 500 MHz, (b) 1000 MHz

In order to quantify more precisely how the performance of CN-TOAG compares against the CRLB, 90% concentration ellipses are shown in Figure 7.7(a) for the case of 500 MHz in a 20m x 20m room being covered by four RPs. The user is again assumed to be at (18,18) so the bound calculations are performed on that particular one point. The QoL on all four links is assumed to be DDP and the SNR on the DDP links, R_{dpp} , is arbitrarily assumed to be $R_{dpp} = 10$ dB. The orientation of the

ellipses (i.e. the angle the major axis makes with the x axis) for the algorithm and the bound are slightly different owing to the different amounts of cross-correlation values in the covariance matrices for the two cases. However, it can be clearly seen that the area covered by the 90% concentration ellipse for CN-TOAG exceeds that of the bound ellipse. To see this more clearly, the ellipses are redrawn in Figure 7.7(b) such that the major axis of the bound ellipse and the ellipse for the algorithm are oriented the same way. In this manner, we can see that the area of the concentration ellipse exceeds that of the bound ellipse. This is an example of the general property of the concentration ellipses in that any unbiased estimator of a parameter will produce a concentration ellipse that lies either outside or on the bound ellipse [Van68].

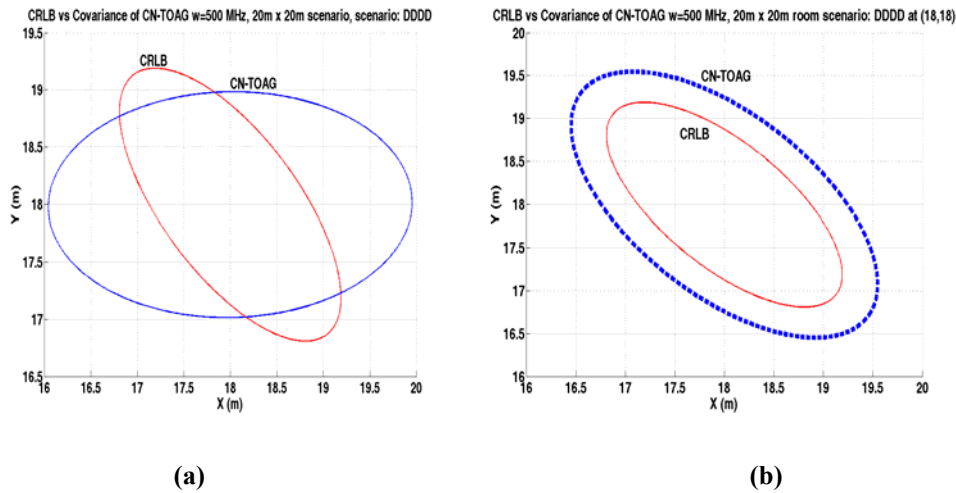
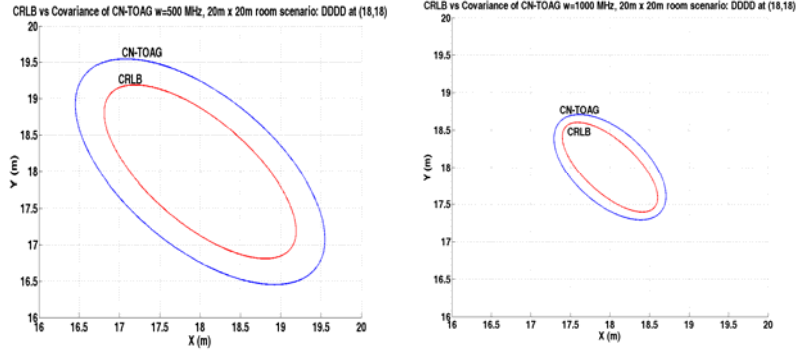


Figure 7.7 Comparison of the 90% concentration ellipses on the CRLB vs. the CN-TOAG algorithm: (a) the ellipses. (b) ellipse for the algorithm reoriented with respect to the bound ellipse.

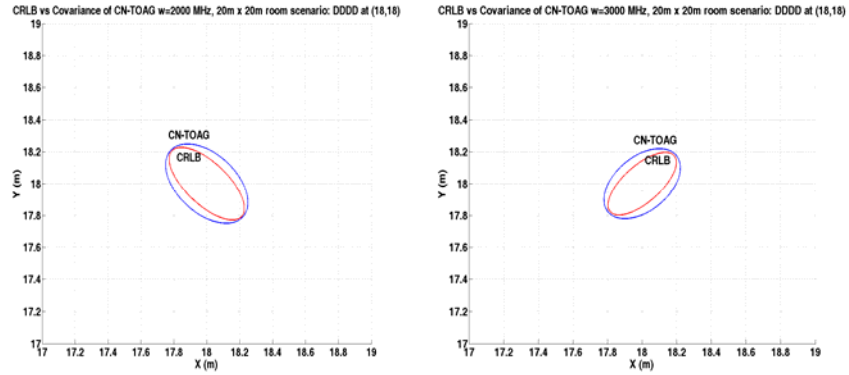
The larger concentration ellipse for the algorithm means that 90% of the estimates obtained are likely to be spread out over a larger area than an efficient

estimate (i.e. an estimate which satisfies the CRLB with equality, also known as a maximum-likelihood estimate), thereby implying larger variance in the estimation error. This is intuitively satisfying, since the goal behind the CRLB analysis is to understand what the theoretically optimum estimation performance is for a given observation model.

In order to explore how the CN-TOAG performance at a given point varies with respect to the CRLB and bandwidth, some further results are shown in Figure 7.8 and Figure 7.9, with the user again assumed to be located at point (18,18) in a 20m x 20m room. The axis of the ellipse for the algorithm is again rotated with respect to the bound ellipse, simply to highlight the fact that the ellipse for the bound is smaller in size than the ellipse for the algorithm. An important observation from the results of Figure 7.8 is that for the all-DDP case, the concentration ellipse for CN-TOAG approaches the bound ellipse as the bandwidth increases. This trend can also be observed in the case of 2000 and 3000 MHz, as can be observed from Figure 7.9. All this implies that for the all-DDP case, CN-TOAG can become an asymptotically efficient estimate as the bandwidth increases, although the degree of efficiency will also depend on the geometric relationship between the user location and the RP locations as well.



(a) (b)
Figure 7.8 Comparison of the CN-TOAG vs. CRLB (all-DDP case) in a 20m x 20m area: (a) $W = 500$ MHz (b) $W = 1000$ MHz



(a) (b)
Figure 7.9 Comparison of the CN-TOAG vs. CRLB (all-DDP case) in a 20m x 20m area: (a) $W = 2000$ MHz (b) $W = 3000$ MHz

In order to get a more objective idea of how well CN-TOAG performs relative to the CRLB, we define the following *measure of relative efficiency*, β_E , as:

$$\beta_E = \frac{A_{CRLB}}{A_{alg}} \quad (7.36)$$

where A_{alg} is the area of the concentration ellipse for the algorithm under consideration (in this case, CN-TOAG) at a given point and A_{CRLB} is the area of the concentration ellipse corresponding to the CRLB at that same point. Obviously, for an efficient estimate (i.e. one that satisfies the CRLB with equality), $\beta_E = 1$, and as the algorithm produces estimates that are less efficient, β_E starts to take on values that are less than

one. On the basis of the results presented in Figure 7.8 and Figure 7.9, the values of β_E have been calculated and are plotted as a function of bandwidth as shown in Figure 7.10 below. On the basis of Figure 7.10, we can make some quantitative observations concerning the effects of bandwidth on relative efficiency. For example, we can see that as the bandwidth is increased from 500 to 1000 MHz, β_E values increase by about 25%, thereby implying that CN-TOAG performance approaches that of the most efficient estimate by about 25% when the bandwidth is doubled. The flat part of the curve in the region between 2000 and 3000 MHz is due to the fact that for these bandwidths, the DDP error takes on very small values [Ala05]. Therefore, increasing the bandwidth beyond 2000 MHz will not necessarily provide a performance advantage for the CN-TOAG algorithm for the all-DDP case.

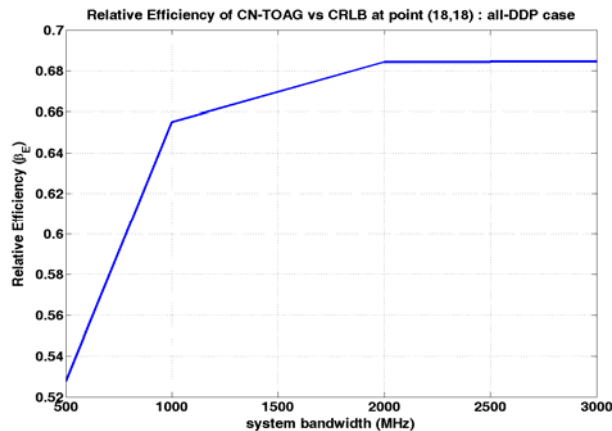


Figure 7.10 Relative efficiency of CN-TOAG as a function of bandwidth (all-DDP case)

Next, the effects of bias due to UDP conditions on CN-TOAG performance and specifically the relative efficiency are examined. As identified in [Ala06a], UDP conditions introduce major errors into the TOA-based distance measurements. In addition, the likelihood of occurrence of UDP conditions increases as the bandwidth

increases. In order to put matters in perspective, the next set of results will focus on the same scenario as before, but this time with only one out of the four RPs subjected to UDP-based DME. Figure 7.11 and Figure 7.12 show the algorithm and bound ellipses for the case of a user located at (18,18) in a 20m x 20m room, at bandwidths of 500, 1000, 2000, and 3000 MHz. For this set of results, the SNR for the DDP links is again assumed to be 10 dB. We also take the SNR for the UDP link as $R_{udp} = -10$ dB ; this is a reasonable assumption, since UDP conditions generally occur in cases where there is signal blockage due to objects and thick walls [Ala06b].

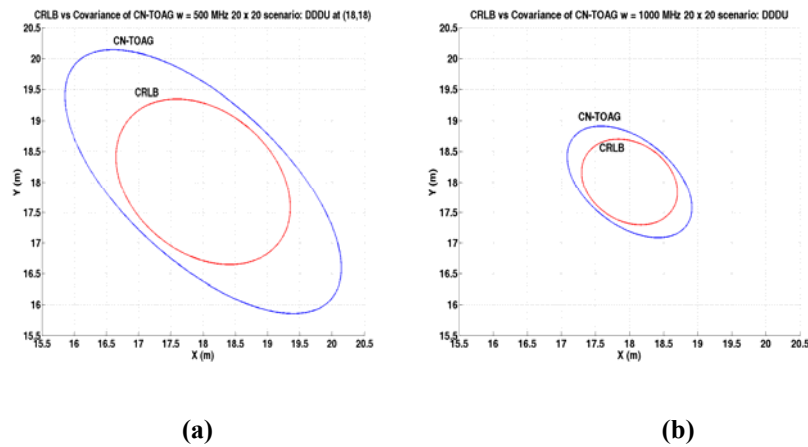


Figure 7.11 Comparison of CN-TOAG vs. CRLB for the 3-DDP, 1-UDP case in a 20m x 20m area: (a) w=500 MHz, (b) w=1000 MHz

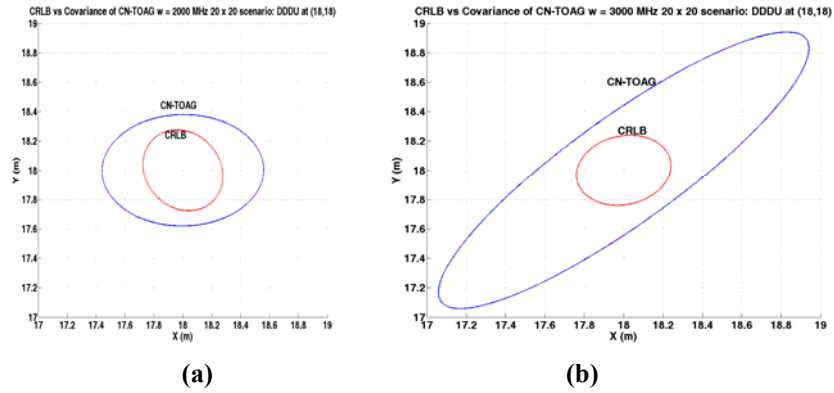


Figure 7.12 Comparison of CN-TOAG vs. CRLB for the 3-DDP, 1-UDP case in a 20m x 20m area: (a) $w=2000$ MHz, (b) $w=3000$ MHz

Similar to the analysis for the all-DDP case, we now calculate and plot the values of β_E as a function of bandwidth, as shown in Figure 7.13. An important finding from these results is that CN-TOAG does not become more efficient as the bandwidth is increased if there are distance measurements in the set that are corrupted by UDP-based error. This is due to the fact that variance of the UDP-based DME actually increases as the bandwidth is increased, especially for bandwidth values greater than 1000 MHz [Ala05].

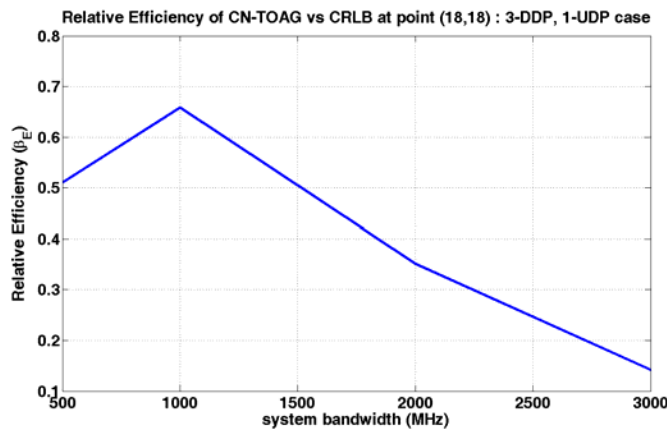


Figure 7.13 Relative efficiency of CN-TOAG vs. CRLB (3-DDP, 1-UDP case)

7.4 Effects of Node Density on the CRLB: Full Coverage Case

It is a well-known fact that geolocation performance is impacted by the number of distance measurements available. This is especially critical in the indoor environment, where the probability of obtaining a direct line of sight (DLOS) path to an RP is much lower than in the outdoor case, depending on the particulars of the building material, furniture, people and so on. In such a NLOS environment, it has already been shown that having more distance measurements will provide higher geolocation accuracy for a given standard deviation of DME [Qi03]. Therefore, it is critical to study the effects of node density, and more specifically *RP Density* on the performance of infrastructure-based indoor geolocation systems.

As given in [Kan06a], RP density, ρ , is defined as the number of RPs (N) per unit area (A):

$$\rho = \frac{N}{A} \quad (7.37)$$

The focus will now be on calculating the CRLB as a function of ρ . The definition of ρ implies that it is necessary to come up with one value of the CRLB that would characterize an entire indoor area for a given value of ρ . Since the value of the CRLB at a given point is also dependent on the geometric relationship between the RPs and the user, one needs to “average out” the effects of geometry. The way this is done is as follows. First a large number, L , of random user locations are simulated through Monte-Carlo methods. The user locations are uniformly distributed over the indoor area. At each of these points, the CRLB for each possible QoL combination is calculated.

Focusing on the first diagonal 2x2 CRLB sub-matrix, an average of the variances in the x and y direction *at each point* is calculated as

$$\sigma_{x,av,k}^2 = \sum_{j=1}^M P_j \sigma_{x,jk}^2 \quad (7.38)$$

$$\sigma_{y,av,k}^2 = \sum_{j=1}^M P_j \sigma_{y,jk}^2 \quad (7.39)$$

where $\sigma_{x,jk}^2$ and $\sigma_{y,jk}^2$ are the computed variances in the x and y directions for the j -th combination at the k -th point ($k=1,..L$) respectively and M is the number of QoL combinations. Finally, in a similar fashion to [Sav05], an average root mean square error (RMSE) value for the whole area (averaged over the geometry and the particular QoL combinations) is calculated as:

$$RMSE_{area} = \frac{1}{L} \sqrt{\sum_{k=1}^L (\sigma_{x,av,k}^2 + \sigma_{y,av,k}^2)} \quad (7.40)$$

The results of this calculation are as shown in Figure 7.14. Based on these results, two important observations can be made. First, regardless of the bandwidth, increasing the RP density beyond a certain point will not necessarily translate to better performance. A similar observation was made within the context of ad-hoc sensor networks in [Sav05]. The second observation is that increasing the bandwidth beyond a certain value (2000 MHz in this case) actually results in a worsening of performance (as indicated by the increase in CRLB values). We also note that these results are somewhat counterintuitive, considering some of the previously published results in [Gez05], which indicated that the CRLB values decrease with increasing system bandwidth. The main reason for this discrepancy is channel behavior, specifically the increased likelihood of UDP conditions at the higher bandwidths, which are not accounted for in [Gez05]. This

result highlights why the relationship between the node density and QoE is not a simple one, as the physical behavior of the channel (particularly as related to the effect of bandwidth) also has a part to play in the determination of the QoE, and therefore needs to be considered.

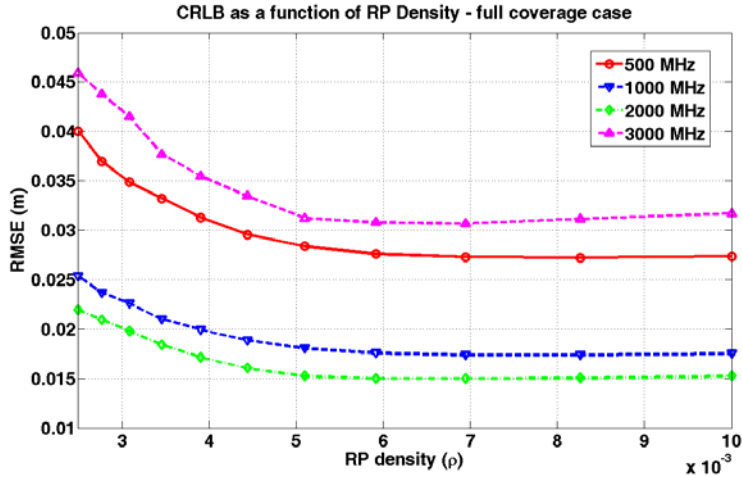


Figure 7.14 CRLB as a function of the RP density: full coverage case

7.5 Effects of Node Density on the CRLB: Partial Coverage Case

As previously stated in chapter 5, fading in the indoor radio channel will sometimes cause radio coverage issues. As a result, it may not be possible for a user to contact some or all of the RPs at a given point. From a geolocation perspective, this means that the number of RPs that can contact the user and perform distance measurements will not always stay the same at a given point. This, in turn, implies that geolocation accuracy at a given point is also a function of the probability, P_K , of being able to obtain distance measurements from a certain number, K , of RPs where $K \leq N$. In a TOA-based geolocation scenario, the minimum value of K needs to be three in order

to locate the user uniquely. The objective now is to gain some basic intuition as to how this probability would affect the CRLB. This will be done in terms of the coverage probabilities, $P_K(\alpha)$, that were first discussed in section 5.2.

Since three distance measurements from three RPs are needed in order to locate a user uniquely, we focus on those values of α that will result in three RPs or more being observed at a given indoor area. As can be seen from Figure 5.2, the appropriate

intervals of α are $\frac{\sqrt{5}}{2} \leq \alpha \leq \sqrt{2}$ (interval V in section 5.2) and $\alpha \geq \sqrt{2}$ (interval VI in

section 5.2), since $P_0 = P_1 = P_2 = 0$. We can therefore show that for $\frac{\sqrt{5}}{2} \leq \alpha \leq \sqrt{2}$ (see

Appendix 5.A at the end of chapter 5 for details):

$$P_3(\alpha) = 4 - 4\sqrt{\alpha^2 - 1} - 2\alpha^2\gamma \quad (7.41)$$

$$P_4(\alpha) = -3 + 4\sqrt{\alpha^2 - 1} + 2\alpha^2\gamma \quad (7.42)$$

where

$$\gamma = \frac{\pi}{2} - 2 \tan^{-1}(\sqrt{\alpha^2 - 1}) \quad (7.43)$$

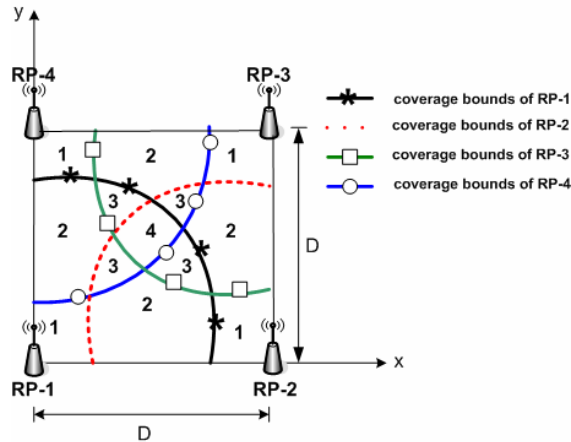


Figure 7.15 Illustrating the coverage issues for indoor geolocation

The relationship between α and the CRLB is evaluated in the following manner. Similar to the methodology of the previous section, a number of random user locations is simulated to “average out” the effects of geometry on the bound values. Then the $RMSE_{area}$ for the whole area is calculated, in the same manner as the previous section, for the case of three and four RPs. Then an average RMSE is calculated for the whole area as a function of α using the relation:

$$RMSE(\alpha) = RMSE_{3,w}P_3(\alpha) + RMSE_{4,w}P_4(\alpha) \quad (7.44)$$

where $RMSE_{3,w}$ and $RMSE_{4,w}$ represent RMSE values over the whole area corresponding to three and four RPs respectively, with the subscript w denoting bandwidth dependence, since the RMSE depends on the DME, which in turn depends on the system bandwidth.

The results of this calculation are as shown in Figure 7.16. An important trend that can be observed from this plot is that for a given value of α , the value of the CRLB goes down until about 2000 MHz and then comes back up at 3000 MHz, indicating a worsening of performance. This is consistent with the observations of [Ala06a], where it is noted that increasing the bandwidth beyond 2000 MHz results in an increased likelihood of UDP conditions. The CRLB results clearly indicate that the amount of UDP-based DME is so much that even introducing additional RPs and distance measurements (by increasing the value of α) does not help remedy the situation, since the CRLB results remain above those for the 500 MHz value.

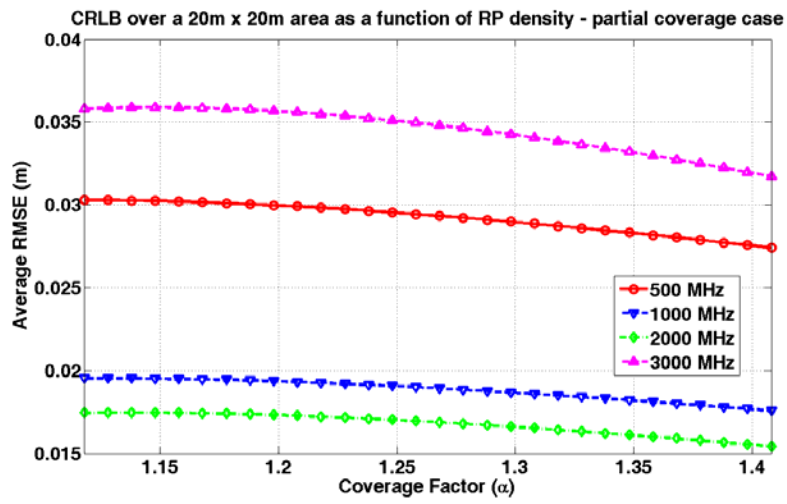


Figure 7.16 CRLB as a function of RP density: partial coverage case

Chapter 8 Conclusions & Future Work

In this chapter, we summarize the main findings of this dissertation and outline some directions for future work. The findings of the dissertation are summarized in section 8.1 and directions for future work are given in section 8.2.

8.1 Conclusions

In this dissertation, we investigated the effects of node density on the quality of estimation for infrastructure-based indoor geolocation using TOA. Specifically, we have developed a framework for evaluation of the performance of infrastructure-based indoor geolocation using different algorithms, different node densities and fundamental bounds on performance. We have done this in the presence of distance measurement error (DME) models recently proposed in the literature [Ala06a], and which are based on ray-tracing (RT) as well as empirical measurements in the UWB regime. The main objective of the research effort was to explore the interrelationship between node density, algorithms, channel behavior, and quality of estimation (QoE) statistics.

We began this investigation by defining the system scenario and the node density and coverage factor in chapter 2. In chapter 3, we examined the QoE for existing geolocation algorithms (LS, RWGH and CN) in the presence of the RT-based DME model. Our main findings were as follows. Regardless of the bandwidth used, the CN algorithm exhibited estimation errors that were 2.5-8 times higher than LS or RWGH algorithms, depending on the system bandwidth. This was due to the crude

manner in which the CN algorithm obtained the location estimate. We also observed that regardless of the bandwidth, channel scenario or the algorithm under consideration, the QoE was degraded by an approximate factor of two when the node density was decreased by a factor of four.

Based on these results, we proposed a new geolocation algorithm based on pattern-recognition principles, known as CN-TOAG in chapter 4. This algorithm, unlike many pattern-recognition algorithms did not require extensive measurement databases or other types of training. We also proposed an extension to this algorithm to cover the partial coverage scenario, known as CMS. We evaluated its performance in the presence of the RT-based DME model. We found that CN-TOAG performance is determined by the spacing between the TOA grid points. Closer spacing of the grid points will put a tighter bound on the positioning error. We found, however, that decreasing the spacing between the grid points (i.e. increasing the size of the grid) beyond a certain value did not necessarily enhance the QoE. For the system scenarios we considered, this value was about 1.25 m. We also observed that CN-TOAG can outperform the LS and RWGH algorithms. While the exact amount of performance difference will differ depending on the bandwidth used, we saw that CN-TOAG can outperform LS and RWGH by as much as 38% and 12% respectively. For the partial coverage case, we found that the CMS algorithm had the best performance when the radius of coverage was roughly of the order of the size of the area, i.e. when the coverage factor $\alpha \approx 1$.

Next, we presented an in-depth analysis of the partial coverage effects in chapter 5. We then did a more in-depth analysis of the effects of node density on QoE in chapter 6 for the full coverage case. We came up with explicit mathematical relationships to quantify the QoE as a function of different node densities in the presence of the DME model based on UWB measurements. We also characterized the statistical variation of the QoE as a function of quality of link (QoL) conditions with this same DME model. We found that CN-TOAG can have a higher QoE than the LS algorithm for a given node density depending on the size of the TOA grid. Specifically, we observed that depending on the system bandwidth used, CN-TOAG provides an MSE that is roughly 5.6% lower for values of $\rho \geq 6 \times 10^{-3}$.

Finally, in chapter 7, we presented an analysis of the fundamental bounds associated with QoE. We did this within the framework of the CRLB. We presented derivations of the CRLB considering the DME model based on UWB measurements. We then used our results to gauge the performance of the CN-TOAG algorithm. We also presented results on the variation of the CRLB as a function of node density. We observed that, depending on the geometric relationship between the reference points (RPs) and a given user location, the CRLB could increase by almost 20% across an entire area because of a single occurrence of UDP conditions in the measurement set. This finding indicates that even a single occurrence of a distance measurement with UDP-based error can cause major performance degradation. It also allows us to conclude that indoor geolocation algorithms must have the capability to (1) detect the existence of UDP conditions in the measurement set, and (2) to either correct them or

exclude them from the location estimation process. For the case where no UDP conditions are present, we saw that CN-TOAG can become a relatively more efficient estimator as the bandwidth is increased, although the degree of relative efficiency will also depend on the geometric relationship between the user location and the RP locations. However, CN-TOAG can fail to be relatively more efficient with increasing bandwidth if UDP conditions are present, due to the significant amount of additional error introduced by UDP conditions. Regardless of the bandwidth, we observed that increasing the node density, ρ , beyond a certain point did not result in lower values of the CRLB. For the system scenarios we considered, this value of ρ was found to be approximately 6×10^{-3} . This implies that there is a fundamental limit to the performance improvement that can be obtained by merely increasing the RP density.

8.2 Future Work

There are several directions in which this work could be extended. We outline some suggestions below:

- Performance analysis of the CMS algorithm in chapter 4 could be further enhanced by looking at the estimation error for each value of α and breaking it down to see how much of the error is attributable to distance measurements from a single RP, two RPs and so on.
- The complexity of the CN-TOAG algorithm could be reduced if the search for the minimum on the TOA grid can be done more intelligently. This could, for example,

be done by also using RSS information to narrow down the set of possible locations to a smaller area on the grid before launching the CN-TOAG algorithm.

- The general formulation of the likelihood function for the DME model based on UWB measurements will have a bimodal distribution composed of two Gaussian distributions. Estimating the parameters of this distribution, possibly through a technique such as expectation-maximization (EM), could result in new classes of algorithms for infrastructure-based indoor geolocation.
- The CRLB analysis in chapter 7 has indicated that even a single distance measurement affected by UDP can cause substantial degradation in performance. Therefore, it is absolutely critical that any indoor geolocation algorithm incorporate the capability to identify the presence of UDP conditions in the measurements and either correct them or exclude them from the location estimation process. Correction of distance measurements affected by UDP conditions prior to use is an interesting area of study and could vastly improve the performance of existing as well as new algorithms; some research on this initiative has been reported [Ven04]. It would be worthwhile to apply such concepts to realistic indoor channel models. An investigation of the existing algorithms as well as CN-TOAG with UDP identification capability is needed.

Bibliography

- [Ala03] B. Alavi, K. Pahlavan, “Bandwidth Effect on Distance Error Modeling for Indoor Geolocation”, *Proceedings of IEEE Personal Indoor Mobile Radio Communications Conference (PIMRC)*, 2003.
- [Ala05] B. Alavi, K. Pahlavan, “Indoor geolocation distance error modeling with UWB channel measurements”, *Proceedings of the IEEE Personal Indoor Mobile Radio Communications Conference (PIMRC)*, 2005.
- [Ala06a] B. Alavi, “Distance Measurement Error Modeling for Time-of-Arrival Based Indoor Geolocation”, *PhD Dissertation, Worcester Polytechnic Institute*, 2006.
- [Ala06b] B. Alavi, K. Pahlavan, “Studying the Effect of Bandwidth on Performance of UWB Positioning Systems”, *Proceedings of the IEEE Wireless Communications and Networking Conference, 2006 (WCNC-2006)*.
- [Aky02] I. F. Akyildiz, W. Su, Y. Sankarasubramaniam, E. Cayirci, “A Survey on Sensor Networks”, *IEEE Communications Magazine*, August 2002.
- [Als06a] N. Alsindi et al., “A Novel Cooperative Localization Algorithm for Indoor Sensor Networks”, *Proceedings of the IEEE Personal Indoor Mobile Communications Conference, 2006 (PIMRC-2006)*.
- [Als06b] N. Alsindi, K. Pahlavan, B. Alavi, “An Error Propagation Aware Algorithm for Precise Cooperative Indoor Localization”, *Proceedings of the IEEE Military Communications Conference, 2006 (MILCOM-2006)*.
- [Als08] N. Alsindi, K. Pahlavan, “Cooperative Localization Bounds for Indoor Ultra Wideband Wireless Sensor Networks” to appear in *EURASIP ASP special issue on Cooperative Localization in Wireless Ad Hoc and Sensor Networks*, 2008.
- [Aso01] M. Aso, M. Kawabata, T. Hattori, “A New Location Estimation Method Based on Maximum Likelihood Function in Cellular Systems”, *Proceedings of IEEE Vehicular Technology Conference fall (VTC2001-fall)*, 2001.

- [Bah00] P. Bahl, V. Padmanabhan, "RADAR: An in-building RF-based user location and tracking system", *Proceedings of IEEE INFOCOM: The Conference in Computer Communications, 2000 (INFOCOM-2000)*.
- [Bat02] R. Battiti, M. Brunato, and A. Villani, "Statistical learning theory for location fingerprinting in wireless LANs," Tech. Rep. DIT-02-0086, Dept. Inform. Telecomun., Universita di Trento, 2002.
- [Bot04a] C. Botteron, Anders Høst-Madsen, Michel Fattouche, "Effects of System and Environment Parameters on the Performance of Network-Based Mobile Station Position Estimators", *IEEE Transactions on Vehicular Technology, Vol. 53, No. 1, January 2004*.
- [Bot04b] C. Botteron, Anders Høst-Madsen, Michel Fattouche, "Cramer-Rao Bounds for the Estimation of Multipath Parameters and Mobiles' Positions in Asynchronous DS-CDMA Systems", *IEEE Transactions on Signal Processing, Vol. 52, No. 4, April 2004*.
- [Bro98] E. Brookner, *Tracking and Kalman Filtering Made Easy*, Wiley, New York, 1998.
- [Caf98] J. Caffery and G. L. Stuber, "Subscriber location in CDMA cellular networks," *IEEE Trans. Vehicular Technology, vol. 47, no. 2, May 1998*.
- [Caf99] J. Caffery, "Wireless Location in CDMA Cellular Radio Systems", *Kluwer International Series in Engineering and Computer Science, 1999*.
- [Cas06] R. Casas et al., "Robust Estimator for Non-Line-of-Sight Error Mitigation in Indoor Localization", *EURASIP Journal on Applied Signal Processing, Volume 2006, Article ID 43429*.
- [Cat04] A. Catovic, Z. Sahinoglu, "The Cramer-Rao Bounds of Hybrid TOA/RSS and TDOA/RSS Location Estimation Schemes", *IEEE Communications Letters, Vol. 8, No. 10, October 2004*.
- [Cha94] Y. T. Chan, K. C. Ho, "A Simple and Efficient Estimator for Hyperbolic Location", *IEEE Transactions on Signal Processing, Vol. 42, No. 8, August 1994*.
- [Che99] P-C. Chen, "Mobile position location estimation in cellular systems", PhD Thesis, WINLAB, Electrical and Computer Engineering Dept., Rutgers University, 1999.

- [Che02] Y. Chen, H. Kobayashi, "Signal Strength Based Indoor Geolocation", *Proceedings of the IEEE International Conference on Communications, 2002 (ICC-2002)*.
- [Chi04] K. Chintalapudi et al., "Ad-hoc localization using ranging and sectoring," *Proceedings of IEEE INFOCOM, 2004*.
- [Con02] L. Cong, W. Zhuang, "Hybrid TDOA/AOA Mobile User Location for Wideband CDMA Cellular Systems", *IEEE Transactions on Wireless Communications, Vol. 1, No. 3, July 2002*.
- [Dar99] D. Dardari, V. Tralli, "High-Speed Indoor Wireless Communications at 60 GHz with Coded OFDM", *IEEE Transactions on Communications, Vol. 47, No. 11, November 1999*.
- [Dav68] W. C. Davidon, "Variance algorithm for minimization," *Computer Journal, vol. 10, 1968*.
- [Den04] B. Denis, N. Daniele, "NLOS Ranging Error Mitigation in a Distributed Positioning Algorithm for Indoor UWB Ad-Hoc Networks", *International Workshop on Wireless Ad-Hoc Networks, 2004 (IWWAN-2004)*.
- [Est02] D. Estrin, D. Culler, K. Pister, G. Sukhatme, "Connecting the Physical World with Pervasive Networks", *IEEE Pervasive Computing, Vol. 1, No. 1, January-March 2002*.
- [FCC96] US FCC Docket No. 94-102. "Revision of the commissions rules to insure compatibility with enhanced 911 emergency calling systems", *Federal Communications Commission Tech. Rep. RM-8143, July 1996*.
- [FCC02] US Federal Communications Commission, "Revision of Part 15 of the Commission's Rules Regarding Ultra-Wideband Transmission Systems," FCC 02-48, First Report & Order, April 2002.
- [Fis99] S. C. Fisher, K. Ghassemi, "GPS IIF – The Next Generation", *Proceedings of the IEEE, Vol. 87, No. 1, January, 1999*.
- [Fle87] R. Fletcher, Practical Methods of Optimization, *John Wiley & Sons, 1987*.
- [Gez05] S. Gezici et al., "Localization via Ultra-Wideband Radios", *IEEE Signal Processing Magazine, Vol. 22, No. 4, pp. 70-84, July 2005*.

- [Gio95] A. Giordano, M. Chan, H. Habal, "A Novel Location-Based Service and Architecture", *Proceedings of the IEEE Personal Indoor Mobile Communications Conference, 1995 (PIMRC-95)*.
- [Gou91] P. Goud, A. Sesay, M. Fattouche, "A Spread Spectrum Radiolocation Technique and Its Application to Cellular Radio", *Proceedings of the IEEE Pacific Rim Conference on Communications, Computers and Signal Processing, 1991*.
- [Gus05] F. Gustafsson, F. Gunnarsson, "Mobile Positioning Using Wireless Networks", *IEEE Signal Processing Magazine, July 2005*.
- [Har04] I. Haratcherev et al., "Hybrid Rate Control for IEEE 802.11", *Proceedings of the ACM International Workshop on Mobility Management and Wireless Access, 2004 (MobiWac'04)*.
- [Hat06] A. Hatami, "Application of Channel Modeling for Indoor Localization Using TOA and RSS", *PhD Dissertation, Worcester Polytechnic Institute, 2006*.
- [Hil01] Alex Hills, "Large Scale Wireless LAN Design", *IEEE Communications Magazine, Nov. 2001*.
- [Hel99] M. Hellebrandt, R. Mathar, "Location Tracking of Mobiles in Cellular Radio Networks", *IEEE Transactions in Vehicular Technology, Vol. 48, No. 5, September 1999*.
- [How90] S. J. Howard, K. Pahlavan, "Measurement and Analysis of the Indoor Radio Channel in the Frequency Domain", *IEEE Transactions on Instrumentation and Measurement, Vol. 39, No. 5, October 1990*.
- [How92] S. J. Howard, K. Pahlavan, "Autoregressive Modeling of the Wideband Indoor Radio Propagation", *IEEE Transactions on Communications, Vol. 40, No. 9, October 1992*.
- [Jan03] R-H. Jan, Y. R. Lee, "An Indoor Geolocation System for Wireless LANs", *Proceedings of the IEEE 2003 International Conference on Parallel Processing Workshops (ICPPW'03)*.
- [Jeo00] Y. Jeong et al., "A Wireless Position Location System Using Forward Pilot Signal", *Proceedings of IEEE Vehicular Technology Conference Spring (VTC2000-spring), 2000*.

- [Jen01] P. Jensfelt, "Approaches to mobile robot localization in indoor environments", *PhD Dissertation, Royal Institute of Technology, Stockholm, Sweden, 2001*.
- [Kan04a] M. Kanaan, K. Pahlavan, "A Comparison of Wireless Geolocation Algorithms in the Indoor Environment", *Proceedings of IEEE Wireless Communications and Networking Conference, 2004 (WCNC-2004)*.
- [Kan04b] M. Kanaan, K. Pahlavan, "CN-TOAG: A New Algorithm for Indoor Geolocation", *Proceedings of IEEE Personal Indoor Mobile Radio Conference, 2004 (PIMRC-2004)*.
- [Kan04c] M. Kanaan, K. Pahlavan, "Algorithm for TOA-based Indoor Geolocation", *IEE Electronics Letters, Vol. 40, No. 22, October 2004*.
- [Kan06a] M. Kanaan, F. O. Akgül, B. Alavi, K. Pahlavan, "A Study of the Effects of Reference Point Density on TOA-based UWB Indoor Positioning Systems", *Proceedings of IEEE Personal Indoor Mobile Radio Communications Conference, 2006 (PIMRC-2006)*.
- [Kan06b] M. Kanaan, F.O. Akgül, B. Alavi, K. Pahlavan, "Performance Benchmarking of TOA-based UWB Indoor Geolocation Systems Using MSE Profiling", *Proceedings of the IEEE Vehicular Technology Conference, fall 2006 (VTC2006-fall)*.
- [Kan07] M. Kanaan, M. Heidari, F. O. Akgül, K. Pahlavan, "Technical Aspects of Localization in Indoor Wireless Networks", *Bechtel Telecommunications Technical Journal, Vol. 5, No.1, January 2007*.
- [Kan08a] M. Kanaan, B. Alavi, A. Hatami, K. Pahlavan, "Channel Modeling and Algorithms for Indoor Positioning", *Springer Encyclopedia of GIS, January 2008*.
- [Kan08b] M. Kanaan, K. Pahlavan, F.O. Akgül, "Analysis of the Effects of Node Density and Bipolar Channel Behavior on Infrastructure-based UWB Indoor Geolocation Using Time of Arrival", *Submitted to IEEE Transactions on Wireless Communications*.
- [Kap96] E. D. Kaplan, *Understanding GPS*, Artech House, Boston, 1996.
- [Lie98] K. Lieska, E. Laitinen, J. Lähteenmäki, "Radio Coverage Optimization with Genetic Algorithms", *Proceedings of the IEEE Personal Indoor Radio Communications Conference, 1998*.

- [Mai07] L. Mailaender, "Comparing Geolocation Bounds for TOA, TDOA and Round-Trip TOA", *Proceedings of IEEE Personal Indoor Mobile Radio Conference, 2007 (PIMRC-2007)*.
- [Mat98] D. M. Matic, H. Harada, R. Prasad, "Indoor and Outdoor Frequency Measurements for MM-Waves in the Range of 60 GHz", *Proceedings of the IEEE Vehicular Technology Conference, 1998*.
- [McG03] M. McGuire, K.N. Plataniotis, and A.N. Venetsanopoulos, "Location of mobile terminals using time measurements and survey points," *IEEE Trans. Veh. Technol.*, vol. 52, no. 4, July 2003.
- [McK05] M.L. McKelvin, M.L. Williams, N. M. Berry, "Integrated Radio Frequency Identification and Wireless Sensor Network Architecture for Automated Inventory Management and Tracking Applications", *2005 Richard Tapia Celebration of Diversity in Computing Conference (TAPIA'05)*.
- [Mis01] P. Misra, P. Enge, *Global Positioning System: Signals, Measurements, and Performance*, Ganga-Jamuna Press, 2001.
- [Mol03] A. F. Molisch, J. R. Foerster, M. Pendergrass, "Channel Models for Ultrawideband Personal Area Networks", *IEEE Wireless Communications*, December 2003.
- [Mol06] A. F. Molisch et al., "A Comprehensive Standardized Model for Ultrawideband Propagation Channels", *IEEE Transactions on Antennas and Propagation*, Vol. 54, No. 11, November 2006.
- [Mos03] R. Moses, D. Krishnamurthy, and R. Patterson, "A Self-Localization Method for Wireless Sensor Networks", *Eurasip Journal on Applied Signal Processing, Special Issue on Sensor Networks*, Vol. 2003, No. 4, March 2003.
- [Ner04] C. Nerguizian, C. Despins, S. Affés, "Indoor Geolocation with Received Signal Strength Fingerprinting and Neural Networks", *Proceedings of the IEEE 11th International Conference on Telecommunications (ICT2004), August 2004, Fortaleza, Brazil*.
- [Ner06] C. Nerguizian, C. Despins, S. Affés, "Geolocation in Mines with an Impulse Response Fingerprinting Technique and Neural Networks", *IEEE Transactions on Wireless Communications*. Vol. 5, no. 3, March 2006.

- [Opp04] I. Oppermann, M. Hämäläinen, J. Iinatti (Eds.), “UWB Theory and Applications”, *Wiley*, 2004.
- [Ott77] G. D. Ott, “Vehicle location in cellular mobile radio system,” *IEEE Transactions on Vehicular Technology*, vol. VT-26, February 1977.
- [Pah98] K. Pahlavan, P. Krishnamurthy, J. Beneat, “Wideband Radio Propagation Modeling for Indoor Geolocation Applications”, *IEEE Communications Magazine*, Vol. 36, Issue 4, April 1998.
- [Pah00] K. Pahlavan et al., “An Overview of Wireless Indoor Geolocation Techniques and Systems”, *Proceedings of the Mobile Wireless Communications and Networks Conference, 2000 (MWCN-2000)*.
- [Pah02] K. Pahlavan, X. Li, J. Makela, “Indoor Geolocation Science and Technology”, *IEEE Communications Magazine*, February, 2002.
- [Pah05] K. Pahlavan, A. Levesque, *Wireless Information Networks*, 2nd edition, Wiley, 2005.
- [Pan96] M. A. Panjwani, A. L. Abbott, T. S. Rappaport, “Interactive Computation of Coverage Regions for Wireless Communications in Multifloored Indoor Environments”, *IEEE Journal on Selected Areas in Communications*, Vol. 14, No. 3, April 1996.
- [Pat03] N. Patwari et al., “Relative Location Estimation in Wireless Sensor Networks”, *IEEE Transactions on Signal Processing*, Vol. 51, No. 8, August 2003.
- [Pat05] N. Patwari et al., “Locating the Nodes: Cooperative Localization in Wireless Sensor Networks”, *IEEE Signal Processing Magazine*, July 2005.
- [Pro03] I. F. Proгри, “Analysis of Indoor Geolocation Systems”, *Ph.D. Dissertation, Worcester Polytechnic Institute, 2003*.
- [Qi03] Y. Qi, “Wireless Geolocation in a Non-Line-of-Sight Environment”, PhD Dissertation, Princeton University, 2003.
- [Qi05] Y. Qi et al., “On Geolocation in Ill-Conditioned BS-MS Layouts”, *Proceedings of the IEEE International Conference on Acoustics Speech and Signal Processing, 2005 (ICASSP-2005)*.

- [Qi06] Y. Qi, H. Kobayashi, H. Suda, "Analysis of Wireless Geolocation in a Non-Line-of-Sight Environment", *IEEE Transactions on Wireless Communications*, Vol. 5, No. 3, March 2006.
- [Rao03] B. Rao, L. Minakakis, "Evolution of Mobile Location-based Services", *Communications of the ACM*, Vol. 46, No. 12, December 2003.
- [Roo02] Teemu Roos, Petri Myllymäki, Henry Tirri, "A Statistical Modeling Approach to Location Estimation", *IEEE Transactions on Mobile Computing*, Vol. 1, No. 1, January-March 2002.
- [Sal87] A. Saleh, R. Valenzuela, "A Statistical Model for Indoor Multipath Propagation", *IEEE Journal on Selected Areas in Communications*, Vol. SAC-5, No. 2, February 1987.
- [Sav01] C. Savarese, J. Rabaey, and J. Beutel, "Locating in distributed adhoc wireless sensor networks," *Proceedings of IEEE International Conference on Acoustics Sensors and Signal Processing (ICASSP)*, 2001.
- [Sav05] A. Savvides et al., "An Analysis of Error Inducing Parameters in Multihop Sensor Node Localization", *IEEE Transactions in Mobile Computing*, Vol. 4, No. 6, November/December 2005.
- [Say05] A. H. Sayed, A. Tarighat, and N. Khajehnouri, "Network-Based Wireless Location", *IEEE Signal Processing Magazine*, July 2005.
- [Sei92] S. Y. Seidel, T. S. Rappaport, "914 MHz Path Loss Prediction Models for Indoor Wireless Communications in Multifloored Buildings", *IEEE Transactions on Antennas and Propagation*, Vol. 40, No. 2, February, 1992.
- [Sha99] M. Shaw, P. Levin, J. Martel, "The DoD: Stewards of a Global Information Resource, the Navstar Global Positioning System", *Proceedings of the IEEE*, Vol. 87, No. 1, January, 1999.
- [She96] H. D. Sherali, C. M. Pendyala, T. S. Rappaport, "Optimal Location of Transmitters fro Micro-Cellular Radio Communication System Design", *IEEE Journal on Selected Areas in Communications*, Vol. 14, No. 4, May 1996.

- [Shi05] Q. Shi et al., "Performance Analysis of Relative Location Estimation for Multihop Wireless Sensor Networks", *IEEE Journal on Selected Areas in Communications*, Vol. 23, No. 4, April 2005.
- [Sil96] M. I. Silventoinen, T. Rantalainen, "Mobile station emergency locating in GSM", *Proceedings of the IEEE International Conference on Personal Wireless Communications, 1996 (ICPWC-96)*.
- [Sno03] D. Snoonian, "Smart Buildings", *IEEE Spectrum*, August, 2003.
- [Spe00] Q. H. Spencer, B. D. Jeffs, M. A. Jensen, A. L. Swindlehurst, "Modeling the Statistical Time and Angle of Arrival Characteristics of an Indoor Multipath Channel", *IEEE Journal on Selected Areas in Communications*, Vol. 18, No. 3, March 2000.
- [Spi01] M. A. Spirito, "On the Accuracy of Cellular Mobile Station Location Estimation", *IEEE Transactions on Vehicular Technology*, Vol. 50, No. 1, May 2001.
- [Str88] G. Strang, *Linear Algebra and Its Applications*, Third Edition, Saunders College Publishing, 1988.
- [Tho01] N.J. Thomas, D. G. M. Cruickshank, D.I. Laurenson, "Performance of a TDOA-AOA Hybrid Mobile Location System", *Proceedings of the IEEE 2nd International Conference on 3G Mobile Communications and Technologies*, March, 2001.
- [Tor84] D. Torrieri, "Statistical theory of passive location systems", *IEEE Trans. Aerospace and Elect. Sys.*, vol. AES-20, March 1984.
- [Unb02] M. Unbehaun, "On the Deployment of Unlicensed Wireless Infrastructure", Doctoral Dissertation, Royal Institute of Technology, Department of Signals, Sensors and Systems, Stockholm, Sweden, 2002.
- [Unb03] M. Unbehaun, M. Kamenetsky, "On the Deployment of Picocellular Wireless Infrastructure", *IEEE Wireless Communications*, December 2003.
- [Urr06] A. Urruela, J. Sala, J. Riba, "Average Performance Analysis of Circular and Hyperbolic Geolocation", *IEEE Transactions on Vehicular Technology*, Vol. 55, No. 1, January 2006.
- [Van68] H. L. Van Trees, *Detection, Estimation and Modulation Theory*, Part I, John Wiley & Sons, Inc. 1968.

- [Ven04] S. Venkatraman, J. Caffery, H-R. You, "A Novel ToA Location Algorithm Using LoS Range Estimation for NLoS Environments", *IEEE Transactions on Vehicular Technology*, Vol. 53, No. 5, September 2004.
- [Vil99] E. Villier, L. Lopes, B. Ludden, "Performance of a Handset-Assisted Positioning Method for GSM", *Proceedings of IEEE Vehicular Technology Conference (VTC99)*, 1999.
- [Wal02] M. Wallbaum, "WhereMOPS: An Indoor Geolocation System", *Proceedings of the IEEE Personal Indoor Mobile Radio Communications Conference, 2002 (PIMRC-2002)*.
- [Wan92] R. Want, A. Hopper, V. Falcão, J. Gibbons, "The Active Badge Location System", *ACM Transactions on Information Systems*, Vol. 10, Issue 1, January 1992.
- [Wan03] X. Wang, Z. Wang, B. O'Dea, "A TOA-based Location Algorithm Reducing the Errors Due to Non-Line-of-Sight (NLOS) Propagation", *IEEE Transactions on Vehicular Technology*, Vol. 52, No. 1, January 2003.
- [War97] A. Ward, A. Jones, A. Hopper, "A New Location Technique for the Active Office", *IEEE Personal Communications*, Vol. 4, Issue 5, October 1997.
- [Wei03] A. J. Weiss, "On the Accuracy of a Cellular Location System Based on RSS Measurements", *IEEE Transactions on Vehicular Technology*, Vol. 52, No. 6, November 2003.
- [Wer98] J. Werb and C. Lanzl. "Designing a positioning system for finding things and people indoors" *IEEE Spectrum*, September 1998.
- [Wil05] J. Wilden, J. Agniel, R. Moses, "Geolocation of Wireless Sensors with Nonuniform GPS Availability", *Unattended Ground Sensor Technologies and Applications VII (Proc. SPIE 5796)*, SPIE Defense and Security Symposium, 2005.